

Numerical Investigation of Thermal-driven Thin Film Instabilities

by

Ali Mohammadtabar

A thesis submitted in partial fulfillment of the requirements for the degree of

Doctor of Philosophy

Department of Mechanical Engineering

University of Alberta

© Ali Mohammadtabar, 2021

Abstract

Instability, morphology, and dewetting of thin films have been the subject of intensive research due to their important industrial and technological applications, including decorative or protective coatings, an intervening media in liquid-liquid emulsions, and polymer films in soft lithography. Thin-film instability can be triggered either naturally through intermolecular forces or with external forces such as mechanical, thermal, and electric forces. Thermal-induced patterning of ultra-thin liquid films subjected to temperature gradient is investigated by characterizing the dynamics, instability, and pattern formation process. The majority of existing studies in the literature are restricted to lubrication approximation, which is only valid for the cases that the initial film thickness is smaller than the characteristic wavelength of induced instabilities. The long-wave approximation is not valid in the later stages of pattern evolution. Hence, in this thesis, the full governing equations of fluid flow and the thermally induced Marangoni effect are employed to track the polymer film's interface and the air bounding layer. First, a phase-field numerical model is developed to simulate the dynamic process of thermal-induced patterning. A systematic study on the impact of influential parameters has revealed an increase in the temperature gradient, thermal conductivity ratio, and initial thickness of the thin-film resulted in a shorter processing time and faster pattern formation. The newly developed numerical model more accurately predicts the characteristic wavelength than the linearized model. In the second part, the volume of fluid (VOF) and thin film (TF) methods are used to solve the governing equations. The results obtained from VOF are compared with the TF model in many cases to find the best model for predicting the characteristic wavelength for the growth of thermal-induced instabilities. This is followed by examining the effect of the protrusion width and the distance between the protrusions on the structures' final shape and interface evolution time in both VOF and TF models. Then, the linear

theoretical relations for forming secondary pillars are presented based on the width of protrusions, their separation distance, and the inverse filling ratio. The number of pillars is found to increase with the protrusions' width and distance between protrusions. In the last part, a mathematical model is developed to characterize the thermocapillary destabilization of the air–polymer interface for non-Newtonian polymer films. A power-law model is adopted to model shear-thickening/thinning fluids and overcome the assumption limitations, such as the independence of viscosity from the shear rate. The presented analyses in this Ph.D. thesis will advance existing knowledge in the thermal-induced patterning mechanism, providing practical implications for lowering the cost and time requirements in designing related experiments.

Preface

Journal Papers from Ph.D. thesis:

- **Ali Mohammadtabar**, Hadi nazaripoor, Adham Riad, Arman Hemmati, Mohtada Sadrzadeh, A numerical study for thermocapillary induced patterning of thin liquid films, *Physics of Fluids* 32 (2), 024106 (2020).
- **Ali Mohammadtabar**, Hadi Nazaripoor, Adham Riad, Arman Hemmati, Mohtada Sadrzadeh, Two-layer modeling of thermally induced Bénard convection in thin liquid nanofilms: Volume of Fluid approach vs. Thin-Film model, *AIP Advances* 11 (4), 045317 (2021).
- **Ali Mohammadtabar**, Hadi Nazaripoor, Adham Riad, Arman Hemmati, Mohtada Sadrzadeh, “Thermocapillary patterning formation of the power-law fluids, Ready for Submission to *Physics of Fluids*.

Conference Presentations:

- Adham Riad, Hadi Nazaripoor, **Ali Mohammadtabar**, Mohtada Sadrzadeh, Electrohydrodynamic patterning of non-newtonian thin films, American Physical Society, APS Division of Fluid Dynamics (Fall) 2019, abstract id.Q34.004 , November 2019.
- **Ali Mohammadtabar**, Hadi Nazaripoor, Behnam Khorshidi, Mohtada Sadrzadeh, Numerical modeling of transport phenomena in patterned nanofiltration membranes, 3rd International Conference on Desalination using Membrane Technology, May 2017.

This thesis is dedicated to my late mother.

For her endless love, support, and encouragement

Acknowledgment

I would like to express my sincere thankfulness to my late mother, who was among us when I started the program and was waiting for my Ph.D. graduation. My deepest regret is that I couldn't make it when you were among us. Thanks for all your motherly care.

It has been a great experience, and I would like to thank all the people who contributed in some way to the work presented in this thesis. First, I would like to express my sincere gratitude to my supervisors Dr. Mohtada Sadrzadeh and Dr. Arman Hemmati, for their continuous support, guidance, and advice. I would also like to thank my committee member, Dr. Morris R. Flynn, for his valuable comments and suggestions.

This work wouldn't be complete without financial support from the Natural Sciences and Engineering Research Council of Canada (NSERC), Canada's Oil Sands Innovation Alliance (COSIA), and Natural Resources Canada (NRC).

Thanks to my friends and lab mates for their support, friendship and help. I thank Dr. Behnam Khorshidi, my office mate, for providing me valuable information. I also thank Dr. Hadi Nazari-poor for all his helpful comments and brainstorming discussions on different aspects of my research.

I would like to sincerely thank my beloved wife, Simin, for her love, understanding, and constant support. Thank you for always being there for me through the ups and downs of my life. But most of all, thank you for being my best friend. I feel lucky to have such a lovely companion to spend the rest of my life with.

Contents

Chapter 1 - Introduction

1.1. Thin liquid film dynamics.....	1
1.2. Technological applications	1
1.2.1. Coatings	1
1.2.2. Emulsion and foams.....	3
1.2.3. Lithography (micron- and nano-patterning).....	5
1.3. Scope and objectives.....	7
1.4. Thesis organization	7
1.5. Thesis contribution.....	8

Chapter 2 - Literature review

2.1. Previous instability studies: Surface Charge (SC) and Acoustic Phonon (AP) model	10
2.2. Previous instability studies: Thermocapillary (TC) model	11
2.2.1. History.....	11
2.2.2. TC model for instability.....	12
2.2.3. Pattern replication through localized film deformation	13
2.2.4. Nonlinear analysis in thermal induced patterning.....	13
2.3. Summary	14

Chapter 3 - A numerical study for thermocapillary induced patterning of thin liquid films

3.1. Introduction.....	16
3.2. Mathematical Model.....	20
3.2.1. Governing Equations and Boundary Conditions.....	21
3.2.1.1. Fluid flow and heat transfer	21
3.2.1.2. Phase field equations.....	21
3.2.1.3. Boundary conditions	22
3.2.2. Validation and Verification.....	25
3.3. Result and Discussion	27
3.3.1. Pattern Formation and Temperature Gradient.....	28
3.3.2. Influence of polymer thickness, driving force, and thermal conductivity.....	31
3.3.2.1. Effect of initial polymer thickness	31

3.3.2.2. Effect of The Driving Force.....	31
3.3.2.3. Effect of Thermal Conductivity	33
3.3.3. Impact of Geometry on the Pattern Formation	34
3.3.3.1. Effect of protrusions width	34
3.3.3.2. Effect of the distance between protrusions	35
3.3.3.3. Effect of protrusions height.....	37
3.3.4. Effect of Wettability of Protrusions	38
3.4. Conclusion	40

Chapter 4 - Two-layer modeling of thermally induced Bénard convection in thin liquid films: Volume of fluid approach vs. thin-film model

4.1. Introduction.....	41
4.2. Mathematical Model	44
4.2.1. Governing Equations and Boundary Conditions (VOF model).....	45
4.2.1.1. VOF model and computational procedure	45
4.2.2. Scaling parameters and thin-film evolution	50
4.2.2.1. Linear stability analysis	51
4.3. VOF Verification	52
4.4. Results and Discussion	53
4.4.1. Non-uniform Temperature Gradient and Morphological Evolutions	53
4.4.2. Characteristic wavelength Predictions: VOF vs. LS analysis	56
4.4.2.1. Validation.....	57
4.4.2.2. Developing VOF model for thermocapillary thin-film flow.....	57
4.4.2.3. The effect of Marangoni and Capillary inverse numbers on the VOF-TC model	59
4.4.3. Effect of Mask Geometry on the Pattern Formation.....	62
4.4.3.1. The effect of protrusions width	62
4.4.3.2. The effect of the distance between protrusions.....	66
4.5. Conclusions.....	71

Chapter 5 - Thermocapillary patterning of non-Newtonian thin films

5.1. Introduction.....	72
5.2. Mathematical Model	74
5.2.1. Problem statement.....	74
5.2.2. Power-law for modeling non-Newtonian fluids.....	75

5.2.3. Thin-film evolution equation	76
5.2.4. Linear stability analysis	80
5.2.5. Numerical modeling.....	81
5.3. Results and Discussion	83
5.3.1. Newtonian Fluid.....	83
5.3.2. Time scale and spatiotemporal evolution in non-Newtonian TC patterning.....	84
5.3.3. Local effective viscosity distribution and its effect on pattern morphology	86
5.3.4. Rheological effects on pillar density and the characteristic wavelength.....	88
5.4. Conclusions.....	92
Chapter 6 - Conclusion and future work	
6.1. Conclusion	94
6.2. Future work.....	97
References	99
Appendix A – Vertical distance and wettability in phase field approach	116
Appendix B – Thin film equation derivation	118

List of Tables

Table 3.1. List of boundary conditions considered in the simulations.....	23
Table 3.2. Parameters and constants used in TC simulation.....	24
Table 3.3. The order of magnitude estimates for characteristic numbers.	25
Table 4.1. List of boundary conditions considered in the simulations.....	49
Table 4.2. Parameters and constants used in the TC simulation.....	50
Table 4.3. The effect of grid size on transient growth of interface height.....	53
Table 4.4. The characteristic wavelength in the different approaches.....	57
Table 4.5. The different parameters used for finding a relation between the VOF and the LS analysis ($w = 6 \mu m$ and $lp = 7 \mu m$).....	58
Table 5.2. List of dimensionless parameters and their values.....	80
Table 5.3. Constants and parameters used in simulations.....	81

List of Figures

Figure 1.1. Schematic of a dewetting process, a liquid film dewets into one drop. In the Young’s equation, θ is an equilibrium contact angle, σ_{sv} , σ_{sl} and σ_{lv} are solid/vapor, solid/liquid and liquid/vapor interfacial tensions. $\theta = 0$ in initial wetting, $0 < \theta < \pi$ in partial wetting, and $\theta = \pi$ in nonwetting. 2

Figure 1.2. Schematic view of thin film confined between two substrates. h_0 is the film thickness. 6

Figure 2.1. Basic nanofilm instability geometry [64] 9

Figure 2.2. Basic nanofilm deformation geometry with a patterned top plate [64] **Error! Bookmark not defined.**

Figure 3.1. 2D schematic of the ultrathin liquid film placed between the top (cold) and bottom (hot) substrates, where $T_H > T_C > T_g$. Here, T_g is the glass transition temperature of the polymer film..... 20

Figure 3.2. Schematic diagram introducing the boundary condition and mesh of the 2D model (not to scale)..... 23

Figure 3.3. The Effect of grid size on transient growth of interface height, $h_0 = 100$ nm, $d = 300$ nm, $W_1 = 800$ nm, $W_2 = 200$ nm, $H = 100$ nm and $\Delta T = 50$ °C..... 26

Figure 3.4. Temporal evolution predictions of air–polymer free surface under $h_0 = 100$ nm, $d = 300$ nm, $W_2 = 5000$ nm, $H = 100$ nm and $\Delta T = 46$ °C..... 27

Figure 3.5. Unsteady contour of temperature at a(i) initial stage, a(ii) 40 ns, a(iii) 70 ns and a(iv) 100 ns. (b) The temperature gradient profile along the interface and the line near the protrusions at steady state condition. The protrusion width of 0.2 μ m and the height of 0.1 μ m. 29

Figure 3.6. Thermally induced hierarchical structures for a patterned template. 2D snapshots of the film interface, $h_0 = 100$ nm, $D = 300$ nm, $W_1 = 800$ nm, $W_2 = 200$ nm and $\Delta T = 50$, at

different stages of the evolution process, a(i) initial, a(ii) 60 μs , a(iii) 141 μs , a(iv) 141 μs and a(v) 200 μs , (b) 2D snapshots of the pressure contour and velocity vector at different stages of the evolution process, (c) The tracking of the interface height of a pillar.	30
Figure 3.7. The changing trend of pattern formation induced by thermal gradient with the filling ratio factors of (a) 0.2, (b) 0.33, and (c) 0.5.....	32
Figure 3.8. The implications of varying temperature gradient on (a) the polymer-air interface, and (b) the transient behavior of the interface height.	32
Figure 3.9. The tracking of the interface height of a pillar at different ratios of thermal conductivity (Kr).....	33
Figure 3.10. (a) The changing trend of pattern formation induced by thermal gradient with the different protrusion width, a(i) 200 nm, a(ii) 400 nm and a(iii) 800 nm, (b) The temperature gradient profile for two cases, a(ii) and a(iii).	34
Figure 3.11. Thermally induced hierarchical structures for a patterned template. 2D snapshots of the film interface at different stages of the evolution process, a(i) initial, a(ii) 0.83 ms, a(iii) 5 ms, a(iv) 5.83 ms, a(v) 6.66 ms and a(vi) 8.75 ms. (b) The tracking of the interface height of both primary and secondary pillar.	36
Figure 3.12. Relationship between the processing time and the template structure	37
Figure 3.13. The structure of the pillars for a base-case at different contact angle (a) 30, (b) 60, (c) 90, (d) 120 and (e) 150.....	39
Figure 4.1. 3D schematic of the ultrathin liquid film placed between the top (cold) and bottom (hot) substrates, where $T_H > T_C > T_g$. Here, T_g is the glass transition temperature of the polymer film.....	45
Figure 4.2. Schematic diagram introducing the boundary condition and mesh of the 2D model (not to scale).	49
Figure 4.3. Thermally-induced hierarchical structures for a patterned template, $d_1 = 3$, $d_2 = 2$, $w = 0.2$, $lp = 0.26$, $T = 1$, and $\lambda LS = 3.06 \mu\text{m}$. (a) 2D snapshots of the film interface at different stages of the evolution process. (b) Snapshots of the temperature distribution through the	

channel. (c) The temperature at the interface over time. (d) The tracking of the interface height of a pillar. (e) The effect of different thermal conductivity over time conductivity. 55

Figure 4.4. 2D snapshots of the thin film interface, $d1 = 3, d2 = 2, w = 0.2, lp = 0.27, T = 1$, and $\lambda LS = 3.06 \mu m$ 56

Figure 4.5. Thermally-induced hierarchical structures for a patterned template. 2D snapshots of the film interface, $h0 = 100 \text{ nm}, d1 = 300 \text{ nm}, d2 = 200 \text{ nm}, w = 6 \mu m, lp = 500 \text{ nm}$ and $\Delta T = 100 \text{ K}$ at different stages of the evolution process, a(i) initial, a(ii) 63 ms, a(iii) 83 ms, a(iv) 119 ms, a(v)149 ms and a(vi) 220 ms..... 59

Figure 4.6. The relation for dominant instability wavelength, λc for both VOF simulation and LS analysis..... 60

Figure 4.7. Marangoni and Capillary inverse numbers, the characteristic wavelength from LS and VOF at different film thicknesses. 61

Figure 4 8. Capillary inverse, the characteristic wavelength from LS and VOF at different temperature gradients..... 62

Figure 4.9. (a) 2D snapshots of the interface deformation and (b) normalized temperature profile at the interface when multiple pillars form under the protrusion, $w = 0.52$ 63

Figure 4.10. 2D snapshots of the interface deformation predicted by the TF model at $w = 1.47$ 64

Figure 4.11. The different stages in the formation of the pillars by increasing the width of the protrusions where $d1 = 3, d2 = 2, lp = 0.26$ and $T = 1$ 65

Figure 4.12. The threshold value for the width of the protrusions at different polymer thicknesses where $lp = 0.26$ and $\Delta T = 1$, (a) VOF model (b) TF model. 66

Figure 4.13. 2D time snapshots of the film interface in the TC induced patterning process focus on the secondary pillar formation, $d1 = 2, d2 = 1.5, w = 0.31, (lp)VOF = 0.82, T = 1$, and $\lambda LS = 2.03 \mu m$ 67

Figure 4.14. 2D time snapshots of the film interface in the TC induced patterning process focus on the secondary pillar formation, $d1 = 2, d2 = 1.5, w = 0.31, (lp)VOF = 2.1, T = 1$, and $\lambda LS = 2.03 \mu m$ 69

Figure 4.15. The final stage of the pattern formation for the different range of stamp periodicity where $d_2 = 1.5$, $w = 0.31$ and $T = 1$ 69

Figure 4.16. The threshold value for the distance between the protrusions at different polymer thicknesses where $w = 0.31$ and $\Delta T = 1$, (a) VOF model (b) TF model..... 70

Figure 5.1. Schematic of the ultrathin liquid film placed between the top (cold) and bottom (hot) substrates, where $T_H > T_C > T_g$. Here, T_g is the glass transition temperature of the polymer film. 75

Figure 5.2. The effect of grid size on transient growth of interface height 82

Figure 5.3. (a) Nondimensional pillars' height over time for a Newtonian fluid ($n=1$), (b) Plot showing 3D pillar distribution for a Newtonian film with $h_0 = 25$ nm. 83

Figure 5.4. Interface height of the fastest growth pillar and 3D snapshots of the interface structure over time for a shear-thinning case ($n=0.75$), (a) Maximum and minimum interface height vs. time, (b(i-iii)) 3D and 2D snapshots of the interface at three different times; b(i) $t = 0.36$, b(ii) $t = 0.45$, b(iii) $t = 1.17$. The parameters in this study are $h_0 = 25$ nm, $d = 100$ nm, $\Delta T = 46$ °C, and $n = 0.75$. (c) Final shape and structure of the pillars from top view, (d) Nondimensional pillars' shear rate versus scaled time for a shear thinning case. 85

Figure 5.5. Interface height of the fastest growth pillar and 3D snapshots of the interface structure over time for a shear-thickening case ($n=1.2$), (a) Maximum and minimum interface height vs. time, (b(i-iii)) 3D and 2D snapshots of the interface at three different times; b(i) $t = 0.15$, b(ii) $t = 0.17$, b(iii) $t = 1.17$. The parameters in this study are $h_0 = 25$ nm, $d = 100$ nm, $\Delta T = 46$ °C, and $n = 1.2$, (c) Final shape and structure of the pillars from the top view, (d) Nondimensional pillars' shear rate versus scaled time for a shear thickening case. 86

Figure 5.6. (a) Tracking interface height over time for a shear-thinning fluid ($n=0.75$), (b) Nondimensional pillars' viscosity versus scaled time for a shear thinning film, (c(i-iii)) Spatiotemporal evolution of the interface at nondimensional times $t = 0.36$, $t = 0.49$ and $t = 1.17$, (d(i-iii)) Effective viscosity distribution at nondimensional times $t = 0.36$, $t = 0.49$ and $t = 1.17$ 87

Figure 5.7. (a) Tracking interface height over time for a shear-thickening fluid ($n=1.2$), (b) Nondimensional pillars' viscosity versus scaled time for a shear thickening film, (c(i-iii)) Spatiotemporal evolution of the interface at nondimensional times $t = 0.15$, $t = 0.17$ and $t = 1.17$, (d(i-iii)) Effective viscosity distribution at nondimensional times $t = 0.15$, $t = 0.17$ and $t = 1.17$ 89

Figure 5.8. (a) The characteristic wavelength obtained from linear stability (LS) analysis versus flow behavior index for different film thicknesses, (b) The characteristic wavelength at different film thicknesses for both shear thinning and shear thickening cases..... 90

Figure 5.9. Shear thinning case, (i-v) 3D snapshots of the interface profile. Initial film thickness, $h_0 =$ (i) 65 nm, (ii) 55 nm, (iii) 45 nm, (iv) 35 nm, (v) 25 nm. $Ma =$ (i) 1.54, (ii) 2.38, (iii) 3.65, (iv) 5.76, and (v) 9.69. Plates distance, $d=100$ nm, temperature difference, $\Delta T = 46$ °C. 91

Figure 5.10. Shear thickening case, (i-v) 3D snapshots of the interface profile. Initial film thickness, $h_0 =$ (i) 65 nm, (ii) 55 nm, (iii) 45 nm, (iv) 35 nm, (v) 25 nm. $Ma =$ (i) 1.54, (ii) 2.38, (iii) 3.65, (iv) 5.76, and (v) 9.69. Plates distance, $d=100$ nm, temperature difference, $\Delta T = 46$ °C. 92

Figure A1. The changing trend of pattern formation induced by thermal gradient with the different substrates distance, (a) 270 nm, (b) 300 nm and (c) 400 nm. 116

Figure A2. Surface tension balance based on Young's considerations. 117

Figure B1. Thermally-induced hierarchical structures for a patterned template. 2D result of nonlinear thin film, $h_0 = 100$ nm, $d_2 = 200$ nm, $w = 6$ μ m, $lp = 500$ nm and $\Delta T = 50$ K at different shorter substrates distance, (a) $d_1 = 220$ nm, (b) $d_1 = 250$ nm, and , (c) $d_1 = 300$ nm. (d) The tracking of the Interface height of pillar at different shorter substrates distance..... 118

Nomenclature

A	Effective Hamaker constant [J]
Bi	Biot number [-]
Bo	Bond number (Bo)
Ca^{-1}	Capillary inverse number, $(\frac{\sigma}{\mu u_c})$ [-]
d_1	the longest separation distances between plates [m]
\tilde{d}_1	dimensionless the longest separation distances between plates [m]
d_2	the smallest separation distances between plates [m]
\tilde{d}_2	dimensionless smallest separation distances between plates [m]
d_{ave}	average separation distances between plates, $\frac{(d_1+d_2)}{2}$ [m]
\tilde{d}_{ave}	inverse filling ratio, $(\frac{d_{ave}}{h_0})$ [-]
Δd	the protrusions height [-]
\mathbf{D}	deformation tensor
E	energy [J]
f_{free}	free energy [J]
F_v	volumetric force [J]
G	chemical potential [J]
h	interface height [m]
\tilde{h}	dimensionless interface height, [-]
h_0	initial interface height [m]
K	flow consistency index
k	thermal conductivity [W/mK]
k_r	relative thermal conductivity, $(\frac{k_p}{k_a})$ [-]
l_p	distance between two protrusions [m]
\tilde{l}_p	dimensionless between two protrusions [-]
l	domain length [m]
Ma	Marangoni number, $\frac{\sigma_T \Delta T}{\mu u_c}$ [-]
n	flow behavior index [-]

Pr	Prandtl number, $(\frac{c_p \mu}{k})$ [-]
p	pressure [pa]
Re	Reynolds number [-]
t	time [s]
\tilde{t}	dimensionless time [-]
T_H	hot temperature [k]
T_C	cold temperature [k]
T_g	polymer glass transition temperature [k]
T_0	reference temperature [k]
ΔT	temperature difference, $(T_H - T_C)$ [k]
w	the protrusion width [m]
\tilde{w}	dimensionless the protrusion width [-]
u_c	The characteristic velocity, $(\frac{\sigma_T k_r \tilde{d}_{ave} \Delta T}{\mu[(1-k_r)+k_r \tilde{d}_{ave}]^2})$ [m/s]
u_x, u_y, u_z	velocity components in x, y, z directions [m/s]
x, y, z	cartesian coordinates [m]

Greek symbols

α	volume fraction [-]
μ	dynamic viscosity [$kg\ m^{-1}s^{-1}$]
ν	kinematic viscosity [m^2s^{-1}]
ρ	Density [kg/m^3]
σ	surface tension [N/m]
σ_0	reference surface tension [N/m]
σ_T	temperature derivative of the surface tension [N/mK]
σ_{sv}	solid/vapor surface tension [N/m]
σ_{sl}	solid/liquid surface tension [N/m]
σ_{lv}	liquid/vapor surface tension [N/m]
κ	curvature [m^{-1}]
λ	the characteristic wavelength

ξ	Long-wavelength approximation factor [-]
θ	Equilibrium contact angle (radian)
$\dot{\gamma}$	shear rate [s^{-1}]

Subscripts

l	liquid phase
g	gas phase
a	air
p	polymer
VOF	volume of fluid
LS	linear stability analysis

Chapter 1 – Introduction ¹

1.1. Thin liquid film dynamics

Thin liquid films and surfaces have been widely used in our daily life. They are present as protective coatings to enhance the conduction or insulation of surfaces or decorative coatings to improve the product's beauty [1]. They are also needed in the intervening area in oil-water emulsions and employs as an eye lubricant [2]. Thin liquid films have been applied in a cooling method for the thermal management of semiconductors [3].

The stability of thin films plays a vital role in technological processes; therefore, there has been done numerous theoretical and experimental studies to investigate the influential parameters that lead to the film rupture [1,2,4–14]. Thin-film instabilities engendered either naturally (i.e., intermolecular forces) [4,15,16] or by external forces such as mechanical [17], thermal [18,19], and electric forces [20–23]. These perturbations result in various dynamics differing from stable films to ruptured films indicating dry holes. Such behavior is related to the intermolecular interactions that are usually not important in bulk fluid dynamics [10]. Thin films become unstable when the wavelength of fluctuations exceeds a critical value [9].

An ultra-thin film (the thickness of films is 100 nm or less) is either stable or unstable, which can be determined by the sign of the second derivative of interaction potential respecting film thickness [9]. Natural intermolecular interactions determine the initial state of a thin film (polar [4] and apolar [9,10,12] interactions) which depends on the properties of system materials [24].

1.2. Technological applications

1.2.1. Coatings

Different techniques have been applied to cover the substrate for decorating or protecting the surface. The most common ones are galvanizing, electrochemical coating, vapor deposition, conversion coatings, thermal spraying, and thin-film coating that are used in various industries, ranging from the printing and textile, pharmaceutical and chemical, automotive to food industries.

¹ Parts of this chapter is based on Mohammadtabar et al. Phys. Fluids. 32 (2020) 024106, Ref. [96]

Although each coating technique provides merits, some disadvantages are restricting their applications [26,27]. Homogenous, uniform thickness, and non-volatile liquid coated surface are of substantial technical importance in thin-film stability on the solid substrate and one of the most critical factors for adopting a coating method. The main concern causing unstable and heterogeneous thin film coating (As shown in Fig. 1.1.) is the disjoining of non-volatile liquid or dewetting [26,28–30]. Dewetting is a spontaneous phenomenon from the withdrawal of a liquid film from the substrate due to interaction and attractive interfacial and intermolecular energies. Dewetting can occur either by expanding the dry zone on the film surface and nucleation resulting in a metastable film or amplifying capillary waves, causing the formation of the unstable film [13,31,32]. The dewetting phenomenon happens in some sequence phases. The first phase involves the growth of perturbations and their amplification, followed by the film's rupture. Then, holes form and start expansion in their size, leading to a polygonal network of straight liquid string or rims. Finally, Rayleigh instability causes the decay and break up in strings resulting in the formation of droplets [33].

Surface chemistry, temperature gradient, initial film thickness, surface forces, and energy are key to defining the dewetting behavior [24,34,35]. Dewetting and instability in thin films (at nanometer thickness) takes place by spontaneous rupture of thin-film (a spinodal mechanism) due to long-range van der Waals forces [16,34]. On the other hand, homogenous and heterogeneous nucleation arise from thermal noise and surface heterogeneity, respectively are the source of the instability and dewetting in thicker films [34].

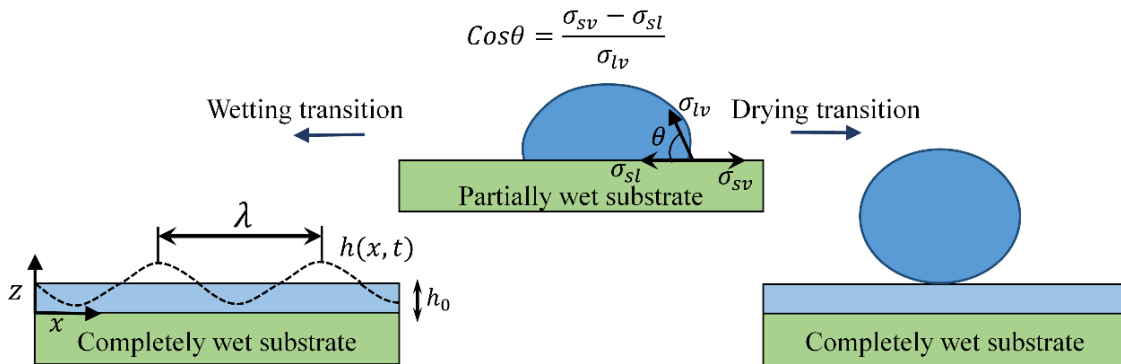


Figure 1.1. Schematic of a dewetting process, a liquid film dewets into one drop. In Young's equation, θ is an equilibrium contact angle, σ_{sv} , σ_{sl} and σ_{lv} are solid/vapor, solid/liquid and liquid/vapor interfacial tensions. $\theta = 0$ in initial wetting, $0 < \theta < \pi$ in partial wetting, and $\theta = \pi$ in nonwetting.

The Dewetting process is considered a dynamic process starting from a non-equilibrium condition: the flat film on the substrate and continuing to reach an equilibrium state where a droplet or a set of droplets emerges [29]. Considering a droplet at the solid surface, there are three distinct phases: liquid-gas, solid-liquid, and solid-gas. In equilibrium condition, a liquid drop on a homogenous surface forms a spherical cap with the contact angle of θ , tangent to the droplet at the three phase contact line. Young's equation defines the relation between the contact angle of θ and three-phase contact line [24,29,35]. However, the intermolecular interactions between liquid-vapor and solid-liquid interfaces are not considered in Young's definition. These interactions can be determined by van der Waals interactions consisting of Keeson, Debye, and London dispersion forces. The van der Waals interaction for a thin film layer on the solid substrate bonded with another layer is defined as $\Phi_{vdW} = A/6\pi h^3$ where A defines as the effective Hamaker constant depending on substrate material and fluid layers [24,25]. For example, the effective Hamaker constant for a three-layer system is defined as $A_{213} = (\sqrt{A_{33}} - \sqrt{A_{11}})(\sqrt{A_{22}} - \sqrt{A_{11}})$ where subscripts 1, 2, and 3 refer substrate, liquid film, and bounding fluid, respectively. Hamaker constant with a negative sign signifies the liquid film is stable and does not dewet the substrate[24,25].

1.2.2. Emulsion and foams

The thin film acts as an intervening media to separate the dispersed gas-liquid phase in food foam or liquid-liquid emulsion, either water-in-oil or oil-in-water [36]. The stability of foam and emulsion is a function of stability and structure of thin-film forming between bubbles, emulsion drops, or a bubble and oil drop, respectively. Coalescence is one of the most important mechanisms in controlling the stability of foam and emulsion.

The thin liquid film emerges from the local deformation of the collision of two droplets or bubbles. Then it starts draining in droplets/bubbles in the presence of a Laplace pressure until the film thickness reaches the critical value and ruptures. This phenomenon refers to the coalescence process. The coalescence process causes the foam or emulsion to become unstable, which is called demulsification. It worth noting that the average size of bubble or droplets depends on the instability level of foam and emulsion [37,38].

As noted above, dispersed colloid systems such as foam and emulsion have fundamental importance in various industries. Surfactants are implemented as emulsifiers to provide stability of emulsion or foam in the food and pharmaceutical industry. However, in the oil industry, various

demulsification techniques are applied to produce produced water, which plays a crucial role in crude oil extraction. These techniques include filtration, chemical demulsifier, heat treatment, and electrostatic emulsion [7,39].

The knowledge of the interaction between different shape deformations and their interaction strength is required to perceive the interactions between soft materials (bubbles or droplets) and liquid film. The most critical factors contributing to the dynamic drainage of thin films are as follows: the inertia of the drop/bubble, fluid viscosity, surface tensions, inertial separation, surface forces, and thin-film hydrodynamic behavior [6,7].

As mentioned, the coalescence process occurs when a droplet or bubble approaches the liquid-liquid surface and forms a thin film liquid layer between them, then starts draining to become unstable. At the early stage of the phenomenon, the liquid film is thick enough to apply Reynolds lubrication theory considering hydrodynamic interactions. It worth noting that intermolecular forces like van der Waals and electrostatic forces can be neglected in this stage [6,40]. In contrast, at the higher film thickness (where intermolecular forces have a dominant role), the intermolecular forces significantly affect the geometry deformation of the thin film [8,41,42]. The gravity effects in the film thickness at the range of micro/nanometer are negligible [6].

To model the droplet deformation at equilibrium condition mathematically, the Young-Laplace equation obtaining from the minimization of the isothermal Helmholtz surface energy is used. Moreover, the Stokes Reynolds Hydrodynamics method can be implemented to determine the hydrodynamic and thin liquid film drainage. The most important outcome can be derived from the mathematical modeling of thin liquid film to the time rate of droplet or bubble deformation and thin-film configurations. The main challenge in mathematical modeling and quantitative analysis is that droplets/bubbles in various length scales range from submicron to millimeter. For example, there are droplets/bubbles at the scale of a millimeter in a thin film with nanometer thickness, and their interaction leads to the deformation in orders of tens/hundreds of micrometers. Another challenge regarding the mathematical modeling of thin-film is the high non-linearity characteristic of the governing equations consisting of momentum balance, conservation of mass, stress balance, and kinematic boundary conditions at the film interface. In addition, the transient behavior and stable/unstable conditions of the thin film is another issue that should be considered in the modeling [6].

1.2.3. Lithography (micron- and nano-patterning)

Reducing the structure size on combined circuits using nano-sized patterns is the main challenge to the semiconductor industry [43]. Although numerous techniques have been employed to transfer micron and submicron-sized patterns to the surface of thin-film layers, photolithography is considered a widely used method for fabricating combined circuits in the electronics industry [44]. Photolithography, similar to other micro/nano-fabrication techniques, is an expensive and time-consuming multi-step method, which also uses environmentally harmful etching processes. The higher costs associated with high standards for devices and processes pose a challenge in the industry. Over decades, there have been tremendous efforts to use alternative patterning techniques that are more favorable in terms of process time and cost [45]. Some of these techniques are embossing methods [46], drop-on-demand and printing technologies [47–49], and lithography-induced self-assembly (LISA) in very thin single liquid films [17,19,50,51]. One of the key advantages of the LISA is the optically smooth surfaces generated due to the limited physical contact between the thin film and master mask. Furthermore, employing self-assembly indicates the ability to fabricate patterning to 3D structures, while either multilayer or serial direct-write methods were required in conventional microfabrication techniques to achieve 3D architectures [52]. Self-assembly, however, assets the demerit of detaching much of the control of final features from the lithographer. This can leads to undesirable impacts, like kinetics defects or thermodynamic or degraded final states. To solve this problem, the hybrid methods have been improved based on top-down templates for bottom-up patterns. One of the earliest examples of this method is liquid crystal templating (LC) using rubbed surfaces [53]. Several other examples show the existence of this process, especially in the area of block copolymer [54,55] and colloidal lithography [56]. In general, self-assembly is typically driven by an external force such as electrical [50,57,58], mechanical [17], intermolecular [59], thermal [60,61], or their combination [62]. This study seeks to highlight the thermocapillary (TC) forces for fabricating patterns on the surface of the polymer. TC-induced patterning of thin films is a pattern transfer that has received widespread attention due to its capacity to fabricate novel micro-and nano-sized features. In TC patterning, a nanofilm is placed between two plates heated through the lower surface and cooled at the top surface, as presented in Fig.1.2. Despite the application of TC-induced patterning, understanding the rationale behind the pattern evolution in thin micro-sized and nano-sized films is vital for further developing this method. There have been many works both experimentally and numerically

in the last two decades to investigate the effect of influential parameters such as temperature gradient, the initial film thickness, the thermal conductivity of polymer and bounding layer, and surface tension, which will be discussed in Chapter 2. The motivation for this thesis is that since the existing models cannot accurately predict the available experimental data in the literature, high accuracy nonlinear numerical model is needed for TC-induced patterning. Initially, the phase-field framework is employed to simulate the TC induced instability and pattern formation of the thin film. Using systematic study, it was shown that effective parameters impact the shape and size of the final features. However, further studies were needed to show the relationship between the characteristic wavelength obtained by linear stability (LS) analysis and the CFD model. Hence, the second part of this thesis focused on how the temperature difference, polymer thickness and the distance between two substrates impacts the characteristic wavelength of created pillars. This work was extended by finding a linear theoretical relation for the formation of secondary pillars when the width of protrusion increased beyond the characteristic wavelength. The polymer film in the first and second parts of the thesis are assumed to behave as a Newtonian fluid, while many polymer solutions and molten polymers are non-Newtonian fluids. Hence, the last part of this study focuses on a power-law model for the TC patterning of polymer films showing shear-thickening/thinning behaviors. This enables overcoming the limitation associated with assuming that viscosity is independent of shear rate.

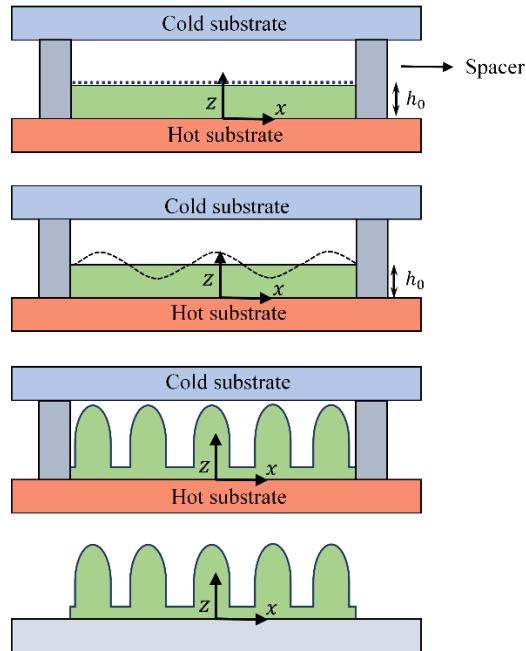


Figure 1.2. Schematic view of thin-film confined between two substrates. h_0 is the film thickness.

1.3. Scope and objectives

Given the above discussion, the objectives of this work are:

1. To solve *the full governing equations, including the continuity, Navier-Stokes, and energy equations, without any LW limit simplification.*, which enables minimizing the coarsening effects and fabricating well-ordered pillars using a patterned substrate. This objective involves investigating the impact of the height and width of protrusions, initial thickness, and polymer properties on the final shape of the pillars and processing time.
2. *To develop a model to show the relationship between the characteristic wavelengths of VOF and the LS analysis*, which includes studying the effect of different forces (viscous force, TC force, and the Laplace force) on the size and final shape of the pillars. This objective enables identifying the linear theoretical relations for forming secondary pillars based on the width of protrusions, the distance between them, and the inverse filling ratio.
3. *To improve the current linear models by considering non-Newtonian liquid films*, which involves examining the effect of local viscosity variation, a function of shear rate, on the dynamics, instability, and morphological evolution of shear-thickening/thinning fluids.

1.4. Thesis organization

This dissertation is organized in a paper-based format and will be presented in six chapters.

In Chapter 1, the potential technological applications associated with this research project are described along with their theoretical background. Moreover, the research goals and the scope of the work, the thesis's organization, and the contribution are provided.

In chapter 2, a detailed literature review for thermally induced patterning is provided, focusing on recognizing the limitations in the theoretical approaches available in the literature.

In chapter 3, a phase-field numerical model is presented to simulate the dynamic process of TC-induced patterning. A parametric study is done to study the effective parameters on the pillars' size and final shape. In chapter 4, the dynamics, instability, and morphological evolution of a thin liquid film investigated using a volume of fluid (VOF) numerical scheme that incorporates the Marangoni stress to model the gas-liquid interface deformation. The results obtained from VOF then compared with the “thin-film” (TF) model and LS analysis in many cases to find an accurate model for predicting the characteristic wavelength for the growth of instabilities.

In chapter 5, Linear and nonlinear analysis has been performed to investigate the thermally induced pattern formation in shear thinning and shear thickening liquid films

In chapter 6, the current study's main conclusions are described, and the recommendations for future work are presented.

1.5. Thesis contribution

Research on the subject has been mostly restricted to lubrication approximation which is only valid for the cases that the initial film thickness is smaller than the characteristic wavelength of induced instabilities. Since the long-wave approximation is no longer valid in the later stages of pattern evolution, we employed the full governing equations of fluid flow and the thermally induced Marangoni effect to track the interface between the polymer film and the air bounding layer. Initially, we used a phase-field framework to simulate the thin film's TC-induced instability and pattern formation. To fabricate well-organized features, a patterned plate is used to create a heterogeneous thermal field on the film interface. The effects of the protrusions' height and center distance are documented for creating compact and well-organized pillars.

Further investigations were required to reveal the relationship between the characteristic wavelength obtained from LS analysis and the CFD model. Hence, the second part of this thesis focused on how the temperature difference, polymer thickness, and the distance between two substrates impact the characteristic wavelength of created pillars. This work was extended by finding a linear theoretical relation for the formation of secondary pillars when the width of protrusion and the distance between them increased beyond the characteristic wavelength for both VOF and TF approaches. In all theoretical and numerical works in TC-induced patterning, the polymer film is assumed to behave as a Newtonian fluid. In contrast, many polymer solutions and molten polymers are non-Newtonian fluids. Hence, the last part of this study focuses on a power-law model for the TC patterning of polymer films showing shear-thickening/ thinning behaviors. This enables overcoming the limitation associated with assuming that viscosity is independent of shear rate. These analyses aim to enhance our understanding of the thermal-induced patterning mechanism and save time and cost in designing related experiments.

Chapter 2 - Literature review²

In 1999, the spontaneous formation of the nanopillars on the molten liquid film sandwiched between two substrates subject to a transverse thermal gradient was observed by Chou and Zhuang [50,63]. In their experiment, they studied solid polymeric nanofilms, which were first spun cast onto a cleaned silicon wafer with an initial film thickness, h_0 of approximately 100 nm. Subsequently, another silicon wafer was placed on this coated silicon wafer with the small air gap using spacers which determined the distance between two plates, d_0 , and this distance was different from several hundred nanometers to a micron. Fig. 2.1 shows a schematic of their experimental setup. The system was heated from below to above the glass transition so that the polymer was in a molten state. The heating cycle carried on for 5-80 min, and then molten polymer was allowed to solidify. After removing the top plate, the hexagonal arrays of pillars with a flat top and lateral spacing on the order of microns were revealed. There were several possible explanations at that time for the main physical mechanism that makes the polymer unstable. These possibilities will be discussed successively.

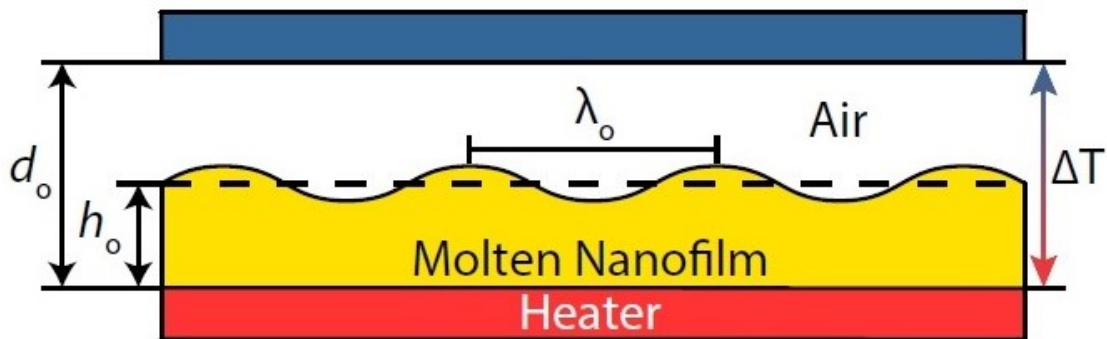


Figure 2.1. Basic nanofilm instability geometry [64]

² Parts of this chapter is based on Mohammadtabar et al. Phys. Fluids. 32 (2020) 024106, Ref. [96]

2.1. Previous instability studies: Surface Charge (SC) and Acoustic Phonon (AP) model

The surface charge (SC) model was initially proposed by Chou and Zhuang [50,63] to explain the formation of periodic nanopillar arrays. The SC model treats the molten polymer from the viewpoint of fluid dynamics in which it linearly becomes unstable to perturbations. They hypothesized that the SC present in the molten polymer and the resulting imaged charged on the substrates creates an electrostatic force as a destabilizing force on the interface to overcome the stabilizing force of surface tension. They also conducted a set of experiments without the top plate and observed that no pillars were formed after the polymer's solidification. Therefore, they noted that thermal gradients might be playing a role in addition to electrical effects. However, they did not deliberately apply a thermal gradient across the surface by installing a top plate's cooling. Moreover, since the initial polymer thicknesses were very small, the critical numbers for cellular convection due to the thermal gradient such as Rayleigh-Bénard and Bénard-Marangoni convection showed too small value instability to occur. Regardless, depending on the formation of the pillars due to temperature gradient remained unexplained.

At the same time, Schäffer and his group studied instability in the same geometry [65–67]. Once again, polymeric films were initially cast on the silicon plates and put in a confined system using spacers. The main difference from the tests of Chou and Zhuang is that the top substrates were cooled in the experiments of Schäffer et al. The temperature of the top cold plate was above the glass transition temperature of the polymeric nanofilms while the temperature difference with the top and bottom plates was around 10 °C. Both top and bottom plates were electrically grounded to rule out any electrical effect. Thus, the experiment setup was just imposed the transverse thermal gradient overnight, and then the polymer was solidified. As before, hexagonal arrays of the pillars were formed after removing the top plate. As Chou and Zhuang mentioned, Schäffer and his co-workers determined the Rayleigh-Bénard and Bénard-Marangoni numbers in their experiments, and they found that the numbers were much smaller than the critical ones needed for instability. To justify their results, they suggested acoustic phonon (AP) as the dominant mechanism for the growth of instabilities that relied on the low-frequency acoustic phonons and the resulting radiation pressure that is exerted on the thin liquid film. They first derived a complete hydrodynamic theory showing the dependence of instability to the radiation pressure and then applied linear stability

analysis to find the characteristic wavelength for the fastest growing mode, λ_0 . The characteristic wavelength was a function of the initial film thickness, temperature difference, thermal conductivity of the polymer and bounding layer, acoustic phonon coefficient, the distance between two plates, interfacial tension, and sound speed in the molten polymer. They conducted a set of tests to study the effect of influential parameters on the characteristic wavelength and then compared the obtained results with linear stability analysis. However, this comparison occurs in the later stage of pattern formation, where the polymer nearly reached the top plate, and it is outside of the linear regime. Furthermore, van der Waals interactions were not considered in the AP model.

2.2. Previous instability studies: Thermocapillary (TC) model

2.2.1. History

A century after Bénard explored cellular convection features in fluid layers subjected to a non-uniform temperature gradient, the liquid layer's thermal convection is still an intense investigation object. This phenomenon has practical relevance for different applications like heat transfer in cavity [68–71], and there is a fundamental interest in the self-organized pattern formation and evolution dynamics of liquid interfaces. With this scope, the surface tension-driven instabilities can be dominant for the liquid layers with a thickness of less than O (1.0 mm). Initiated by the seminal work of Pearson [72], many studies have been devoted to the Bénard-Marangoni (BM) in a fluid layer due to the presence of a temperature gradient at the interface while considering a temperature-dependent surface tension (TC-induced) [73–75]. In general, the TC phenomenon can be categorized into two fundamental modes called short-wavelength (SW) and long-wavelength (LW). The SW-induced mode creates cellular convection patterns, which can be grown without any surface deformation. This often happens in less viscous liquid film or relatively thicker. In contrast, the LW mode is always accompanied by a surface deformation that occurs more in thinner and/or viscous films [76]. The formed structures' amplitude is commonly much smaller than the pattern periodicity but may have the same height as the film thickness.

There have been several studies, both numerically and experimentally, to analyze the onset of instability and dynamics of a fluid layer experiencing SW-BM instability. To mention a few, Schatz et al. [77] visualized the pattern using shadowgraphy and then studied the hysteresis effect

during the heating and cooling process. Rahal et al. [78] used interferometry and infrared thermography to study the pattern dynamics, the deformation of the free surface, and the interfacial temperature distribution of SW-BM convection in a circular container. The SW-BM is applicable for a variety of practical problems like welding of steels [79], crystal growth [80], and convection under microgravity [81]. In terms of the LW-BM instability, VanHook et al. [82] conducted several experimental cases and theoretical studies for thick oil films with thickness in the order of 100 μm . They observed that the interface depressed or elevated locally depending on the film thickness and the oil and gas layers' thermal conductivities.

2.2.2. TC model for instability

Several years after Chou et al. [50], and Schäffer et al. [65], Dietzel and Troian started to study the issues existing in AP and SC models and reevaluate the assumptions of these models. They noted that phonon mean free paths in the range of 10-100 nm needed for coherent reflection from the AP model's polymer interface have only been calculated at temperatures much less than the glass transition temperature. They concluded that Acoustic Phonon is unlikely the main mechanism of pattern formation. They also repeated the assertion by Chou et al. and Schäffer et al. that the critical numbers that commonly govern the Bénard-Marangoni convection are very small in thin-film experiments for instability. Their theoretical and numerical work [18,19] has illustrated a new limit of the LW-BM instability, which is not governed by the traditional critical numbers. They presented a TC model. This model's underlying concept is that the temperature gradient across the interface results in non-uniform interfacial tension that exerts tangential TC stress at the polymer-air interface. They derived a relation for the characteristic wavelength of the fastest growing mode, λ_0 , as a function of plate separation, initial film thickness, and temperature difference. They then compared the characteristic wavelength obtained TC model to the experimental data of Schäffer et al. and showed that the TC model had a good agreement with the experimental data to that point and could play a vital role, if not dominant, role in the thermally induced pattern formation. After that, McLeod et al. did a set of experimental wavelength measurements to more study the main mechanism of pattern formation [51]. By improving the practical measurement techniques, he compared the characteristic wavelength obtained from the AP, SC, and TC models more accurately, and they found that the measured wavelength was most consistent with the TC model.

2.2.3. Pattern replication through localized film deformation

There have been several works into controlling structure deformation as a potential manufacturing technique. In these studies, the top flat plate was replaced by a patterned plate. The presence of a pattern mask will create non-uniform temperature leads to localize deformation.

Chou and co-workers were the first groups that demonstrated pattern replication using the top patterned mask with a triangle, a square, and the text "PRINCETON" [50,83]. In all these cases, pillar arrays were formed in the patterned mask's shape, and no deformation was observed in the regions outside the mask. In a similar study, Chou et al. showed that the film completely covered the patterned mask if it was adjacent to the initial film height, and the formed pillars merged into a continuous structure [63]. Schäffer et al. [17,65] similarly illustrated pattern replication of square arrays, hexagonal arrays, and lines with pillar sizes around 500 nm. In all cases mentioned above, the pillars were permitted to grow until they reached and contacted the top mask. Therefore, the formed pillars had a flat top due to their contact with the top plate. McLeod and Troian stopped the experiment before the pillars touch the top mask to create a square array of curved lenses [51]. The ability to control film deformations using the top patterned masks opens a new horizon for the fabrication of nano-sized structures with smooth surfaces.

2.2.4. Nonlinear analysis in thermal-induced patterning

The majority of studies are focused on the nonlinear analytical approach to model the interface dynamics and provide an insight into the timescale and length associated with the thermal-induced patterning process. The nonlinear model relies on the lubrication approximation leading to the so-called "thin-film" [18,19,84]. In fact, the governing equations, including continuity, momentum, and energy balance equations, are simplified using low Reynolds number ($Re \ll 1$) and long-wavelength approximation, which describes the ratio of polymer thickness to lateral scale is less than 0.1, results in a 4th order nonlinear equation called the thin film equation. By substituting the interface height with the sinusoidal perturbations in the thin-film equation and neglecting all the obtained nonlinear terms, the linearized predictions were found [19,62,84]. The thin-film solution showed the exact location of the interface at any time of the pattern formation. Nazaripour et al. [84] employed both linear and nonlinear analyses of AP and TC models to determine the mechanisms responsible for instability growth and pattern formation in confined heated nanofilms.

The results showed that both models predict the formation of pillars and bicontinuous features for very low and high filling ratio, which defined the ratio of the distance between two plates to the initial film thickness. However, the obtained features in the TC model were smaller than those in the AP model. Regardless of the good accuracy of the predictions achieved by the thin-film equation and its low computational time and cost, this model suffers from its limitations in predicting the high aspect ratio interface deformation. Thus, a high accuracy nonlinear numerical model was required for TC-induced patterning. The influence of interfacial slippage on the surface instability of elastic thin films subjected to van der Waals-like surface interactions was studied [85]. Recently, different numerical techniques were applied to track the free interfaces, such as phase-field, volume of fluid (VOF), and level set models [86–88]. The phase-field model was considered as one of the most accurate approaches for simulating many types of microstructure evolution processes. This method is based on a diffuse-interface description developed by van der Waals [89] and then Cahn and Hilliard [90] independently. This method has also been used to study various multiphase problems, such as the spreading process of microdroplets [91], droplet impact on homogeneous surfaces [92,93], and electrohydrodynamic multiphase flow [94,95]. Moreover, phase field can be incorporated in other physical fields like thermal and electric fields [95], [96]. The VOF approach has also attracted significant interest due to its incredible accuracy in simulating of two-phase flow system with a sharp interface. This method has been commonly used in modeling the hydrodynamics of bubbles rising in a liquid [97,98]. Tomiyama et al. [99] showed that the shapes proved the high accuracy of the VOF approach in modeling the shapes and terminal velocities of a single rising bubble by comparing them to the published experimental data. Kawaji et al. [100] studied the two-dimensional modeling of a Taylor bubble rising in a stagnant fluid-filled tube. Given the high accuracy of the phase-field and VOF approaches, these models are selected in the present study to investigate the thermally induced patterning of the heated nanofilms numerically.

2.3. Challenges of previous models and thesis objectives

The reduction of the feature size from micron to submicron level and fabricating well-organized pillars using TC-induced patterning are found to be challenging due to the complex underlying mechanisms of this phenomenon. The existing models, the SC and AP models, failed to predict the characteristic wavelength obtained from the experimental data where the film thickness is less

than 100 nm. TC model can predict more accurately the characteristic wavelength; however, it is an empirical model. Moreover, most works rely on the assumption of the very low ratio of deformation amplitude to its lateral size. They also treated the molten polymer as a Newtonian fluid in their analysis. Therefore, a more comprehensive TC-patterning model is required to overcome these shortfalls. This thesis demonstrated that employing the phase-field and VOF models, as high-accuracy approaches for the two-phase flow problems, and solving the full governing equations without any LW limit simplification can predict more complex and even smaller structures. The effect of polymer properties, the relative thermal conductivity of polymer and air, filling ratio, and temperature gradient on the dynamics, instability, and pattern formation of the TC-induced patterning has been studied. Moreover, the effect of the Marangoni and Capillary number on the time evolution and the shape and size of pillars were investigated. Finally, a mathematical model is proposed to study the impact of the power-law rheology on the structures.

Chapter 3 - A numerical study for thermocapillary induced patterning of thin liquid films³

3.1. Introduction

Thermal-induced patterning of a thin liquid film is a promising method to fabricate micro/nano-sized structures that rely on thermocapillary (TC)-induced instabilities and pattern self-organization. Due to its merits in micro-contact, leading to easy demolding and low cost compared to other conventional micro-patterning techniques, it has become a topic of interest in the community. Micro- and nano-fabrication are essential parts of innovative solutions in the area of microelectronics, optoelectronics, and micro/nano-fluidics. Although numerous techniques have been employed to transfer micron and submicron-sized patterns to the surface of thin-film layers, photolithography is considered a widely used method for fabricating combined circuits in the electronics industry [101]. Photolithography, similar to other micro/nano-fabrication techniques, is an expensive and time-consuming multi-step method, which also uses environmentally harmful etching processes. The higher costs associated with high standards for devices and processes pose a challenge in the industry. Over decades, there have been tremendous efforts to use alternative patterning techniques that are more favorable in terms of process time and cost [45]. Some of these techniques are embossing methods [46], drop-on-demand and printing technologies [47–49], and lithography-induced self-assembly (LISA) in very thin single liquid films [17,19,50,51]. The latter is typically driven by an external force such as electrical [50,57,58], mechanical [17], intermolecular [59], thermal [60,61], or their combination [62]. One of the key advantages of the LISA is the optically smooth surfaces generated due to the limited physical contact between the thin film and master mask. However, a major problem with these self-organized pattern formation methods is the complex mechanism and nonlinearity in the growth of instabilities and pattern formation. Thus, a large number of investigations have focused on the behavior and characteristics of the thin liquid film in hydrodynamic instabilities approaches [18,19,58,62].

³ Reproduced from Ref. [96], with the permission of AIP Publishing

A century after Benard [102] discovered cellular convection structures in fluid layers exposed to non-uniform temperature distribution, thermal convection in the liquid layer is still a subject of research, especially in the self-organized pattern formation of thin liquid films. The surface tension-driven instabilities can be dominant for the liquid layers with a thickness of less than 1.0 mm. Initiated by the work of Pearson [72], many studies have focused on the Bēnard-Marangoni (BM) instability in a fluid layer due to a transverse temperature gradient at the interface while considering a temperature-dependent surface tension effect or TC [73–75]. The TC-induced instabilities are categorized into two fundamental modes: short-wavelength (SW) and long-wavelength (LW). The SW-induced mode results in a cellular convection pattern, which can be developed without any surface deformation. These commonly occur in relatively thicker or less viscous liquid films or a combination of both. In contrast, the LW mode is accompanied by a surface deformation that is more dominant in thinner and/or viscous films [76]. The majority of early studies focused on the TC-induced instabilities of heated thin films [13,103], where the generated features on the surface had a small height-to-width ratio. In addition, capturing the formed features was not of practical interest.

Chou and Zhuang [63] created micron-sized features on the molten liquid film using a high transverse thermal gradient. They discovered the formation of raised columnar features (pillars) in a thin molten polymer film that was confined with another plate with a small air gap. Although the main interest was the pattern formation via electrically induced instabilities, it was found that the features were also formed when there was no electric field applied to the system. The surface charge (SC) model was initially proposed as an underlying mechanism for pattern formation, which relies on the image charge-induced electrohydrodynamic instabilities that might be present in the molten polymer film. Later on, the same set of experiments was conducted by Schaffer et al. [17,104] to show that pillars are also formed after the grounding of substrates and liquid films. This result ruled out the electrostatic effect and acoustic phonons (AP) models as hypothesized alternatives to SC. The AP model relies on the radiation pressure caused by acoustic phonons at low frequencies. The AP model was accepted in the community until the recent study of Dietzel et al. [19] and McLeod et al. [51]. They observed the formation of periodic pillar arrays when a nanofilm is subjected to an external transverse thermal gradient. They proposed the LW-TC model as the responsible mechanism for the growth of instabilities. Their result showed that it is not necessary to achieve a critical Marangoni number for the onset of instabilities [76]. This was

despite the conventional BM instabilities. They performed systematic experiments and in-situ visualizations to verify the LW-TC model as the main reason for the growth and amplification of instabilities, which rules out both SC and AP models.

Despite the application of TC-induced patterning, understanding the rationale behind the pattern evolution in thin micro-sized and nano-sized films is vital for further development of this method as a micro/nanofabrication technique. The study of interface dynamics and TC-induced pattern formation process is of considerable interest to researchers [50,104]. However, a direct simulation for the interface evolution remaining a challenge for the community. This is a multiphysics process that includes fluid flow from micro- to macro-scales, TC flow due to the interfacial tension inhomogeneity at the interface, and two-phase flow interface tracking. The early works focused only on the linear analytical approach to simulate the dynamic interface process and provide an insight into the length and time scales associated with the TC-induced patterning process [18,19]. The linear model relies on the Stokes flow and the lubrication approximation leading to the so-called “thin-film equation”. The linearized predictions are found by replacing the interface height with the sinusoidal perturbations and neglecting all the resulted nonlinear terms [19,62,84]. In the majority of the works concerning the dynamics, instability, and dewetting of heated thin films, the morphological evolution of the interface and film rupture is found by solving the thin film equation, which relies on the validity of long-wave (LW) approximation [13,103]. The governing equations, including mass, momentum, and energy balance equations, are simplified using LW approximation, leading to a 4th order nonlinear equation called the thin-film equation. The transient solution provides the exact location of the interface at any time of the evolution. Despite the good accuracy of the predictions achieved by this model and its low computational time and cost, the thin-film model suffers from its limitations in predicting the high aspect ratio interface deformation, which might not be the case in the TC patterning studies. The thin-film model relies on the assumption of a very low ratio of deformation amplitude to its lateral size, limiting the accuracy of the predictions for the low aspect ratio deformation at the interface. Thus, a high accuracy nonlinear numerical model is needed for TC-induced patterning.

The spatiotemporal evolution of the thin liquid film involves multiphase flow interface tracking, which can be modeled using computational fluid dynamics (CFD). These models track the interface between two phases, such as volume of fluid (VOF), Level Set, and Phase Field models

[86–88]. Among these methods, the phase-field approach is considered one of the most accurate models for simulating several types of microstructure evolution processes. The phase-field method is based on a diffuse-interface description developed by Van der Waals [89] and then Cahn & Hilliard [90] independently. The temporal microstructure evolution is illustrated by both Cahn-Hilliard nonlinear diffusion equation and the Allen-Cahn (time-dependent Ginzburg-Landau) [105] equation. The Phase Field is formulated to minimize the sum of surface energy and bulk energy of the flow. While it has more underlying physics compared to the Level Set method, it is also shown to be more accurate when an appropriate mesh is generated at the interface [94]. The Phase Field model resolves the tri-phase contact line singularity by defining a diffuse-interface and present the Fluid-Solid Interaction by applying chemical energy diffusion instead of shear stress [106]. This method has also been applied to investigate different multiphase problems, such as droplet impact on homogeneous surfaces [92,93], spreading process of microdroplet [91], and electrohydrodynamic multiphase flow [94,95]. Furthermore, Phase Field can be incorporated in other physical fields such as thermal field and electric field [95]. Hence, the Phase Field is selected for this analysis to investigate the thermally induced patterning in heated liquid films numerically.

Thus far, the majority of research has focused on using a flat plate as a top substrate that leads to the formation of hexagonal or random pillar arrays [17,84]. However, to obtain other types of packing, minimizing the coarsening effects and fabricating well-ordered pillars, a patterned substrate is used. The filling ratio, the ratio of polymer thickness to substrate separation distance, plays a vital role in the final shape of structures and secondary pillar appearance [62]. Moreover, Karapetsas et al. [107] studied the thermocapillary-driven flow of a droplet on a nonuniform heated patterned surface. It was shown that proper design of the substrate wettability could be used to manipulate droplet dynamics. Therefore, the wettability and adhesion forces between the liquid film and solid plates also affect the pattern formation mechanism and final shape and features.

Here, we presented the phase-field model framework as a multi-phase flow interface tracking approach to simulate the TC-induced instability and pattern formation of thin films. In the proposed approach, the full governing equations, mass continuity, Navier-Stokes and energy are solved without any LW limit simplification. We study the effect of both physical and chemical properties of bounding plates on the size and shape of final structures. For the first part, we show that we can obtain a well-ordered nanostructure based on an interplay between the height and width

of protrusions and the pattern of plate periodicity and initial thickness. We also study the formation of a secondary feature from the residual polymer after the growth of primary pillars. The effect of the properties of polymer-like thermal conductivity on processing time is also studied. In the second part, the effect of polymer wettability of bounding plates by changing the contact angle on the interface evolution at later stages of pattern formation is investigated. These analyses aim to enhance our understanding of the thermal-induced patterning mechanism and save time and cost in designing related experiments.

3.2. Mathematical Model

A two-dimensional schematic of the ultrathin polymeric film with the initial thickness of h_0 is shown in Fig. 3.1. The liquid film is placed between two plates that are heated (T_H) through the lower surface and cooled at the top surface (T_C). The gap between the liquid film and the top plate is filled with air. The patterned top plate (mask) is used to create a non-uniform temperature distribution on the polymer-air interface. The protrusions on the top mask have a height of H and width of W_2 and spacing of W_1 . The separation distance between the two substrates is set to D . Although the density and viscosity of molten polymer may change with temperature gradients, the liquid film is assumed to be incompressible and Newtonian with constant viscosity evaluating at the mean working temperature ($\mu = 30 \text{ Pa s}$).

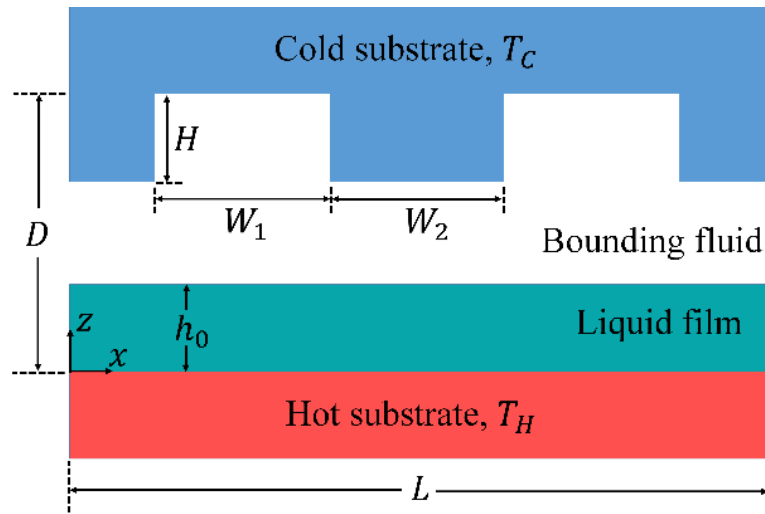


Figure 3.1. 2D schematic of the ultrathin liquid film placed between the top (cold) and bottom (hot) substrates, where $T_H > T_C > T_g$. Here, T_g is the glass transition temperature of the polymer film.

3.2.1. Governing Equations and Boundary Conditions

3.2.1.1. Fluid flow and heat transfer

Mass conservation and time-dependent momentum balance equations are used to describe the velocity field and pressure distribution within the fluid layers.

$$\nabla \cdot (\mathbf{u}_i) = 0 \quad (3.1)$$

$$\rho_i \left[\frac{\partial \mathbf{u}_i}{\partial t} + (\mathbf{u}_i \cdot \nabla) \mathbf{u}_i \right] = \nabla \cdot [-p_i \mathbf{I} + \mu_i (\nabla \mathbf{u}_i + (\nabla \mathbf{u}_i)^T)] \quad (3.2)$$

Here, the subscript “ i ” denotes the fluid phase (1 for air and 2 for the liquid film).

To find the temperature distribution in the system, the energy equation (Eq. 3.3) is also incorporated in the model,

$$(\rho c_p)_i \frac{\partial T_i}{\partial t} = \nabla \cdot (k_i \nabla T_i), \quad (3.3)$$

Where c_p is the heat capacity and k denotes the thermal conductivity of fluid phases. The convective mode of heat transfer in our system is negligible (Biot number, $Bi = \frac{h_0 h_{convection}}{k_p} \ll 0.1$) as the film thickness in the TC process is in micron and submicron ranges. Therefore, it is neglected. The fluid flow is coupled with the energy balance equation to incorporate the effect of temperature on the velocity field at each time step. The thermophysical properties of the polymer are constant with the exception of density, which is calculated using the Boussinesq approximation. However, the effect of density variations within the thin film on the thermal-induced patterning process is negligible compared to the effect of the induced surface tension gradient along the interface.

The thermocapillary effects are incorporated in this model by coupling the fluid flow and the energy equations based on the Boussinesq approximation that implements the effect of temperature on the velocity field. This model ensures that the density differences only affect the flow field through buoyancy forces.

3.2.1.2. Phase-field equations

The Phase-field method, as a powerful tool for multiphase flow, is used to investigate the TC effect on dynamics and spatiotemporal evolution of the film interface. In this method, a phase parameter φ is defined to distinguish the two phases. Here, $\varphi = 0$ denotes one phase and $\varphi = 1$ represents

another phase. The polymer-air interface is considered a thin diffusive layer, which has the phase parameter φ between 0 and 1. The interface can be determined by tracking the profile of $\varphi = 0.5$. By defining the phase parameter, fluid phase properties of density (ρ) and viscosity (μ) are considered as a function of φ . Therefore, unified governing equations are solved for two phases, that is a polymer, air, and their interface [108].

First, a free energy (f_{free}) is defined for the system, which takes the Ginzburg-Landau form [109],

$$f_{free}(\varphi) = \frac{1}{2}\lambda|\nabla\varphi|^2 + \frac{1}{4}\frac{\lambda}{\xi^2}\varphi^2(1-\varphi)^2 \quad (3.4)$$

where ξ is the polymer-air interface thickness and $\lambda = 6\sqrt{2}\xi\sigma$ (σ is the surface tension coefficient). Eq. 3.4 shows the energy density at each point in two domains. Based on Eq. 3.4, this energy is zero when $\varphi = 0$ or $\varphi = 1$. However, at the interface, where φ is between 0 and 1, this energy is nonzero and, it originates from the surface tension (σ). The chemical potential (G) is determined from the differential of the free energy density with respect to φ ,

$$G = \frac{\delta f_{free}}{\delta\varphi} = \lambda \left[-\nabla^2\varphi + \frac{\varphi(\varphi-1)(\varphi-1/2)}{\xi^2} \right] \quad (3.5)$$

Tracking the deformation of the polymer-air interface needs the evolution of φ . The general energy equation of the phase parameter is the Cahn-Hilliard equation [94], which describes the conservation of the phase parameter:

$$\frac{\partial\varphi}{\partial t} = -\mathbf{u} \cdot \nabla\varphi + M\nabla^2 G \quad (3.6)$$

Here, \mathbf{u} is the velocity field, and M is the mobility of the diffusion effect. The term on the left-hand side of Eq. 3.6 is the transient term of φ , while the first term on the right-hand side denotes the convection effect, and the second term represents the diffusion effect.

3.2.1.3. Boundary conditions

A two-dimensional computational model is used to solve the governing equations based on the finite element method (FEM) using COMSOL Multiphysics. The simulation domains shown in Fig. 3.2 consists of 2 subdomains (one for each phase), 7 boundaries, and 22 vertices. Initially, domain-1 and domain-2 are occupied by air and thin liquid film, respectively. The bottom substrate, which is shown by a red line, is exposed to a hot source. The top substrate (Blue line) is exposed to a cold source at constant temperatures. For the momentum equations, the no-slip

boundary condition is used for the top and bottom substrates. It is essential to define the periodic boundary conditions at edges 3, 4, 5, and 6. Sources 3 and 4 correspond to destinations 5 and 6, respectively. The red line in Fig. 3.2 indicates the initial fluid interface at boundary 2 and pressure point constraint applied at locations a and b, as two ends of the air-liquid interface. Table 3.1 summarizes all the boundary conditions used for the simulation for the momentum, the phase-field, and the energy equations.

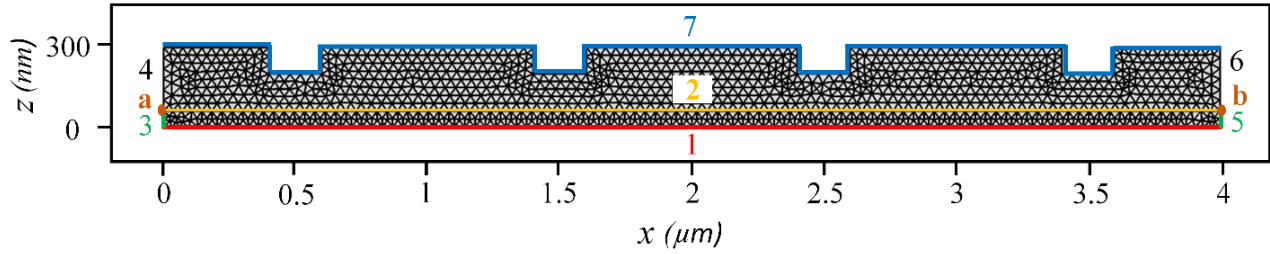


Figure 3.2. Schematic diagram introducing the boundary condition and mesh of the 2D model (not to scale).

Table 3.1. List of boundary conditions considered in the simulations.

Boundary number	Momentum	Phase-field	Energy
1	No-slip	$\frac{\partial \varphi}{\partial n} = 0$ or $\theta = \frac{\pi}{2}$	T_H
3 – 6	Periodic	Periodic	Periodic
7	No-slip	$\frac{\partial \varphi}{\partial n} = 0$ or $\theta = \frac{\pi}{2}$	T_c

At the interface between fluid phases, a balance is considered for normal and tangential stresses, where the shear stress is proportional to the temperature gradient on the interface. This is achieved using the Marangoni effect multiphysics feature in COMSOL,

$$\mathbf{t} \cdot \{[-P\mathbf{I} + \mu(\nabla\mathbf{u} + (\nabla\mathbf{u})^T)] \cdot \mathbf{n}\} = \nabla_s \sigma \cdot \mathbf{t} \quad (3.7)$$

where σ is interfacial tension that is approximated as a linear function of temperature,

$$\sigma = \sigma_0 - \sigma_T(T - T_0) \quad (3.8)$$

Here, σ_T is the temperature derivative of the surface tension, σ_0 is the reference surface tension and T_0 is the reference surface temperature. Table 3.2 shows the constant parameters used by the models in this study as a base-case [110,111]. The range of geometrical parameters and the material properties used for the simulation are also adopted from the previous experimental studies focusing on the TC-induced patterning and reported [19,112].

Table 3.2. Parameters and constants used in TC simulation

Parameters	Value	Unit
Density of air (ρ_a)	0.829	kg/m ³
Viscosity of air (μ_a)	1.81×10^{-5}	Pa.s
Thermal conductivity of air (k_a)	0.0225	W/m K
Density of polymer (ρ_p)	1000	kg/m ³
Viscosity of polymer (μ_p)	30	Pa.s
Thermal conductivity of polymer (k_p)	0.13	W/m K
Surface tension of polymer (σ)	45×10^{-3}	N/m
Interfacial tension gradient (σ_T)	10^{-4}	N/m K
Temperature difference (ΔT)	50	K
Thermal conductivity ratio (k_p/k_a)	5.2	---
Initial thickness of the polymer film (h_0)	100	nm
Distance between top and bottom substrate (D)	300	nm
Height of the protrusions (H)	100	nm
Width of the protrusions (W_2)	200	nm
Periodic length of the template (W_1)	800	nm

To compare the dominant forces in the system, the non-dimensional numbers of Reynolds, Capillary, Grashof, Marangoni, Bond and Prandtl number are defined and their order of magnitude are tabulated in Table 3.3.

Table 3.3. The order of magnitude estimates for characteristic numbers.

Nondimensional numbers	Equation	Order of magnitude
Reynolds number (Re)	$Re = \frac{uD}{\vartheta}$	$10^{-7} - 10^{-8}$
Grashof number (Gr)	$Gr = \frac{g\beta\Delta TD^3}{\vartheta^2}$	$10^{-21} - 10^{-22}$
Marangoni number (Ma)	$Ma = \frac{[(1 - k_r) + k_r\tilde{D}]^2}{k_r\tilde{D}}$	$10^0 - 10^2$
Capillary inverse (Ca ⁻¹)	$Ca^{-1} = \left[\frac{\sigma[(1 - k_r) + k_r\tilde{D}]^2}{\sigma_T k_r \tilde{D} \Delta T} \right]$	$10^1 - 10^2$
Bond number (Bo)	$Bo = \frac{\rho g D^2}{\sigma}$	$10^{-7} - 10^{-8}$
Prandtl number (Pr)	$Pr = \frac{C_p \mu}{k}$	$10^4 - 10^5$

** u is the characteristic velocity ($u = \frac{\alpha}{D}$) and \tilde{D} is the filling ratio ($\tilde{D} = \frac{D}{h_0}$).

The very low order of magnitude of Reynolds number (Re) indicates that the inertial (convective terms) effect is less dominant compared to the viscous effects leading to the Stokes flow of the fluid. The order of Marangoni number (Ma), which represents the relative strength of the TC force to the viscous force, and Capillary inverse (Ca⁻¹), which represents the relative strength of the surface tension forces acting on the interface to the viscous forces, are large enough, so the dominant forces in the thin-film study are thermocapillary, viscous, and Laplace force. Prandtl number (Pr) is of the order of $10^4 - 10^5$. Bond number (Bo), which is the ratio of gravitational force to surface tension force, is small enough so we can ignore the effect of gravity as well as the density variation.

3.2.2. Validation and Verification

To examine the optimum grid size, four different grids are generated using Physics-controlled mesh. The results for the interface height growth over time are presented in Fig. 3.3. These results show that the mesh generated with 2.78×10^4 elements was sufficiently accurate for film interface height tracking.

The simulation results are also compared with experimental data reported by Dietzel and Troian[19] and the linear stability (LS) analysis method to ensure the validity of our numerical model. The value of λ_{max} obtained from experiments and LS are compared with our simulation results for the case of $h_0 = 100$ nm, $D = 300$ nm, $H = 100$ nm, $W_2 = 5$ μ m, and $\Delta T = 46$ K with one long protrusion which mimics the same conditions as that used in the literature [19]. The spatiotemporal evolution of the film is shown in Fig. 3.4. As can be seen, three features are formed under the large protrusions at approximately 2.01 μ m distances. Experimental results with a similar configuration showed that $\lambda_{max,exp} = 2.04$ μ m. However, the LS method overpredicts the value of λ_{max} by a factor of ~ 2 compared to the experimental data ($\lambda_{max,ls} = 4.52$ μ m). Hence, the results obtained from the CFD model are in excellent agreement with the reported experimental results and can provide a better prediction of characteristic wavelength than the LS analysis widely used in current literature.

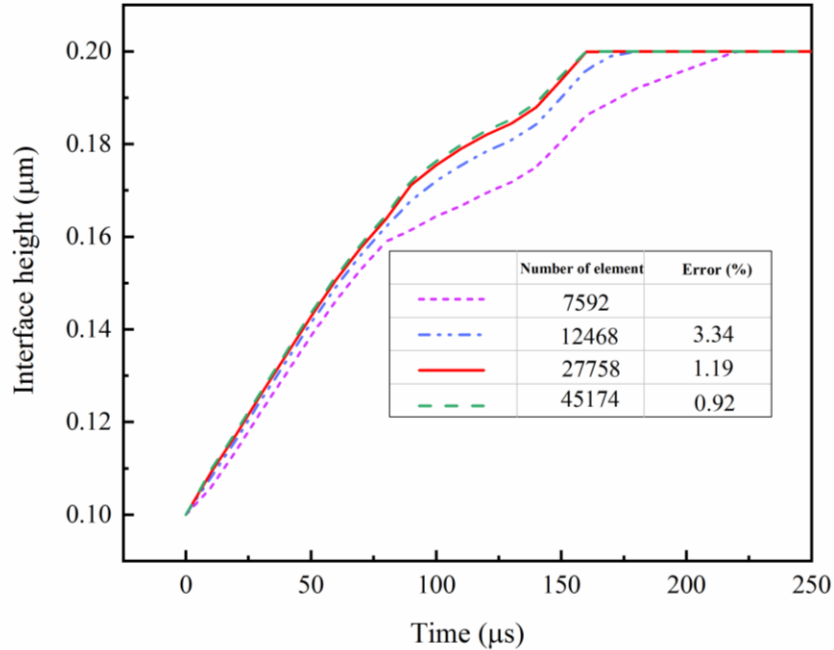


Figure 3.3. The Effect of grid size on transient growth of interface height, $h_0 = 100$ nm, $d = 300$ nm, $W_1 = 800$ nm, $W_2 = 200$ nm, $H = 100$ nm and $\Delta T = 50$ °C.

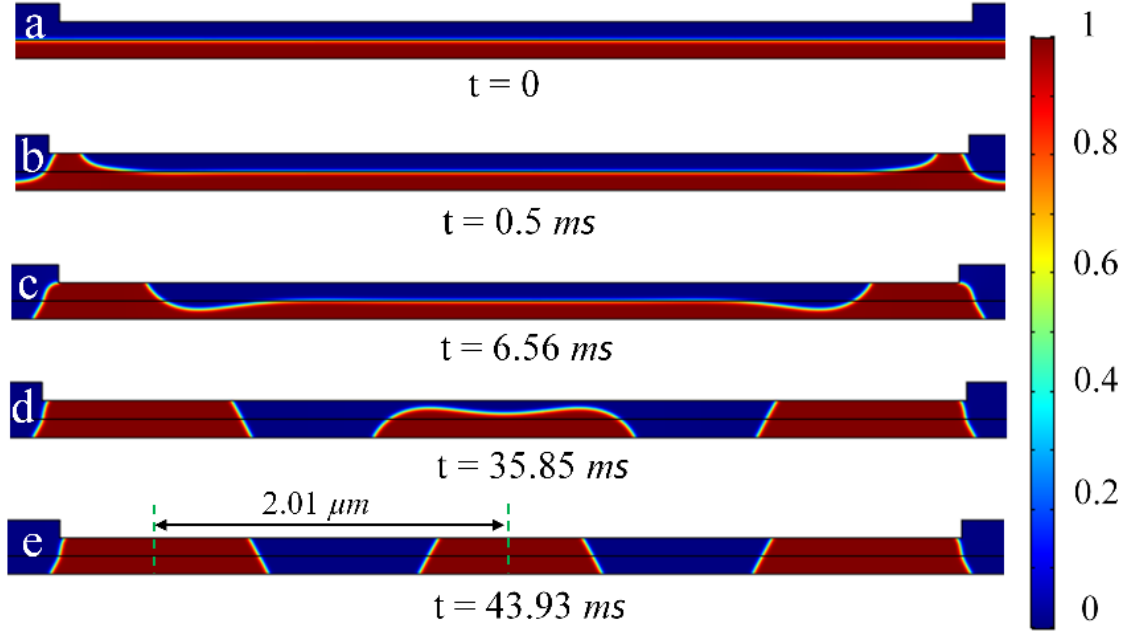


Figure 3.4. Temporal evolution predictions of air–polymer free surface under $h_0 = 100$ nm, $d = 300$ nm, $W_2 = 5000$ nm, $H = 100$ nm and $\Delta T = 46$ °C.

3.3. Result and Discussion

A periodic pattern is used on the template to control the pattern formation and create well-ordered pillar arrays. This pattern generates a periodic temperature gradient along with the air-polymer interface. The lower temperature gradient magnitude corresponds to the areas under the protrusion, and the higher magnitude corresponds to the areas under the cavity. This non-uniform temperature gradient at the interface generates the surface tension non-homogeneity, which ultimately unbalances the stress distribution at the air-polymer interface and leads to a pattern evolution. The dynamics, instability, and morphological evolution of the interface depends on several process parameters such as temperature gradient, the protrusion dimensions and wettability, air gap thickness, the initial film thickness, and thermal conductivity of polymer film. It should be noted that the contact angle for all cases is $\frac{\pi}{2}$ except for the last section (section 3.4). In section 3.4, different contact angles from 0 to π are considered to study the effect of the relative energy of liquid film on the contacting plates in the shape of the final structure.

3.3.1. Pattern Formation and Temperature Gradient

First, the time variation in temperature gradient and interfacial tension are studied as the main driving force in thermally induced patterning. The snapshots of temperature distribution across the polymer and the air layer at a given instance in time are shown in Fig. 3.5. Here, the liquid polymer is heated at the bottom surface and cooled at the top surface. The initial temperature condition at $t=0$ (Fig. 3.5a(i)) is set such that the temperature of polymer and air is that of the top cold mask. It only takes 40 ns for the interface to feel the exposed temperature gradient (Fig. 3.5a(ii)), and the temperature distribution reaches steady-state conditions at $t=100$ ns (Fig. 3.5a(iv)). This time scale for the heat transfer within the thin film is significantly smaller than that of the pattern evolution reported in thin films [18].

In Fig. 3.5b, the temperature profile is plotted along the x-direction at the interface ($z = 100$ nm) and near the protrusions ($z = 190$ nm). The temperature distribution shows that the gradient in temperature at the interface due to the patterned mask is much smaller than the gradient exposed near the protrusions, which is due to the very low thermal conductivity of the air bounding layer. However, a non-uniformity in the temperature distribution exists at the interface, which induces TC instability. Moreover, when the interface moves towards the patterned mask, it experiences a higher thermal gradient that enhances the TC stress. In most of the molten polymers, the surface tension linearly decreases as temperature increases [51,84]. Hence, the interfacial tension is higher than its surroundings, where the temperature underneath the protrusion is smaller than the neighboring area. That is, the areas with lower interfacial tensions are pulled by the regions with higher interfacial tension leading to a rise of the interface under the protrusions. The TC stress is an interfacial force, and the polymer viscosity transfer this load through the polymer film, giving rise to a fluid motion and fluid flow.

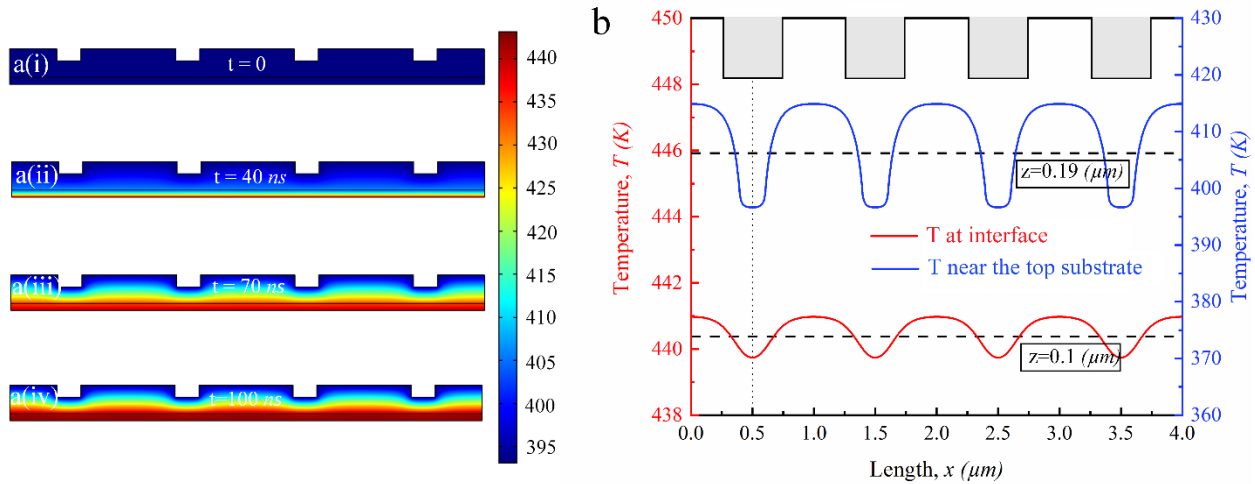


Figure 3.5. The unsteady contour of temperature at a(i) initial stage, a(ii) 40 ns, a(iii) 70 ns, and a(iv) 100 ns. (b) The temperature gradient profile along with the interface and the line near the protrusions at the steady-state condition. The protrusion width of $0.2 \mu\text{m}$ and the height of $0.1 \mu\text{m}$.

The interface contour plots and the interfacial height growth profile over time are shown in Fig. 3.6. In the contour plots, the red color represents the polymer film, and the blue color shows the area filled by air. It is assumed that the liquid film destabilized with the initially flat interface (Fig. 3.6a(i)). It has been shown that the initial shape of the interface affects the dynamics and pattern evolution process [58]. At the early stages, the temperature gradient is small at the interface due to the larger gap between the interface and the top plate. Thus, the TC force is small, and the interface deformation is slow.

Fig. 3.6a(ii) shows a snapshot of the interface deformation under the protrusions after $60 \mu\text{s}$. Over time the uplifted liquid film experiences a larger TC force as the interface approaches the top plate, and it is exposed to a higher thermal gradient leading to faster interface evolution towards the protrusions (Fig. 3.6a(iii)). Subsequently, the interface reaches the top plate at $t=155 \mu\text{s}$ (Fig. 3.6a(iv)). This process continues until the polymer wets the entire surface of the protrusions, which reveals the exact replication of top substrate stamp periodicity shown in Fig. 3.6a(v). In the linear stability analysis (refer to Appendix A, Eq. A6), it takes $23 \mu\text{m}$ for the polymer to touch the top substrate, which is shorter than the processing time of the phase-field method. The wetting mechanism of the top plate with polymer film depends on the relative energy of the contact surfaces and the polymer film, which is controlled by contact angle settings. The setting for the wetting properties of the top plate highly affects the shape of the final formed patterns, which will be discussed later in this study. The spatial heterogeneity of the surface tension force in the TC

patterning process induces the non-uniform pressure distribution shown in Fig. 3.6b. This uneven pressure distribution is responsible for the flow mechanism and interface deformation in the TC patterning process. Fig. 3.6b(i) shows the initial pressure and velocity distribution. As time progresses, the pressure increases in the area under the protrusion as air is squeezed out of that region. This is due to the circulation effects in the gap between the protrusions, which forces the polymer upwards to create the pattern, as shown in Fig. 3.6b(i) to 3.6b(iv). The velocity vector data indicates the flow recirculation in two sides of the protrusion and the resulting fluid flow from the neighboring area to the region under the protrusion. As the interface deforms and moves upward, the flow entrainment continues. The tracking of interface height evolution of a pillar over time is presented in Fig. 3.6c. The entire process can be divided into three stages. At stage 1, the effect of the surface tension is small compared to the TC force. Thus, the polymer deforms rapidly (Fig. 3.6a(ii)). The pillar keeps growing until it enters stage 2, where the surface tension force is comparable to TC force (Fig. 3.6a(iii)). Although the slope of the pattern growth slowly decreases at this stage, the structure height increases due to negative fluid diffusion from the neighbor area toward the pillars. This leads to thinning of the residual layer of film between each pillar. At stage 3, the polymer touches the top substrate (Fig. 3.6a(iv)) and makes the well-ordered structures (Fig. 3.6a(v)). The process is mostly affected by the relative surface energy of the mask and the polymer film.

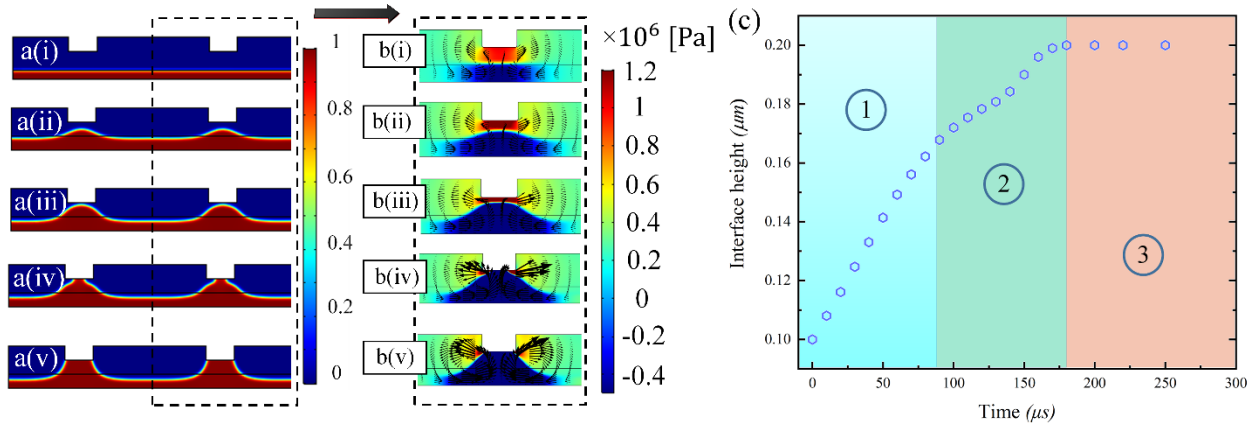


Figure 3.6. Thermally-induced hierarchical structures for a patterned template. 2D snapshots of the film interface, $h_0 = 100$ nm, $D = 300$ nm, $W_1 = 800$ nm, $W_2 = 200$ nm and $\Delta T = 50$, at different stages of the evolution process, a(i) initial, a(ii) 60 μ s, a(iii) 141 μ s, a(iv) 141 μ s and a(v) 200 μ s, (b) 2D snapshots of the pressure contour and velocity vector at different stages of the evolution process, (c) The tracking of the interface height of a pillar.

3.3.2. Influence of polymer thickness, driving force, and thermal conductivity

3.3.2.1. Effect of initial polymer thickness

In the self-organized micro/nano-patterning techniques, the initial film thickness and the ratio of film thickness to electrodes separation distance (filling ratio) dominate the dynamics, instability, and patterns forming on the film. Moreover, the formed patterns based on these techniques rely on thin liquid film deformations, either using the de-wetting mechanism or electrically induced patterning. Here, we present how changing the polymer thickness affects the pattern formation in the TC-induced patterning process, while the temperature gradient is controlled by protrusion geometry, including width, height, and periodicity. Keeping all the parameters the same as the base-case shown in Fig. 3.4, the polymer thickness is varied so that the filling ratios (h_0/D) are 0.2 (Fig. 3.7a), 0.33 (Fig. 3.7b), and 0.5 (Fig. 3.7c). Snapshots of patterns formed at a quasi-steady state are shown in Fig. 3.7. At $h_0/D = 0.2$, constituting a low filling ratio, single pillars are formed touching the top substrate with no residual polymer left between the pillars. Increasing the filling ratio results in pillars with a lower aspect ratio (height to width ratio of a pillar), while the lower plate remains wet. At higher filling ratios, the interface touches the top plate at the early stages, as shown in Fig. 3.7c with $h_0/D = 0.5$. At this ratio, the interface deformation is an undulation in the film. We further investigated the effect of the filling ratio by changing the separation distance between plates. The trend was similar, with a lower filling ratio resulting in pillars and higher filling ratios resulting in undulations. Further details are provided in Appendix A1.

3.3.2.2. Effect of The Driving Force

We continue by looking at the effect of changing temperature gradient as one of the main driving forces in pattern formation. Fig. 3.8 shows the temperature gradient magnitude over the liquid-air surface along with tracking of the interface height over time for temperature differences of 10 K, 50 K, and 100 K. By increasing the temperature difference in the transverse direction, the temperature gradient magnitude along the interface would also increase, leading to a higher surface tension gradient. Therefore, the time required for the interface to touch the top plate decreases, implying a fast pattern replication. As shown in Fig. 3.8b, it takes ~ 3 ms for the liquid film to touch the top template at a temperature difference of 10 K, whereas this time for a temperature difference of 50 K and 100 K is 175 μ S and 75 μ S, respectively. Higher temperature gradient results in a

higher TC-induced force on the interface through the pattern evolution and faster interface deformation. Moreover, the processing time in transferring TC-induced patterns depends on the dependency of the liquid viscosity on temperature. Here, it is assumed that the viscosity of the film is constant throughout the pattern formation process, and it does not vary with temperature.

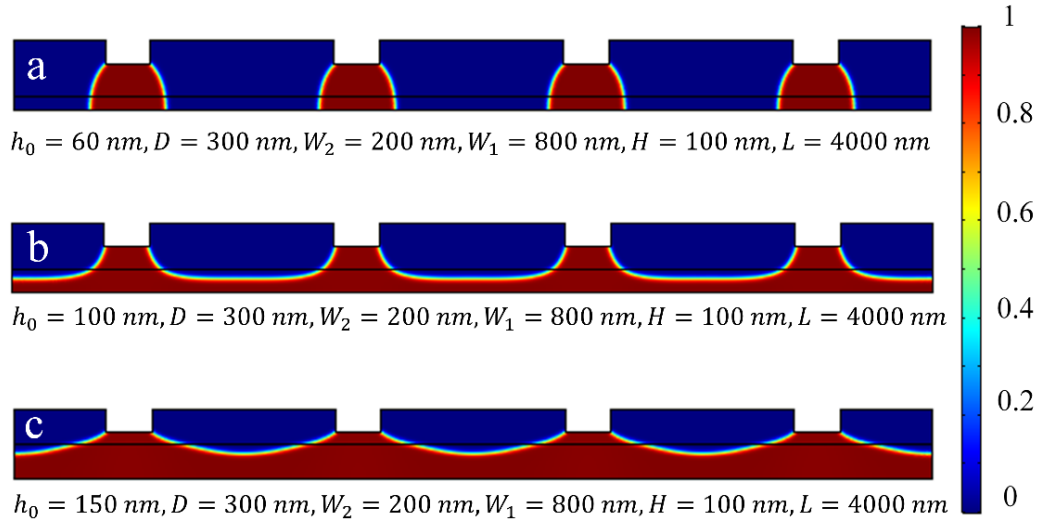


Figure 3.7. The changing trend of pattern formation, induced by thermal gradient with the filling ratio factors of (a) 0.2, (b) 0.33, and (c) 0.5.

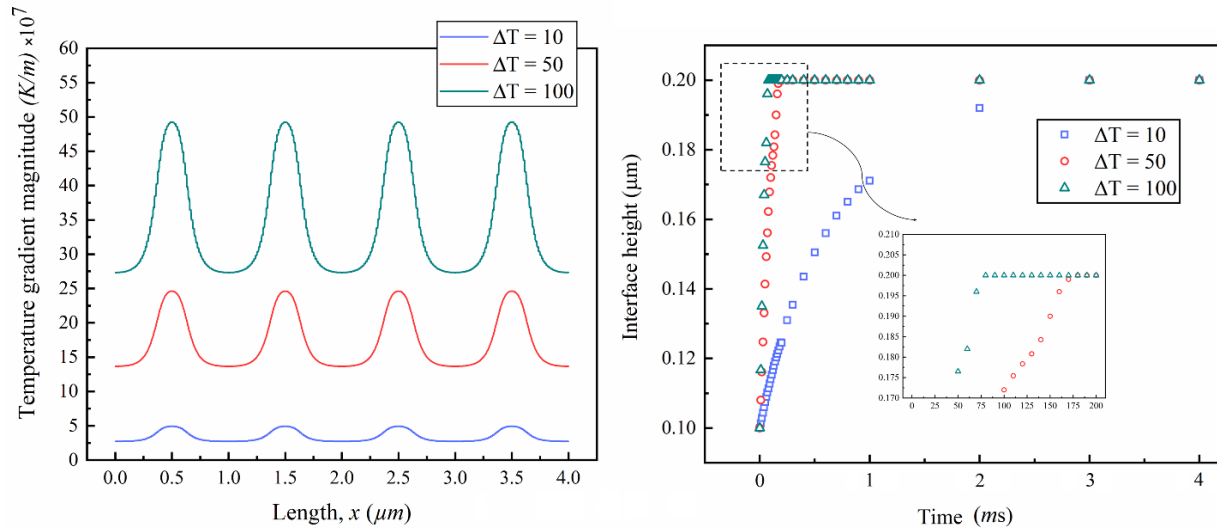


Figure 3.8. The implications of varying temperature gradient on (a) the polymer-air interface and (b) the transient behavior of the interface height.

3.3.2.3. Effect of Thermal Conductivity

The thermal conductivity of layers affects the non-uniformity of temperature distribution and interfacial tension along the interface. This includes the conductivity of layers involved in the system, such as plates, polymer film, and protrusions in the mask. It is assumed that the confining plates are not affecting temperature gradients since their temperature is uniform. Here, the ratio of thermal conductivity of the polymer film to the air layer ($K_r = K_p/K_{air}$) is varied to investigate the effect of thermal conductivity of layers on the pattern formation process. By increasing K_p , the temperature at the interface increases, which leads to a uniform temperature distribution at the interface. Thus, the temperature gradient along the interface and the resulting TC force are less than the cases with smaller thermal conductivity ratios. Furthermore, the shape of the formed features is not affected by K_r variations. However, tracking height of the interface over time (Fig. 3.9) revealed that the interface deformation is slower when K_r is larger resulting in a longer time for the film to touch the top plate. As discussed earlier, there are three stages for the process of growing pillars. At the initial stage, decreasing the thermal conductivity of the polymer causes the fluid to flow faster towards the top protrusions. Although the rate of pattern growth slowly decreases for all cases near the top protrusions, the structure height increases due to negative fluid diffusion from neighboring regions toward the pillars (stage 2). At the final stage, the fluid with the lowest K_r touches the top wall earlier than the other two cases.

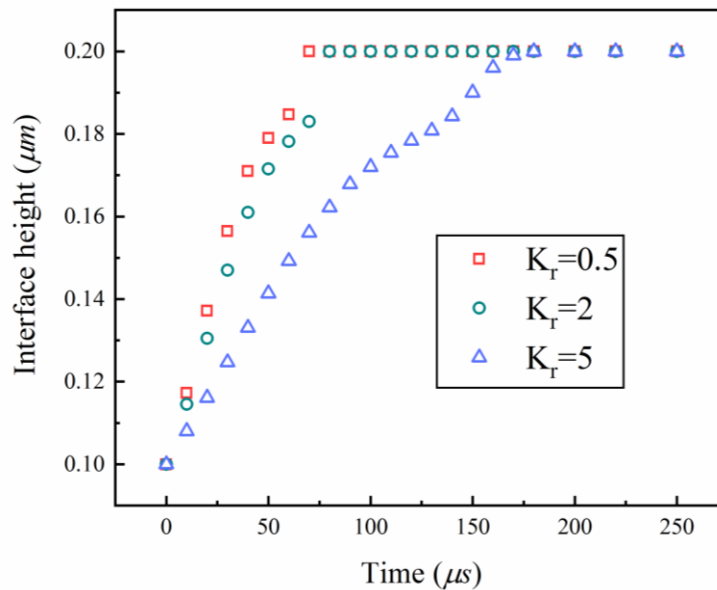


Figure 3.9. The tracking of the interface height of a pillar at different ratios of thermal conductivity (K_r).

3.3.3. Impact of Geometry on the Pattern Formation

It was previously shown that microstructures and nanostructures on the patterned mask could be replicated on the polymer film. The size, shape, and period of the resulting pattern are determined by the geometry of the used mask as the top cold plate.

3.3.3.1. Effect of protrusions width

The width of top protrusions affects the size and number of pillars forming in the thermal-induced patterning process. Fig. 3.10 demonstrates the pattern formation of a 100 nm thin liquid film under a temperature difference of 50 K using a protruded top substrate with a height of 100 nm and three different widths of 200 nm, 400 nm, and 800 nm. The gap spacing is set to 300 nm. By increasing the width from 200 nm to 400 nm, the size of pillars increases while only one pillar is formed under each protrusion. However, increasing the width of protrusions led to the formation of twin pillars under the protrusions (Fig. 3.10a(iii)). In the case of $W_2 = 800$ nm, there are two regions with high-temperature gradients (points A and B in Fig. 3.10b), and thus the polymer moves up in these two regions at the initial stage of pattern formation. Consequently, two twin pillars were observed at the end of the process. However, in the case of $W_2 = 400$ nm, there is only one region with a high-temperature gradient (point C), leading to the formation of one pillar.

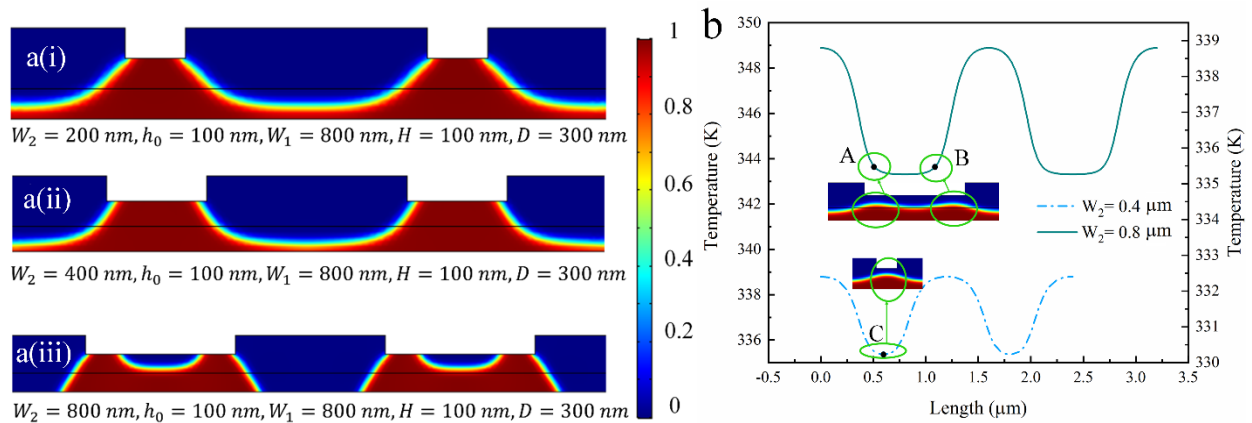


Figure 3.10. (a) The changing trend of pattern formation induced by thermal gradient with the different protrusion width, a(i) 200 nm, a(ii) 400 nm and a(iii) 800 nm, (b) The temperature gradient profile for two cases, a(ii) and a(iii).

It is believed that the spacing between the pillars forming in TC-induced instabilities are correlated to the characteristic wavelength found using the LS analysis. Moreover, it is shown that the size of the protrusions is correlated to the predicted characteristic wavelength [18,51,84]. The reason is that the thermal gradient exposed to the film interface is higher at the corners of the protrusions leading to a considerable gradient at the interfacial tension on the underneath interface. The instabilities at the interface begin and grow at these peaks located on the sides. When the width of the protrusion is small, case (i), these two peaks merge at very early stages of growth of instabilities leading to one larger undulation. However, when the protrusion width is higher than the characteristic wavelength for instabilities growth, then the instabilities grow without merging, leading to twin pillars (case (iii)).

3.3.3.2. Effect of the distance between protrusions

Another factor affecting the fidelity of pattern replication in TC-induced patterning is the center-to-center distance of protrusions. Fig. 3.11 shows the temporal evolution of a thin polymeric film under the effect of a square protruded (side length of 100 nm) top substrate with a stamp periodicity of 2 μm . On the application of temperature gradient, the generated non-uniform temperature distribution destabilizes the free surface (Fig. 3.11a(ii)) and triggers a motion in the polymer due to the thermocapillary pressure gradient. Finally, the interface evolution results in the formation of primary pillars (Fig. 3.11a(iii)) under the protrusions. Once these pillars touch the top protrusions, the remnant layer between two pillars moves toward the top substrate due to the combined effect of temperature gradient and surface tension forces (Fig. 3.11a(iv)). However, complete de-wetting happens if the polymer content in the remnant layer is significantly low (Figure 3.11a(v)). This observation is of great interest since the full de-wetting process, and its subsequent dynamics are significantly affected by the surface properties. At the quasi-steady state, the secondary pillar is formed between the protrusions (Fig. 3.11a(vi)).

The remnant layer connected to the pillars via a concave meniscus and the pathway of evolution in this layer begins with the film rupture at the meniscus. The TC force acting on the interface close to the meniscus leads to a diffusion of fluid from thinner to thicker regions of the film leading to a film rupture at the meniscus (Fig.3.11 a(iii) and a(iv)). After the fragmentation, the remnant film encounters both Laplace pressure and TC stress which tend to retract the film and forms a

more circular shape pattern like a microdroplet. However, the TC stress acting on the interface is more severe at the corners where contact line exists due to a higher gradient of film thickness. This leads to a sharp increase in the film thickness at the edges and a dimple formation at the center of the remnant layer (Fig.3.11 a(v)). The droplet, which is called the secondary pillar, becomes increasingly circular due to surface tension and TC force (Fig.3.11 a(vi)). Depending on the initial filling ratio and applied thermal gradient, the secondary pillar may also touch the confining cold plate (shown in Fig. 3.4). The same qualitative pathway of morphological evolution was also seen for secondary pattern formation in electrohydrodynamic patterning [12,16,30].

Tracking the interface height over time for both primary and secondary pillars is presented in Fig. 3.11(b). Initially, the liquid film flows, and the interface rises under the protrusions to form the primary pillar. With the residual polymer between the pillars, the secondary pillars emerge ($t = 5.83$ ms) and they quickly grow with the primary pillars touching the top substrate. The main reason behind the formation of the secondary pillar is that the distance between the two protrusions in this case is greater than the characteristic wavelength. Thus, the formation of secondary pillars is affected by the thickness of the remnant layer, wetting properties of the substrate, and temperature gradient magnitude in those regions. The height of the secondary pillar also depends on the amount of the residual polymer between the formed pillars or the initial film thickness.

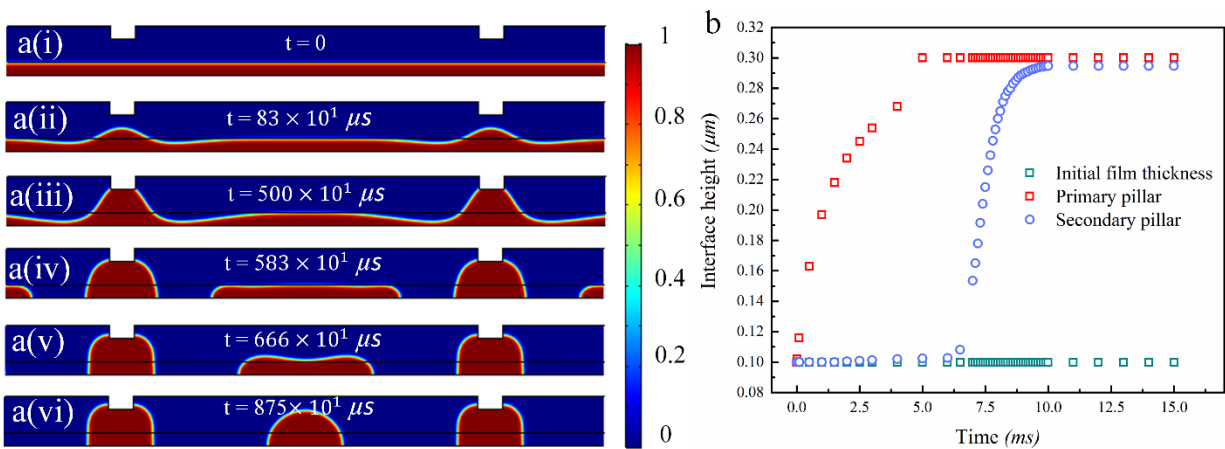


Figure 3.11. Thermally induced hierarchical structures for a patterned template. 2D snapshots of the film interface at different stages of the evolution process, a(i) initial, a(ii) 0.83 ms, a(iii) 5 ms, a(iv) 5.83 ms, a(v) 6.66 ms and a(vi) 8.75 ms. (b) The tracking of the interface height of both primary and secondary pillar.

3.3.3.3. Effect of protrusions height

The effect of protrusion height of the template, H , on thermal-induced patterning is examined by simulating the deformation process of the liquid film for various templates. As previously discussed, the template structure modulates the temperature distribution, which leads to non-uniform TC force leading to deformation of the interface. The distance between the bottom substrate and tip of the top protrusions ($D - H$) is fixed at 400 nm to eliminate the effect of the filling ratio. For a quantitative investigation of the effect of templates, the process time at which the liquid film touches the protrusions represents the growth rate of the pattern. A longer process time indicates a slower growth rate. Increasing H , at a constant $D - H$, results in a higher temperature gradient exposed to the interface that leads to higher TC forces. As shown in Fig. 3.12, a template with a large protrusion height resulted in a shorter process time. Moreover, the effect on growth rate becomes insignificant for larger H . When the protrusion height (H) equals the distance between the bottom substrate and the tip of protrusions ($D - H = 400$ nm), further increasing the protrusion height has insignificant effects on the process time. This is due to a decrease in temperature gradient at the interface.

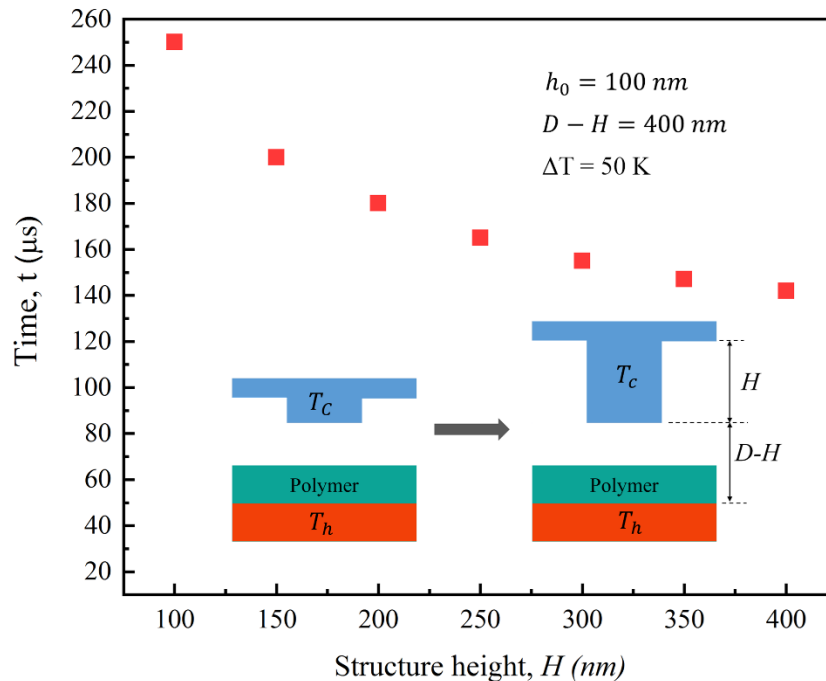


Figure 3.12. Relationship between the processing time and the template structure

For thermal-induced patterning, it is always beneficial to shorten the processing time. Thus, a template with a large protrusion height is required to boost the non-uniformity of TC force and thus the growth rate. However, fabricating a template with this high aspect ratio protrusions significantly enhances the challenges and costs associated with the process.

3.3.4. Effect of Wettability of Protrusions

In previous sections, it was shown that the dynamics of spatiotemporal evolution in TC instability systems, with the patterned top substrate, is sensitive to several physical parameters, such as film thickness, gap distance, thermal conductivity of polymer, and temperature gradient magnitude. In these cases, the contact angle, which is the angle formed by the intersection of the polymer-substrate interface, was kept constant at 90° . The contact angle between the polymer film and solid substrates represents the surface interaction, indicating the relative strength of the surface energy between the polymer and the substrate. Hence, it could significantly affect the thin film instability, shape, and size of patterns. According to Young's equation [113], the contact angle θ and the surface tension of the film (σ_f), the interfacial tension between film and substrate (σ_{sf}), and the surface free energy of the solid substrate (σ_s) are related as $\sigma_s = \sigma_{sf} + \sigma_f \cos \theta$ (shown in Fig. A2 at Appendix A). The interactions between the liquid film and the underlying solid substrate leads to the film deformation and formation of various meso-scale structures [59]. Depending on the material properties of the liquid film and the solid plates, the interactions between each layer and the resulting force on the interface vary, which affects the equilibrium contact angle. In contrast to the free-standing films where the initial deformations are driven by the competition between the surface energy of films and the substrate, in the TC-induced patterning, the later stages of the deformation (where tri-phase contact line appears) are affected by the wettability properties of the film and bounding plates.

In thermal-induced patterning, the lower plate should remain wetted and the upper plate must be non-wetting to make the demolding process easy. In this study, in order to show the significance of the interactions between the film and solid plates on the final shape of structures, the contact angle between the film and upper and lower bounding plates is varied. Partially wettable surfaces of contact angles 30° and 60° as well as non-wettable surfaces of contact angles 120° and 150° were investigated in Fig. 3.13. A surface with a 90° contact angle was also considered for comparison. The contact angle of both the top and bottom substrates was set to the same value.

Fig. 3.13(b-d) show that complete de-wetting takes place for contact angles more than 60° while Fig. 3.13(a) shows a remnant polymer layer after the patterns touched the upper substrate for the most wettable surface case. This can be attributed to the strong adhesive force between the lower substrate and the polymer that overcomes the cohesive viscous forces keeping the polymer all together. This observation is only valid for that particular temperature difference between the top and lower substrate and highly depends on the combined effect of the thermal gradient and surface tension forces. Another observation would be the tendency of the polymer to wet the top protrusions. Once these patterns touch the top protrusions, an upward movement of the residual polymer is experienced due to the combined effect of thermal gradient and surface tension forces. Fig. 3.13 shows that various shapes of the polymer can be created depending on the wettability of the top protrusions. This observation is of significant interest since the contact angle considerably influences the subsequent dynamics in the complete wetting and /or de-wetting process.

The micro-pattern and nano-pattern formation rely on the dewetting mechanisms in the thin liquid film, which is a novel branch in soft lithography [59]. As stated previously, the wettability of the substrates may change the pattern formation mechanism in nanofilms. Here, we showcased an example of such effects within the TC-induced patterning framework.

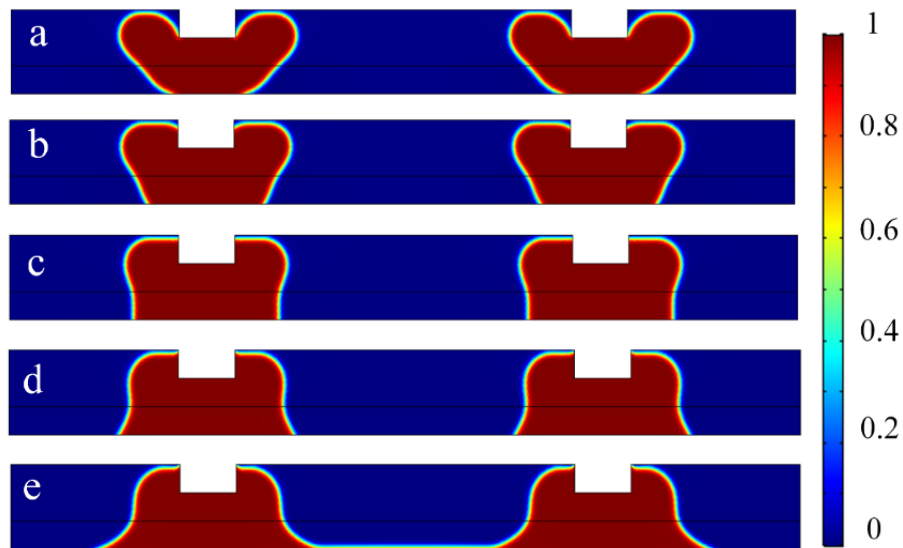


Figure 3 13. The structure of the pillars for a base-case at different contact angle (a) 30, (b) 60, (c) 90, (d) 120 and (e) 150.

3.4. Conclusion

A phase-field numerical model was used to simulate the dynamic process of thermal-induced patterning. In this model, the deformation of the liquid film in a two-phase flow system was defined by the phase parameter. Using the phase-field model, the dynamic process of thermal-induced patterning was studied while highlighting the effect of various parameters. It was found that the temperature gradient in the interface can considerably affect the dynamic process. For a larger temperature gradient, the liquid film grew rapidly until it touched top protrusions. In terms of the effect of polymer's thermal conductivity, the thermocapillary force decreased due to the reduction of the temperature gradient. Thus, the processing time was longer. As protrusion height increased, it was observed that a large protrusion height could enhance the growth rate and could decrease the processing time. However, a further increase in the protrusion height became insignificant. Examining the effect of the distance between two protrusions revealed that as the primary pillars touched the top substrate, the residual polymer between pillars has formed secondary pillars. This indicated that pillars could form under protrusions and between them, depending on their spacing distance. This enables reducing the number of protrusions. Moreover, it was determined that the contact angle was critical in establishing the pillars' final structure. Well-ordered pillars appeared when the surface had higher surface energy compared to the liquid film. These findings improve our understanding of thermal-induced patterning, which may be a useful guide for experiments. In this chapter, it was found that the increase in the width of protrusions and the distance between them beyond a critical value can lead to a secondary pillar. Hence, there is a need for a parametric study to find the threshold for these parameters. Since the phase field model has a convergence issue in large domain sizes, the VOF model will be employed to do a systematic investigation. Moreover, the thin film approach that provides a non-linear solution of TC patterning will be applied. Then, the obtained results from different numerical models (VOF, TF, and LS analysis) were compared.

Chapter 4 - Two-layer modeling of thermally induced Bénard convection in thin liquid films: Volume of fluid approach vs. thin-film model⁴

4.1. Introduction

Fabrication of micro- and nano-sized structures is an innovative solution for microelectronics, optoelectronics, and micro/nano-fluidic applications. A variety of techniques have been employed to fabricate micron and submicron-sized patterns to the surface of thin-film layers, such as photolithography, electron-beam lithography, and nanoimprint lithography [114,115]. Although these methods are widely used to manufacture combined circuits in the electronics industry [101], these techniques' multi-step fabrication process is both time- and cost-intensive. Furthermore, they consist of an etching step, which is an environmentally destructive and pollution-causing process. An impressive amount of work has been done to find an alternative method to address limitations associated with conventional micro/nano-manufacturing [17,45,116–118]. These methods include hot embossing [46], drop-on-demand and printing technologies [47–49], and lithography-induced self-assembly (LISA) of thin liquid films [17,19,50,51]. The latest method is typically driven by an external force such as electrical [50,57,58,119,120] mechanical [17], intermolecular [26,59,121,122] thermal [60,61,123–125], or their combination [22,23,62,126]. One of the remarkable advantages of LISA is its ability to create an optically smooth surface due to the limited physical contact between the thin film and master mask, which is of interest in optoelectronic applications. Despite the simplicity in applying LISA to create micron and nano-sized features compared to the conventional soft lithography techniques, the non-linearity and complexity of the governing mechanisms are not trivial as it relates to the growth of instabilities and the pattern formation. Hence, a significant amount of effort is required to understand the underlying mechanism of such instabilities and to harness them to create well-ordered features with consistent shape and sizes [18,19,22,58,62,127].

⁴ Reproduced from Ref. [139], with the permission of AIP Publishing

A typical LISA system consists of a molten polymer thin film, or polymer solution, on a substrate. In the films with micron and submicron-sized thickness, the intermolecular interactions are relatively strong, and the film may undergo interfacial deformations, leading to the creation of holes or drops. In such conditions, the material properties of the film, substrate, and the bounding layer define the dominant intermolecular forces [24], dewetting mechanisms, and consequently the shape and size of structures [59,128]. In the electrically induced patterning, the interface deformation is triggered by applying an electric field, which results in the application of net electrostatic force on the interface [129]. Similarly, there are instabilities caused by temperature gradients in the fluid layer at the interface, which is referred to as Bēnard-Marangoni (BM) instability. If the temperature gradient at the interface results in non-uniformity of the surface tension at the interface, the BM instability is referred to as the thermocapillary (TC) effect [73–75,130–136]. The TC-induced instabilities are categorized into two fundamental modes: short-wavelength (SW) and long-wavelength (LW). The former leads to a cellular convection pattern without any nonlinear surface deformations, and it occurs commonly in relatively thicker or less viscous liquid films or a combination of both. In contrast, the LW mode is accompanied by a surface deformation appearing in thinner and more viscous liquid films [76]. Most of the previous studies that investigated the TC-induced instabilities of heated liquid films have focused on thermal convection [102] resulting from a density gradient across the film. As such, the SW mode of instabilities led to cellular convection structures with small height-to-width ratios [13,103].

Early studies on the TC-induced patterning of thin films are primarily devoted to exploring the corresponding mechanism for interface deformation. In the TC-induced patterning processes, the solid thin layer of film is initially heated to above its glass transition temperature (T_g). Then, the transverse temperature gradient is applied using the controlled cooling of the film from the top plate. Chou and Zhuang [63] were the pioneers who reported the creation of micron-sized features on the ultrathin molten polymer films using high transverse thermal gradients. They introduced the surface charge (SC) model, based on the image charge-induced electrohydrodynamic instabilities, as the underlying mechanism for TC-induced instability. Soon later, Schaffer et al. [17,104] reported the formation of pillars after the grounding of substrates and liquid films. They introduced the acoustic phonons (AP) model as an alternative to SC. According to the AP model, the low-frequency acoustic phonons generate significant destabilizing radiation pressure. The AP model was well accepted in the scientific community until recent studies by Dietzel et al. [19] and

McLeod et al. [51], who proposed the TC model to predict the spontaneous formation of periodic pillar arrays on the molten nanofilms exposed to a transverse thermal gradient. In contrast to SC and AP models, the TC model is applicable to any nanofilm and represents an extreme range of BM instability for LW fluctuations, where gravity forces are absent, and TC forces overcome the stabilization by capillary forces [51]. While the previous efforts were limited to the AP and TC prediction of instabilities, based on the initial stages of pattern formation, we recently studied the non-linear stages of pattern formation for both AP and TC models under long-wave approximation limit [84].

Nevertheless, the previous studies are mainly limited to simplified governing equations using long-wave approximation either in linearized or non-linear modes [84,112,137]. A majority of these studies utilized an analytical approach to evaluate the length and time scales in the TC-induced patterning process [18,19]. This non-linear model, called the “thin-film” (TF) equation, relies on Stokes flow and the lubrication approximation. The linearized predictions can be obtained by replacing the interface height with the sinusoidal perturbations and ignoring non-linear terms [19,62,84]. However, neglecting the higher-order non-linear terms is a critical drawback, preventing effective prediction of the dynamic process of the thermal-induced patterning. A non-linear numerical model with high accuracy is required to address this challenge, which is the focus of this study.

The spatiotemporal evolution of the thin liquid film includes multiphase flow interface tracking, which is commonly modeled by computational fluid dynamics (CFD). These models track the interface between two phases and primarily include volume of fluid (VOF), Level Set, and Phase Field models [86–88,96,107]. In particular, the VOF method has attracted significant interest owing to its remarkable accuracy in the modeling of two-phase flow systems with a sharp interface. This method has been mostly implemented in examining the hydrodynamics of bubbles rising in a liquid [97,138]. Tomiyama et al. [99] proved the high accuracy of the VOF method in simulating the shapes and terminal velocities of a single rising bubble as compared to the published experimental data. Kawaji et al. [100] reported new findings for the two-dimensional simulation of a Taylor bubble rising in a stagnant liquid-filled tube. Given the high accuracy of the VOF method, it is selected in the present work to numerically investigate the thermally induced patterning of heated liquid films.

Here, we studied the dynamics and the interface evolution of nanofilms exposed to the transverse thermal gradient, either using a flat or patterned top mask. The patterned top mask resembles the localized cooling of the thin film, which triggers the instability locally and induces the motion in the film. The characteristic wavelength was obtained by VOF, TF model, and linear stability (LS) analysis for many cases. First, we derived a correlation, which shows the relation between the characteristic wavelengths obtained by VOF and LS analysis. Moreover, we not only considered the effect of distance between the top and bottom substrates on the characteristic wavelength, but we also investigated the impact of the initial film thickness and temperature difference. This will advance the initial empirical model developed by Dietzel et al.[19], which constitutes a novel contribution to the field. We studied the impact of the width of the top mask protrusions on the final shape of the structures, the number of pillars, and the processing time. It was demonstrated that, by smart adjustment of width and height of protrusions, as well as the initial thickness of the polymer and the distance between the protrusions, well-organized pillars could be formed. We also investigated the formation of secondary pillars, originating from the residual thin film after the growth of primary pillars. The presented analyses aim to provide an insight into the mechanism of thermal-induced patterning and to save time and cost in designing related experiments.

4.2. Mathematical Model

A three-dimensional (3D) schematic of the ultra-thin liquid film with the mean initial thickness of h_0 is shown in Fig. 4.1 [139]. The liquid film and air bounding layer are placed between two plates that are heated from the bottom boundary (T_H) and cooled from their top boundary (T_C). It is assumed that the heat dissipation within the confining plates is negligible. The film is assumed to be flat and initially stable. The TC-induced instabilities are originated from imbalances at the temperature distribution along with the interface. This non-uniformity of temperature distribution either can be achieved using the patterned upper plate - inhomogeneity of the upper plate, or by imposing the random perturbations on the film interface. In the present study, the patterned upper plate is used to induce the TC instabilities. Using a patterned top plate, the non-uniform temperature distribution is achieved on the air-polymer interface, where the thickness of the air gap affects the cooling rate. As shown in Fig. 4.1, d_1 and d_2 are the separation distances between the plates, where $\Delta d = d_1 - d_2$ is the protrusion's height.

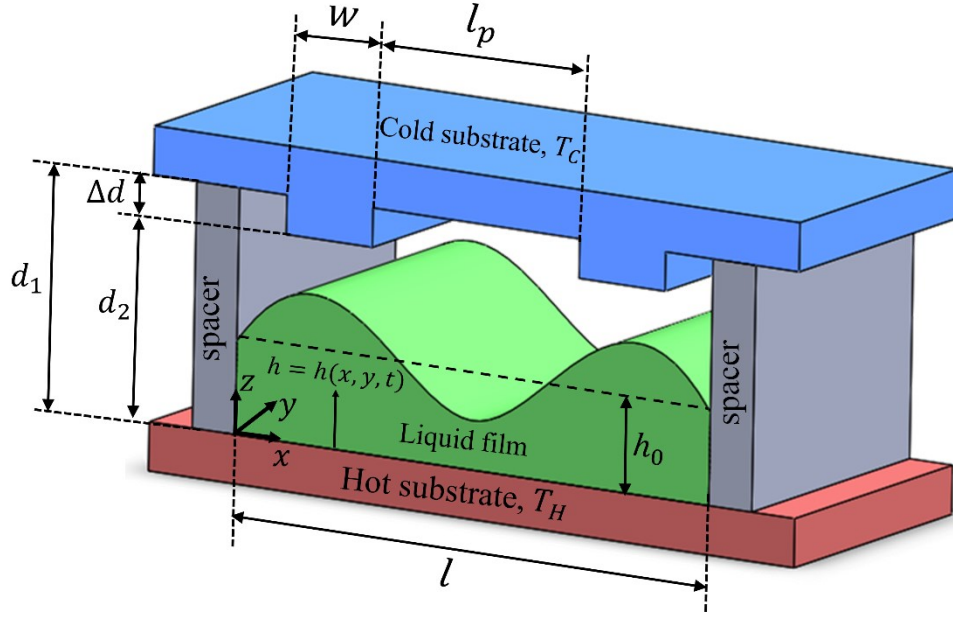


Figure 4.1. 3D schematic of the ultrathin liquid film placed between the top (cold) and bottom (hot) substrates, where $T_H > T_C > T_g$. Here, T_g is the glass transition temperature of the polymer film.

The protrusion width is w , and the spacing distance between the neighbor protrusions is l_p . Although the viscosity of the molten polymer changes at temperatures above T_g , it is assumed that the ultra-thin film behaves as a Newtonian and incompressible fluid with constant viscosity evaluated at the mean working temperature: $\mu = \mu\left(\frac{T_H + T_C}{2}\right)$. The variation in density due to temperature gradient within the film and during the interface deformation is included in our simulation using Boussinesq approximation. However, it should be noted that the effect of microgravity condition and density variation is negligible compared to viscous forces in nanofilms.

4.2.1. Governing Equations and Boundary Conditions (VOF model)

The numerical analysis considered in this study is based on solving the fluid motion governing equations and continuity equation using the VOF method. The details on the VOF model and the computational setup are provided in the following sections.

4.2.1.1. VOF model and computational procedure

This study numerically investigates the dynamics, instability, and morphological evolution of the air-liquid interface. The air-liquid system is considered a two-phase flow interface tracking

problem, and the governing equations for two-phase flow are solved using the VOF method. ANSYS-Fluent is used as our base-solver, which has been extensively used for similar studies and it is known to provide accurate and stable results [97,138]. The calculations are accomplished using the pressure-based segregated and implicit solver. Pressure-velocity coupling is performed using the pressure implicit with the splitting of the operator (PISO), considering two corrections to account for neighbor and skewness. The momentum and energy equations are discretized using a second-order upwind differencing scheme, while the pressure staggering option (PRESTO) is used for pressure interpolation. The implicit scheme with the courant number of 0.2 and time steps of 10^{-6} is used to obtain convergence. No gravitational force is imposed on the simulation, and all cases are run in double-precision mode. A wall adhesion angle in conjunction with the surface tension approach, which was presented by Brackbill [140], was used to model a three-phase line at the wall. Instead of applying boundary condition at the wall itself, the contact angle that polymer is possibly made with the wall is used to adjust the surface normal in cells near the wall. This so-called dynamic boundary condition leads to the adjustment of the curvature of the surface near the wall. The VOF method is used to track the polymer-air interface utilizing a geometric reconstruction scheme based on the piecewise linear interface calculation (PLIC) method [141]. Moreover, the Geo-reconstruction module is added to the existing VOF scheme to enhance the prediction accuracy of the polymer interface [142,143]. In the VOF model, a so-called fraction function of α is defined as the integral of fluid's characteristic function on an Eulerian fixed grid cell, which is unity at any point occupied by the fluid and zero elsewhere. The cells with $0 < \alpha < 1$ state the partially filled case that indicate the interface [144,145]. For a gas-liquid two phase flow system, the volume fraction of gas and liquid phases are α_g and α_l , respectively, and must satisfy conservation of mass (with respect to the phase concentration) in each computational cell:

$$\alpha_g + \alpha_l = 1$$

In general, the VOF method is applied to track interface movement between the immiscible liquid/gas and the liquid/liquid phases. A single momentum equation is solved throughout the domain to obtain a velocity field that is shared among the phases:

$$\rho \left[\frac{\partial \mathbf{u}}{\partial t} + (\mathbf{u} \cdot \nabla) \mathbf{u} \right] = \nabla \cdot [-p\mathbf{I} + \mu(\nabla \mathbf{u} + (\nabla \mathbf{u})^T)] + \mathbf{F}_V \quad (4.1)$$

where p is the pressure, ρ and μ is the volume-averaged density and viscosity computed for each cell,

$$\rho = \alpha_l \rho_l + (1 - \alpha_l) \rho_g \quad (4.2)$$

$$\mu = \alpha_l \mu_l + (1 - \alpha_l) \mu_g \quad (4.3)$$

and \mathbf{u} is treated as the mass-averaged variable, depending on the volume fraction of each phase α_l and α_g , and their material properties,

$$\mathbf{u} = \frac{\alpha_l \rho_l \mathbf{u}_l + \alpha_g \rho_g \mathbf{u}_g}{\rho} \quad (4.4)$$

The term \mathbf{F}_V in Eq. (4.1) is the volumetric force at the air-polymer interface, resulting from surface tension force. The volumetric surface tension force at cells containing both phases is evaluated using the continuum surface force (CFS) model [140]:

$$\mathbf{F}_V = \sigma \frac{\rho}{\frac{1}{2}(\rho_l + \rho_g)} k \mathbf{n} \quad (4.5)$$

where σ is the coefficient of surface tension, \mathbf{n} is the normal vector, which is calculated from the gradient of volume fraction, and k is the local surface curvature,

$$k = -(\nabla \mathbf{n}) = \frac{1}{\mathbf{n}} \left[\frac{\mathbf{n}}{|\mathbf{n}|} \nabla |\mathbf{n}| - (\nabla \cdot \mathbf{n}) \right] \quad (4.6)$$

Eq. 4.5 is added to the governing equations as a user-defined function (UDF). The surface tension varies by non-uniform temperature distribution at the gas-liquid interface, which leads to TC induced motion [59,60,137]. Here, the focus is on the TC-induced instabilities, in which we only consider the variations in σ due to inhomogeneity in temperature distribution. We also considered a linear dependence of σ on the temperature $T(x, z, t)$ [84,137],

$$\sigma = \sigma_0 - \sigma_T (T - T_0) \quad (4.7)$$

where σ_T is the temperature derivative of the surface tension, σ_0 is the surface tension evaluated at reference temperature T_0 and T is the liquid film temperature evaluated at the interface

$T(x, z, t)|_{z=h}$. The tracking of the air-film interface is accomplished by the solution of a volume fraction continuity equation for only one phase (the gas phase here):

$$\frac{\partial}{\partial t}(\alpha\rho_g) + \nabla \cdot (\alpha\rho_1\mathbf{u}_g) = 0 \quad (4.8)$$

In order to capture the TC effect, the temperature field is computed within the domain using the energy balance equation. The energy equation that is shared among the phases is given by:

$$\frac{\partial}{\partial t}(\rho E) + \nabla \cdot [\mathbf{u}(\rho E) + p] = \nabla \cdot (k\nabla T) \quad (4.9)$$

Here, E is the energy and can be computed as follows:

$$E = H - \frac{p}{\rho} + \frac{v^2}{2} \quad (4.10)$$

where H is enthalpy. H can be calculated for incompressible flows as

$$H = \sum_j Y_j H_j + \frac{p}{\rho} \quad (4.11)$$

Here, Y_j is the mass fraction of species j and

$$H_j = \int_{T_0}^T c_{p,j} dT \quad (4.12)$$

where $T_0 = 298.15$ K. The VOF treats energy (E) and temperature (T) as mass-averaged variables using the following definition:

$$E = \frac{\sum_{q=1}^n \alpha_q \rho_q E_q}{\sum_{q=1}^n \alpha_q \rho_q} \quad (4.13)$$

The corresponding version of Eq. (4.13) is written for each phase based on the shared energy/temperature and the specific heat of that phase. The thermal conductivity is also shared by the phases similar to the density and viscosity defined in Eqs (4.2) and (4.3).

4.2.1.2. Boundary conditions

A two-dimensional computational model is used to solve the governing equations (Eqs. 4.1, 4.8, and 4.9) based on the finite volume method (FVM). The three-dimensional variations (gradients) along the span of the domain are expected to be minimal, and the system is expected to behave

two-dimensional for the scales considered here [107,137]. The simulation domain in the Cartesian coordinate system is shown in Fig. 4.2, which consists of 2 subdomains (one for each phase), 15 boundaries, and 14 vertices. The Domain-1 and Domain-2 are initialized by the air and polymer film, respectively. The red and blue lines represent the applied hot and cold constant temperatures. The no-slip boundary condition is also applied to the top and bottom plates. It is necessary to have the periodic boundary conditions at edges 3, 4, 14, and 15. It is assumed that the liquid film, shown with the purple line at Boundary 2, is initially flat. The boundary conditions are summarized in Table 4.1. A non-homogenous grid is generated with a higher grid density near the walls (ratio of 1.1) to improve the tracking accuracy of the simulations close to the solid walls. This leads to a higher resolution for the dynamics and morphological evolution of the interface as the polymer touches the top plate or the bottom plate's dewetting.

Table 4.2 shows the range of geometrical parameters and the material properties used in the TC simulation. The value was adopted from the experimental studies on the thermal-induced patterning in the literature [19,112].

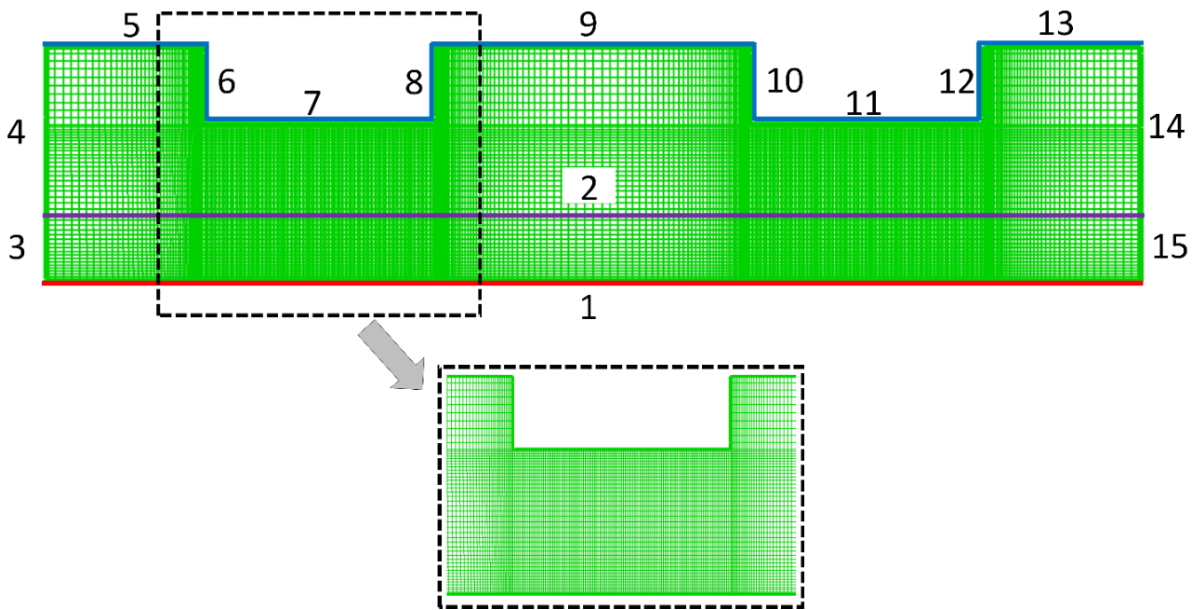


Figure 4.2. Schematic diagram introducing the boundary condition and mesh of the 2D model (not to scale).

Table 4.1. List of boundary conditions considered in the simulations.

Boundary number	Momentum	Energy
1	No-slip	T_H
3, 4, 14 and 15	Periodic	Periodic
5-13	No-slip	T_C

Table 4.2. Parameters and constants used in the TC simulation

Parameters	Value	Unit
Density of air (ρ_a)	0.829	kg/m ³
Viscosity of air (μ_a)	1.81×10^{-5}	Pa.s
Thermal conductivity of air (k_a)	0.0225	W/m K
Density of polymer (ρ_p)	1000	kg/m ³
Viscosity of polymer (μ_p)	30	Pa.s
Thermal conductivity of polymer (k_p)	0.13	W/m K
Surface tension of polymer (σ)	45×10^{-3}	N/m
Interfacial tension gradient (σ_T)	10^{-4}	N/m K
Temperature difference (ΔT)	100	K
Thermal conductivity ratio ($k_r = k_p/k_a$)	5.2	---

4.2.2. Scaling parameters and thin-film evolution

The parameters, including vertical and lateral coordinates, velocity field, temperature, and time are normalized as follows:

$$\begin{aligned} \tilde{h} &= \frac{h}{h_0}, \quad \tilde{d}_1 = \frac{d_1}{h_0}, \quad \tilde{d}_2 = \frac{d_2}{h_0}, \quad \tilde{z} = \frac{z}{h_0} \\ \tilde{x} &= \frac{x}{\lambda_c}, \quad \tilde{w} = \frac{w}{\lambda_c}, \quad \tilde{l}_p = \frac{l_p}{\lambda_c} \\ \tilde{u}_x &= \frac{u_x}{u_c}, \quad \tilde{u}_z = \frac{\lambda_c u_z}{h_0 u_c}, \quad \tilde{p} = \left(\frac{\lambda_c}{\mu u_c} \right) p \\ \tilde{t} &= \left(\frac{u_c}{\lambda_c} \right) t, \quad \tilde{T} = \frac{T - T_C}{\Delta T}, \quad \tilde{\sigma} = \frac{\sigma}{\mu u_c} \end{aligned}$$

(4.14)

The initial film thickness (h_0) is used to nondimensional the vertical dimensions of z , d_1 , and d_2 , whereas the characteristic wavelength (λ_c) is used to normalize the lateral dimensions of x , l_p and w . Terms \tilde{w} , \tilde{l}_p , \tilde{t} , \tilde{x} , \tilde{z} , \tilde{T} and \tilde{h} denote the scaled parameters of the width of the protrusions, the distance between the protrusions, time, length, height, temperature, and interface height, respectively. The velocity and pressure field also scaled using the TC induced characteristic velocity u_c defined as $u_c = \frac{\sigma_T k_r d_2 \Delta T}{\mu[(1-k_r)+k_r \tilde{d}_2]^2}$ [19,84]. The nondimensional term of \tilde{d}_2 is referred to as the inverse filling ratio and k_r is the ratio of the thermal conductivity of the polymer film to the air layer. Applying the above-mentioned scaling factors to the governing equations results in the following dimensionless ratios for Marangoni, Capillary, and Prandtl numbers:

$$Ma = \frac{\sigma_T \Delta T}{\mu u_c}, \quad Ca = \left[\frac{\sigma}{\mu u_c} \right]^{-1}, \quad Pr = \frac{c_p \mu}{k} \quad (4.15)$$

The governing equations (continuity, momentum, and energy equations) and boundary conditions (no slip at the top and bottom substrate, kinematic and stress balance at the interface) are normalized [19,84]. To find the characteristic wavelength relation, the shorter distance between two substrates (\tilde{d}_2) is used (see section S1 in the supplementary material). The normalized equations are then simplified using long-wavelength approximation ($h_0/\lambda_c \ll 1$) leading to the following dimensional TF equation, which shows the spatiotemporal evolution of a thin liquid film subjected to the transverse thermal gradient (derivations are available in the supplementary material S2.)

$$\frac{\partial \tilde{h}}{\partial \tilde{t}} + \nabla \cdot \left\{ \frac{\tilde{h}^3}{3} Ca^{-1} \nabla (\nabla^2 \tilde{h}) + \frac{\tilde{h}^2}{2} \frac{Ma k_r \tilde{d}_2}{[(1-k_r)\tilde{h} + k_r \tilde{d}_2]^2} \nabla \tilde{h} \right\} = 0 \quad (4.16)$$

To derive insight into the thin film's instabilities and dynamics, we solve the nonlinear TF equation that is a 4th order nonlinear partial differential equation (PDE). Using the finite difference (FD) discretization and applying a 2nd order central finite difference scheme for spatial derivatives and a differential-algebraic system solver of DASSL with adaptive time step solver settings. More details about this numerical scheme are available in our previous studies [20,62,84].

4.2.2.1. Linear stability analysis

Linear stability (LS) analysis is the conventional technique in predicting the characteristic wavelength for the growth of instabilities, λ_c . The corresponding wavelength is calculated by replacing the uniform interface height (h) in the so-called thin-film equation with a periodic perturbation of $\tilde{h} = 1 + \xi \exp(\bar{\kappa} \tilde{x} i + S(\bar{\kappa}) \tilde{t})$, where $i = \sqrt{-1}$, $\bar{\kappa}$ is the wavenumber, $S(\bar{\kappa})$ is the growth coefficient, and $\xi (\ll 1)$ is the infinitesimal amplitude coefficient. Details for the derivations of the dispersion relation and the characteristic wavelength is available in the supplementary material for the LS analysis section (S3). The following equation shows the characteristic wavelength obtained by LS analysis:

$$\lambda_{LS} = 2\pi [h_0(1 - k_r) + k_r d_2] \sqrt{\frac{4\sigma h_0}{3d_2 \sigma_T k_r \Delta T}} \quad (4.17)$$

The characteristic wavelength obtained from LS analysis (λ_{LS}) will be used as a lateral normalizing factor. To show the dependencies of the characteristic wavelength to the distance between substrates, film thickness, and temperature gradient, the following equations can be derived based on Eq (4.17):

$$\lambda_{LS} = 2\pi h_0(1 - k_r) \sqrt{\frac{4\sigma h_0}{3\sigma_T k_r \Delta T}} d_2^{-\frac{1}{2}} + 2\pi k_r \sqrt{\frac{4\sigma h_0}{3\sigma_T k_r \Delta T}} d_2^{\frac{1}{2}} \quad (4.18)$$

$$\lambda_{LS} = 2\pi (1 - k_r) \sqrt{\frac{4\sigma}{3d_2 \sigma_T k_r \Delta T}} h_0^{\frac{3}{2}} + 2\pi k_r \sqrt{\frac{4\sigma}{3d_2 \sigma_T k_r \Delta T}} h_0^{\frac{1}{2}} \quad (4.19)$$

$$\lambda_{LS} = 2\pi [h_0(1 - k_r) + k_r d_2] \sqrt{\frac{4\sigma h_0}{3d_2 \sigma_T k_r}} \Delta T^{\frac{1}{2}} \quad (4.20)$$

4.3. VOF Verification

Different spatial grid element sizes are examined to find the optimum grid size that accurately predicts the interface deformation. In this effort, the case is considered for the following conditions: $d_1 = 200$ nm, $d_2 = 150$ nm, $w = 600$ nm, $l_p = 4000$ nm and $\Delta T = 100$ K. Four cases (Grid 1, Grid 2, Grid 3, and Grid 4) are generated to verify the effect of the spatial grid on the results. Here, the number of elements is increased systematically from Grid 1 (12,000) to Grid 4 (24,000), while maintaining the same grid distribution and quality. The exact location of the interface for each mesh is compared between consecutive cases (e.g., Grid 4 with Grid 3 and Grid

3 with Grid 2), and the results are presented in Table 4.3. The error in Table 4.3 was calculated as:

$$error (\%) = \frac{1}{n} \sum_{i=1}^n \frac{h_{new,i} - h_{old,i}}{h_{old,i}} \times 100 \quad (4.21)$$

where n is the number of extracted data points for interface location. This variation between the grids falls below 5% for Grid 3, which indicates that it is sufficient to accurately track and predict the interface deformation for the geometry with the biggest size and most complex features in the present study.

Table 4.3. The effect of grid size on transient growth of interface height

Case:	Grid 1	Grid 2	Grid 3	Grid 4
Number of cells:	12000	15000	18000	24000
Error (%):	-	5.3	1.5	1.1

4.4. Results and Discussion

The air bounding layer has a lower thermal conductivity than the liquid film. Therefore, the protrusion areas, which have a smaller air gap, are exposed to the higher temperature gradient and vice versa. The induced non-uniform temperature gradient results in a gradient of surface tension at the interface. The generated tangential stress transfer to the lower layers of fluid by viscosity triggers the fluid flow and subsequently leads to the film's morphological evolution. Using a top plate with protrusions generates a temperature gradient along the polymer-air interface and adds more control to the pattern formation, resulting in well-ordered pillar arrays. The details of this observation will be discussed in later sections.

4.4.1. Non-uniform Temperature Gradient and Morphological Evolutions

Many studies have explored the formation of hexagonal or random pillar arrays using a flat plate as a top substrate [17,84]. Here, we used a patterned cold plate to reduce the coarsening effect and generate well-ordered pillars. The temperature gradient at the interfaces and the resultant interfacial tension gradient is responsible for the TC-induced instabilities and pattern formation on the film.

The pattern formation steps and the film's temperature distribution are presented over the evolution time in Fig. 4.3(a-d). The deformation of the interface is divided into three stages. At the early stage of deformation, the air gap is large, and the temperature gradient and the resulting TC force at the interface are small, leading to a slow amplification of interface deformation. In the second stage, the interface has already deformed, and the air gap is smaller, which generates a higher thermal gradient at the interface. This leads at this stage to a faster deformation of the interface. The pattern evolution process continues until the liquid film touches the top plate in the last stage ($\tilde{t} = 403$). The wetting mechanism of the top plate and dewetting of the bottom plate by the polymer film depends on the intermolecular interactions between the polymer material and the plates, as well as the ratio of the initial film thickness to the plate separation distances [35,59]. These factors affect the transition in the shape of created pillars from cone to columnar and finally to the inverted cone-shaped structures. Tracking the interface height over time (shown in image 3d) elucidates a non-linear increase in the rate of interface deformation as the interface moves toward the top plate. In this study, the contact angle that shows the tendency of the polymer film in the wetting of the plates is constant and set to $\pi/2$ for all cases.

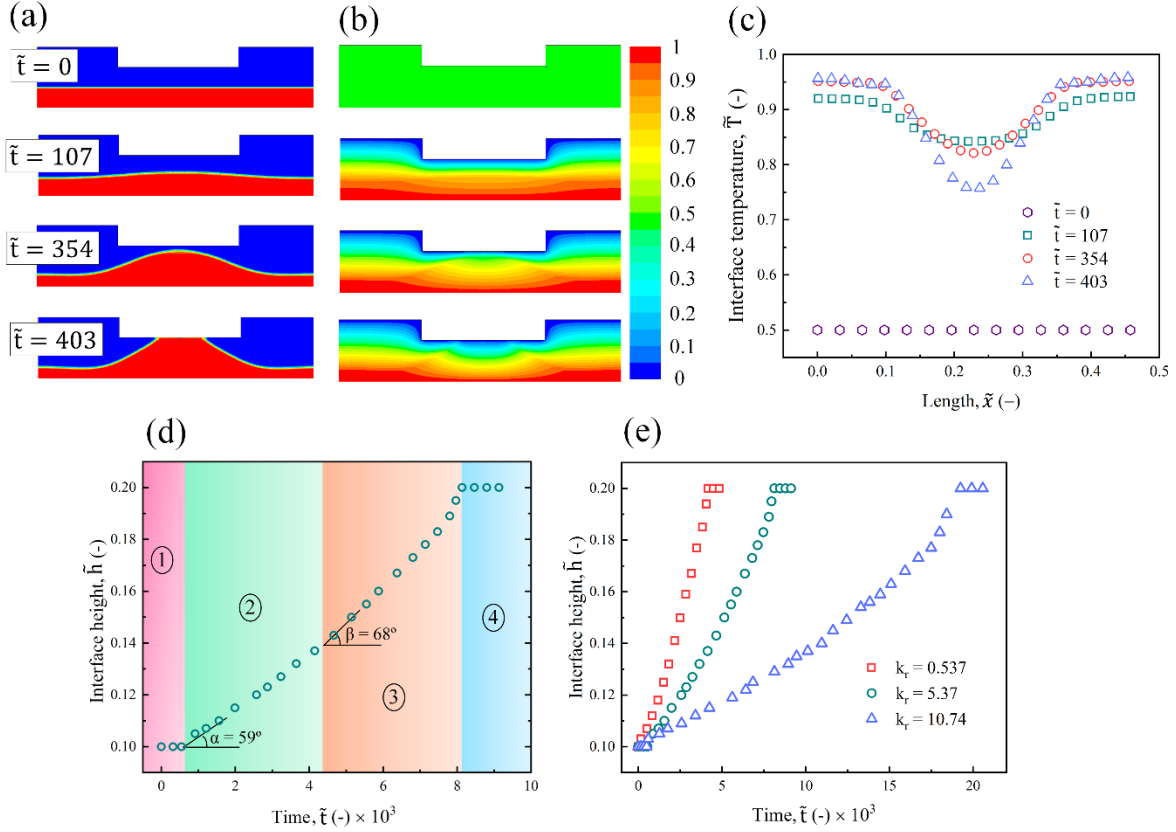


Figure 4.3. Thermally-induced hierarchical structures for a patterned template, $\tilde{d}_1 = 3, \tilde{d}_2 = 2, \tilde{w} = 0.2, \tilde{l}_p = 0.26, \tilde{T} = 1$, and $\lambda_{LS} = 3.06 \mu m$. (a) 2D snapshots of the film interface at different stages of the evolution process. (b) Snapshots of the temperature distribution through the channel. (c) The temperature at the interface over time. (d) The tracking of the interface height of a pillar. (e) The effect of different thermal conductivity over time conductivity.

The temperature distribution within the film and along the interface, including the interface evolution over time, is presented in Fig. 4.3(b). At the initial condition ($\tilde{t} = 0$), the temperature in the film and the bounding layer is set to $\tilde{T}=0.5$, which is the average temperature of the top and bottom surfaces. The temperature profile along the interface shows that the temperature gradient on the interface increases as the film deforms and eventually reaches the top plate (Fig.4.3(c)). Thermal conductivity ratios of the film and the bounding layer (k_r) impacts the rate of interface deformation, and thus more significantly alters the pillar growth rate (shown in image 4.3e). The temperature distribution at the interface becomes uniform when the thermal conductivity of the polymer is higher. Therefore, TC force becomes smaller, leading to the slower deformation of the interface. A similar case is numerically simulated using the TF equation, and the results are

presented in Fig.4.4. The snapshots of the interface height at different stages show a single pillar formation under the protrusion with the exponential growth rate in time.

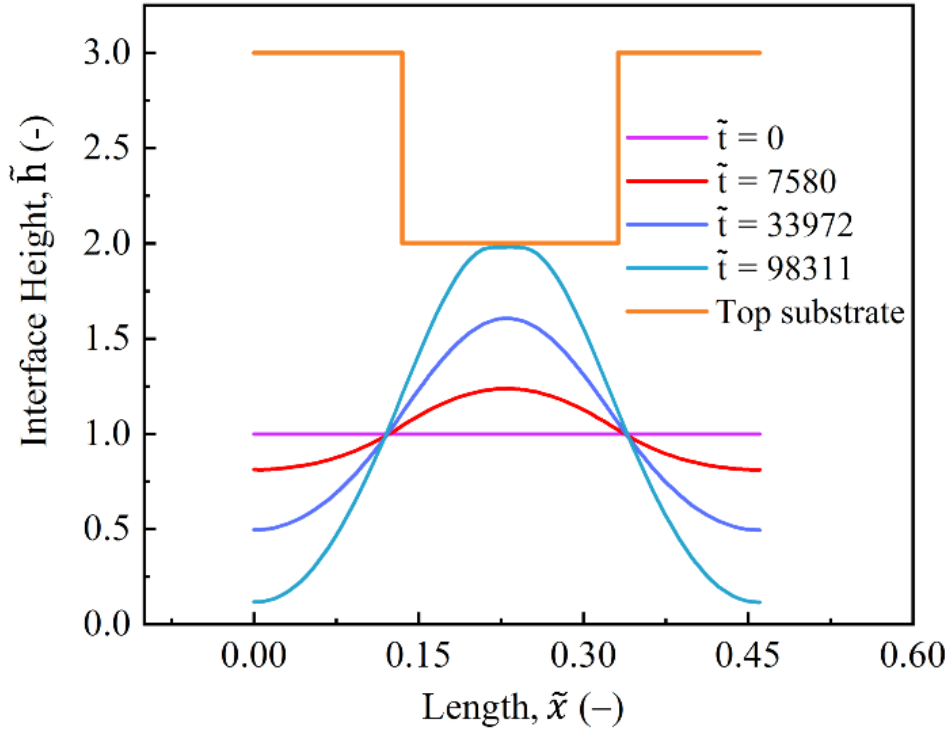


Figure 4.4. 2D snapshots of the thin film interface, $\tilde{d}_1 = 3, \tilde{d}_2 = 2, \tilde{w} = 0.2, \tilde{l}_p = 0.27, \tilde{T} = 1$, and $\lambda_{LS} = 3.06 \mu m$.

4.4.2. Characteristic wavelength Predictions: VOF vs. LS analysis

The characteristic length for the growth of instabilities in the TC-induced patterning process is predicted using the LS analysis, which relies on the small deformation from the original state (base case). Experimental observations and monitoring of the interface deformation at its early stages showed that the LS predicted wavelength (λ_{LS}) matches well with the experimental results [18,19,51,112]. However, the interface deformation undergoes non-linear deformations soon after the initial undulation. This leads to uncertainties in the validity of λ_{LS} to predict the final form of the structures. Here, we used a numerical simulation to predict the TC induced interface deformation at both early linear and late non-linear stages of the pattern formation process. In this

section, the relationship between the VOF-predicted characteristic length scale and the one obtained using LS analysis is predicted.

4.4.2.1. Validation

The simulation results are first compared with the experiments of Dietzel and Troian[19] to verify their accuracy. In the VOF model predictions, the characteristic wavelength (λ_c) is found after pattern formation via measuring the center to center distance of neighboring pillars. For the case considered by Dietzel and Troian[19] ($d_1 = 310$ nm, $d_2 = 210$ nm, $w = 6$ μ m, $l_p = 500$ nm, $h_0 = 100$ nm, and $\Delta T = 46$ K), our VOF-predicted characteristic wavelength is 1.82 μ m, which is in good agreement ($\sim 10\%$ error) with their experimental value of 2.04 μ m. However, the value of λ_c obtained from the LS analysis (using Eq. (4.17)) is 4.52 μ m, which expectedly deviates significantly ($\sim 121\%$ error) from the experimental observation. In addition, the characteristic wavelength obtained from TF is 4.2 μ m, which is a better prediction compared to LS analysis but far from the value obtained from experimental data and VOF model. Table 4.4 presents the characteristic wavelength obtained from VOF, TC, and TF. The VOF simulation showed the lowest deviation from experimental observation compared to the TF and LS predictions. Given the simplicity of LS theoretical analysis compared to other two numerical predictions, it is of interest to find a correlation between the LS predicted characteristic wavelength and the more accurate VOF model results.

Table 4.4. The characteristic wavelength in the different approaches

	Exp [19]	VOF	TF	LS
λ_{max} (μ m)	2.04	1.82	4.2	4.52
Deviation From Exp.(%)	-	-10	+105	+121

4.4.2.2. Developing VOF model for thermocapillary thin-film flow

To find a relationship between the characteristics wavelength predicted by the VOF model (λ_{VOF}) and the LS analysis (λ_{LS}), thirteen cases are simulated based on different initial film thickness (h_0),

separation distances between the plates (d_1 and d_2), and temperature gradient (ΔT). The values of λ_{VOF} and λ_{LS} are then compared in Table 4.5.

Table 4.5. The different parameters used for finding a relation between the VOF and the LS analysis ($w = 6 \mu m$ and $l_p = 7 \mu m$)

Case number	d_1 (nm)	d_2 (nm)	ΔT (K)	h_0 (nm)	λ_{LS} (μm)	λ_{VOF} (μm)
1	300	200	100	100	3.86	1.32
2	300	200	90	100	4.06	1.38
3	300	200	80	100	4.31	1.46
4	300	200	70	100	4.61	1.51
5	300	200	60	100	4.98	1.54
6	300	200	55	100	5.2	1.58
7	300	200	50	100	4.45	1.62
8	310	210	46	100	4.82	1.82
9	300	200	100	110	3.84	1.30
10	300	200	100	90	3.84	1.31
11	300	200	100	80	3.8	1.28
12	275	175	100	100	3.44	1.12
13	350	250	100	100	4.6	1.49

The VOF-predicted characteristic wavelengths in Table 4.5 are obtained by measuring the average center to center distances of pillars formed at the quasi-steady stage of pattern formation. The width of the protrusion is $6 \mu m$ ($w = 6 \mu m$) and the distance between two protrusions is $7 \mu m$ ($l_p = 7 \mu m$). Fig. 4.5 shows a snapshot of the film spatio-temporal evolution for Case 1 in Table 4.5, showing different pattern formation stages. The interface deformation started under the edge of protrusion, where the interfacial tension (and temperature) has the highest gradient. Subsequently, the generated surface waves traveled toward the center. The initial undulations on the interface have led to the formation of the first set of pillars near the edges with the concurrent fluid depletion around these pillars (Figures 4.5a(ii) and 4.5a(iii)). The remnant fluid layer between the two pillars experienced the TC force due to its uneven surface, which resulted in the formation

of second sets of pillars at $t > 119$ ms (Figures 4.5a(iv) and 4.5a(v)). The pillar formation process continued until the remained polymer was sufficient to form one pillar (Fig. 4.5a(vi)). After the pattern formation is completed, when all pillars touched the upper mask as shown in Fig. 4.5a(vi), the characteristic wavelength is measured by averaging the center of the created pillars.

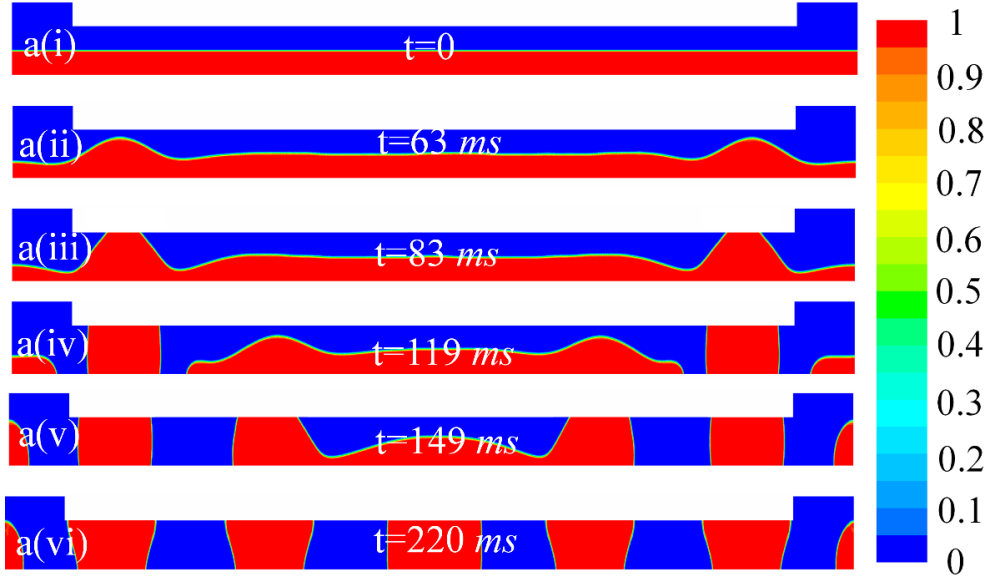


Figure 4.5. Thermally-induced hierarchical structures for a patterned template. 2D snapshots of the film interface, $h_0 = 100$ nm, $d_1 = 300$ nm, $d_2 = 200$ nm, $w = 6$ μ m, $l_p = 500$ nm and $\Delta T = 100$ K at different stages of the evolution process, a(i) initial, a(ii) 63 ms, a(iii) 83 ms, a(iv) 119 ms, a(v) 149 ms and a(vi) 220 ms.

The measured λ_{VOF} is plotted against the LS-predicted wavelength (λ_{LS}) in Fig. 4.6. The relationship between λ_{VOF} and λ_{LS} is determined using an implicit radical function dependence,

$$\lambda_{VOF} = c_1 \sqrt{\lambda_{LS}} + c_2 (\lambda_{LS})^{3/2} + \frac{c_3}{\sqrt{\lambda_{LS}}}, \quad (4.22)$$

where $c_1 = 1.5034$, $c_2 = -0.0728$, and $c_3 = -1.5959$ are fitting coefficients.

4.4.2.3. The effect of Marangoni and Capillary inverse numbers on the VOF-TC model

Fig. 4.7a shows the variation of the characteristic wavelength predicted by the VOF model (red symbols), TF model (blue symbols), and LS analysis (blue line). Fig. 4.7b shows the Marangoni number (Ma) and the Capillary inverse (Ca^{-1}) with inverse filling ratio ($\tilde{d}_2 = d_2/h_0$). Marangoni number (Ma) represents the relative strength of the TC force to the viscous force, while the

Capillary inverse (Ca^{-1}) represents the relative strength of the surface tension force acting on the interface to the viscous force. At a constant plate separation distances (d_1 and d_2), the initial film thickness increased to study the effect of different filling ratios on the final structure of the pillars. As can be observed in Fig. 4.7b, the Marangoni number decreased by increasing the filling ratio. An explanation is that increasing the filling ratio (thicker film) leads to a lower temperature gradient at the interface, decreasing the TC force and Marangoni number. Similarly, the Ca^{-1} decreases as the filling ratio increases.

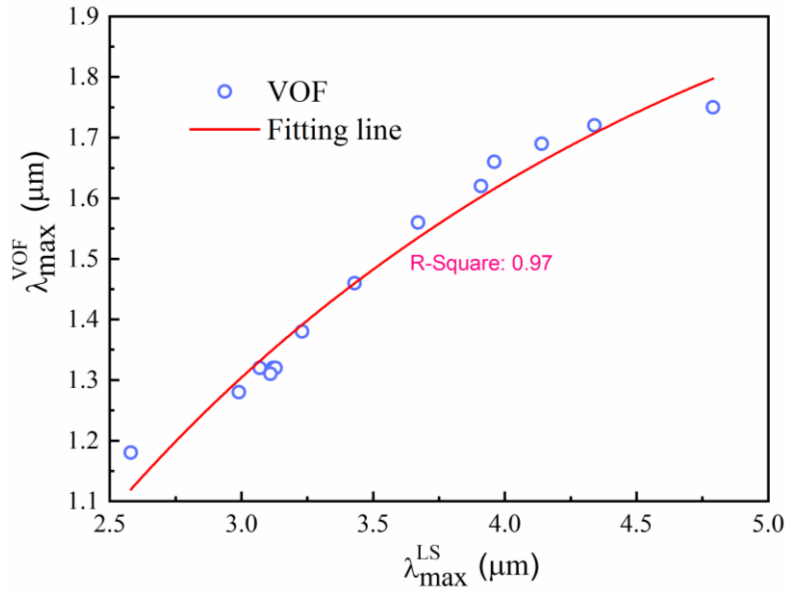


Figure 4.6. The relation for dominant instability wavelength, λ_c for both VOF simulation and LS analysis.

The characteristic wavelength predicted by the LS analysis (λ_{LS}) increased sharply for small \tilde{d}_2 up to a maximum at $\tilde{d}_2 = 2.44$. To calculate the maximum point, the derivative of λ_{LS} with respect to h_0 is set to zero ($d\lambda/dh_0 = 0$) in Eq. (4.17). Thus, a relation is obtained for \tilde{d}_2 as a function of k_r : $\tilde{d}_2 = 3(1 - k_r)/(-k_r)$. Since k_r is a material property, the extremum value for \tilde{d}_2 can be adjusted based on the geometrical limitations with respect to the thermal properties of the film. In the current study, where the ratio of the thermal conductivity of polymer to that of air is $k_r = 5.37$, \tilde{d}_2 is calculated as 2.44. The red and blue symbols in Fig. 4.7a show the variations in characteristic wavelength predicted by the VOF model and TF model, respectively. The λ_{VOF} has a similar trend as λ_{LS} . It increased for small values of \tilde{d}_2 and dropped rapidly after it reached a maximum point

at $\tilde{d}_2 = 2.5$. It must be noted that although λ_{VOF} followed a similar parabolic trend as λ_{LS} , its magnitude is about three times smaller than λ_{LS} . On the other hand, λ_{TF} has a similar trend as λ_{VOF} ; however, it reached a maximum point at $\tilde{d}_2 = 2.44$ (like LS). The magnitude of λ_{TF} is less than λ_{LS} and higher than λ_{VOF} .

Next, the effect of the temperature gradient (ΔT in the range of 50 K to 100 K) on the capillary inverse (Ca^{-1}) and the characteristic wavelength predicted by VOF, TF, and LS analysis is investigated, and results are presented in Fig. 4.8. The Ca^{-1} decreased with an increase in the nondimensional temperature as it is inversely related to ΔT . As the temperature difference along the film interface increases, the resulting TC force applied to the interface increases, leading to a higher characteristic velocity within the film. The higher u_c (and shear rate) results in higher viscous resistance and thus lower Ca^{-1} .

All the characteristic wavelengths from LS analysis (blue line), TF model (blue symbols), and VOF simulation (red symbols) decreased with an increase in the applied thermal gradient (presented in Fig. 4.8a). From Eq. (4.17), λ_{LS} is proportional to the inverse of the square root of the temperature difference ($\lambda_{LS} \propto \Delta T^{-1/2}$). With an increase in the temperature difference from 0.5 to 1, the λ_{max} the reduction in characteristic wavelengths is about 27%, 33%, and 33% for VOF, TF, and LS methods, respectively. Given the large difference in Lambda's absolute values between these approaches, the predictions for the relative reductions are in a close match.

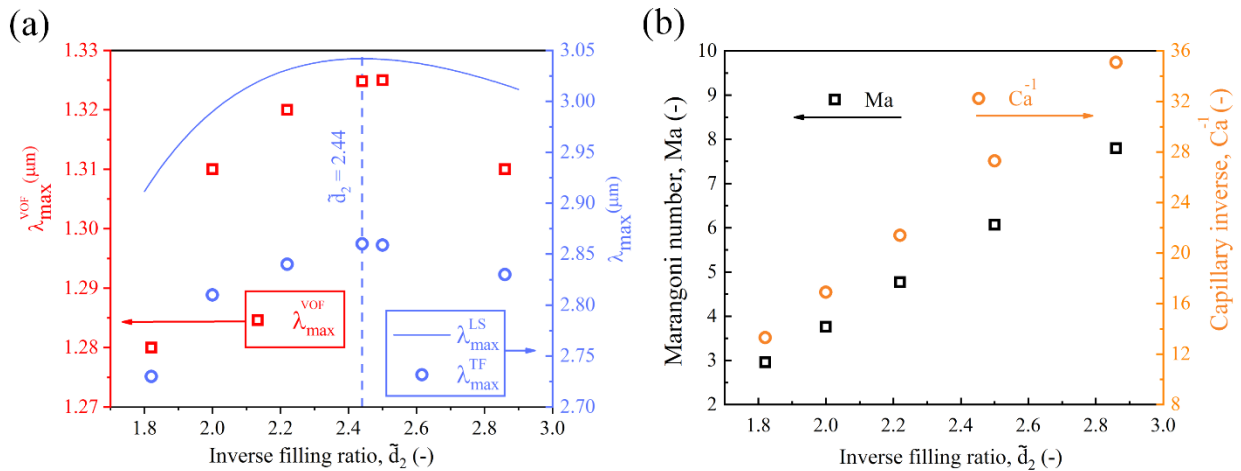


Figure 4.7. Marangoni and Capillary inverse numbers, the characteristic wavelength from LS and VOF at different film thicknesses.

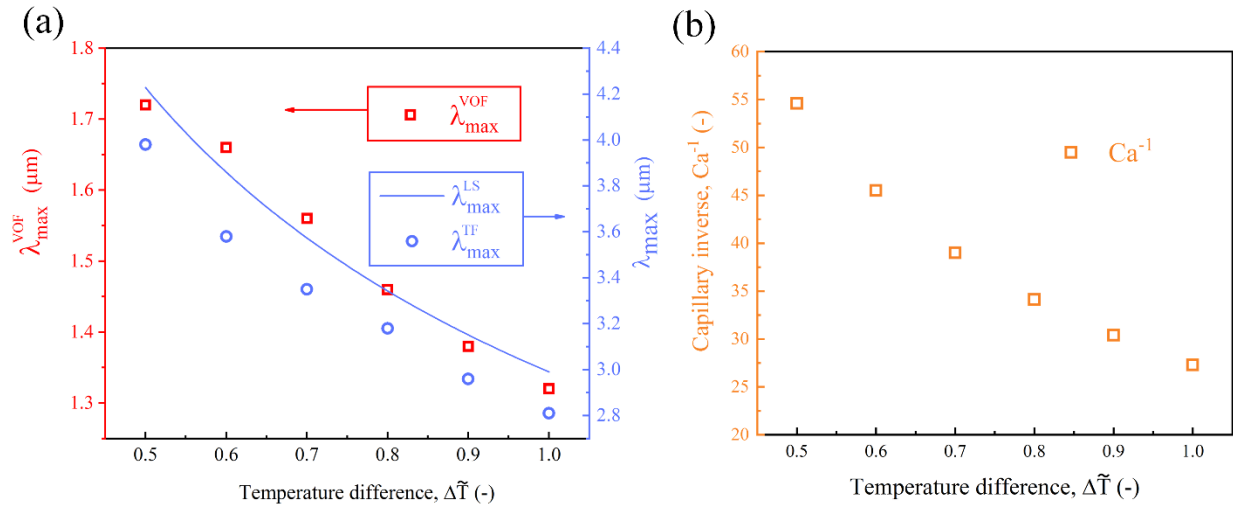


Figure 4.8. Capillary inverse, the characteristic wavelength from LS and VOF at different temperature gradients.

So far, the similarity and differences in predictions of the characteristic length using three methods of LS analysis, the TF model and the VOF model, have been discussed. In what follows, the effect of localized cooling using a patterned top plate on the pattern formation's fidelity will be compared using both VOF and TF nonlinear simulations.

4.4.3. Effect of Mask Geometry on the Pattern Formation

The size and periodicity of the protrusions need to be tailored to avoid secondary pillar formations when using plates with protrusions to generate the non-uniform thermal gradient and enable forming well-ordered patterns. Also, the shape, size, and the number of the formed pillars are affected by the geometry of the protrusions at the top cold substrate. Later in this section, we discuss these conditions and outline the range of the geometrical parameters predicted by VOF numerical simulations and the TF models. To simplify the comparison, λ_{LS} is used for the lateral normalizing scale.

4.4.3.1. The effect of protrusions width

The size and number of created pillars in TC-induced patterning are affected by the protrusions' width. The snapshot of the thin film evolution for the case of $\tilde{d}_1 = 3, \tilde{d}_2 = 2, \tilde{w} = 0.52, \tilde{l}_p = 0.26$ and $\tilde{T} = 1$ is shown in Fig.4.9. The polymer interface is assumed to be initially flat (Fig. 4.9a(i)). At $\tilde{t} = 5644$ in Fig. 4.9a(ii), two twin pillars formed under each protrusion. The separation distance between the formed pillars was long enough to prevent them from merging (Fig. 4.9a(iii)) until they touch the top plate at $\tilde{t} \geq 14940$ in Fig. 4.9a(iv). The interface deformation is strongly related to the interface temperature profile since it causes the non-uniformity in the interfacial tension. Figure 4.9(b) demonstrates the normalized temperature profile at the air-film interface over the deformation time. There exist two low-temperature regions close to $\tilde{x} \sim 0.4$ and $\tilde{x} \sim 1.5$ at initial stages of interface deformation ($\tilde{t} = 5644$). The surface tension at these regions is higher, pulling the polymer towards the neighboring areas with lower interfacial tensions. With the significant jump in the surface tension at the corners, the two twin pillars ascended at the initial stage of the pattern formation (Fig. 4.9 a(ii) and a(iii)). The temperature difference between the peak and trough at the interface increased as the pillar grew over time, which triggered the growth rate over time. This also prevented the merging of the neighboring pillars.

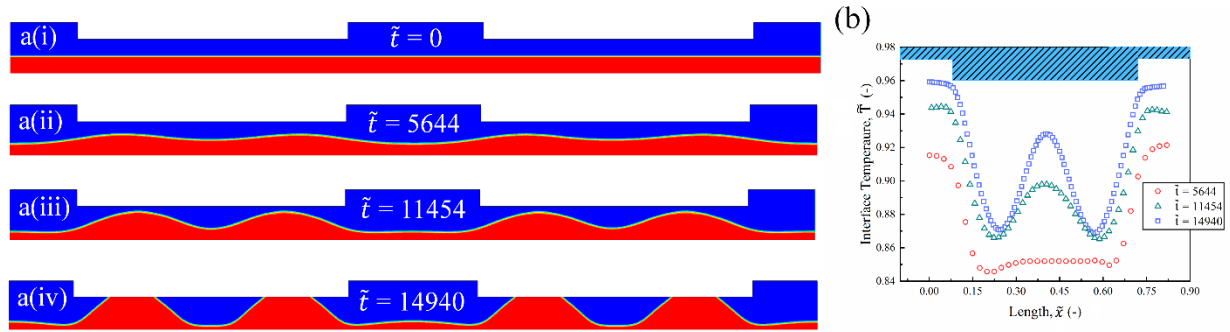


Figure 4.9. (a) 2D snapshots of the interface deformation and (b) normalized temperature profile at the interface when multiple pillars form under the protrusion, $\tilde{w} = 0.52$

Fig. 4.10 shows the snapshot of the thin film evolution predicted by the TF model for the case of $\tilde{d}_1 = 3, \tilde{d}_2 = 2, \tilde{w} = 1.47, \tilde{l}_p = 0.26$ and $\tilde{T} = 1$. The size and number of pillars in the TF model are similarly affected by the protrusions' width. However, the magnitude of \tilde{w} for making two twin pillars is found to be higher than that of in the VOF simulation.

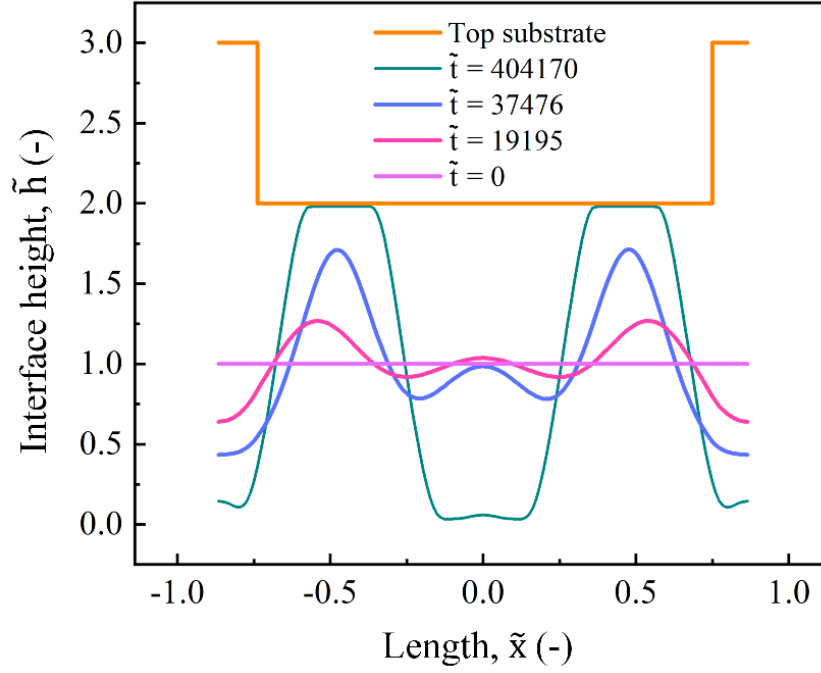


Figure 4.10. 2D snapshots of the interface deformation predicted by the TF model at $\tilde{w} = 1.47$.

An interesting observation in Figs. 4.9 and 4.10 is that by tuning the protrusion's width multiple pillars can be generated under each protrusion. This enhances the pattern miniaturization capability in TC patterning since the formed pillars' width is less than half of the protrusion width. Depending on the width of the top plate protrusions, the number of created pillars varies.

Fig. 4.11 shows the 2D snapshots of the interface over the evolution time for three different conditions. First, the case with $\tilde{w} < 0.34$ leads to the formation of only one pillar under the protrusion, as shown in Fig. 4.11a(i) – 4.11a(iii). This is followed by the transition stage, at which the protrusion width is $0.34 < \tilde{w} < 0.49$. Here, two peaks are observed at the early stages. As the film evolved, however, the initially formed peaks merged, and only one pillar was formed at the end (Fig. 4.11b(i) – 4.11b(iii)). For $\tilde{w} = 0.52$ in Fig. 4.11c(i) – 4.11c(iii), the initially formed peaks are well separated from one another, and they did not merge over time to form two isolated pillars under one protrusion. Hence, the width of protrusions can be increased to form more pillars (e.g., five pillars in Fig. 4.5) under a single protrusion. However, using very large protrusions leads to the formation of secondary and tertiary pillars, whose size and shape will no longer be under control. Moreover, it should be noted that the threshold value of $\tilde{w} = 0.52$ found here is for a

specific filling ratio of 2. This threshold varies by changing the filling ratio, which will be discussed later in this section.

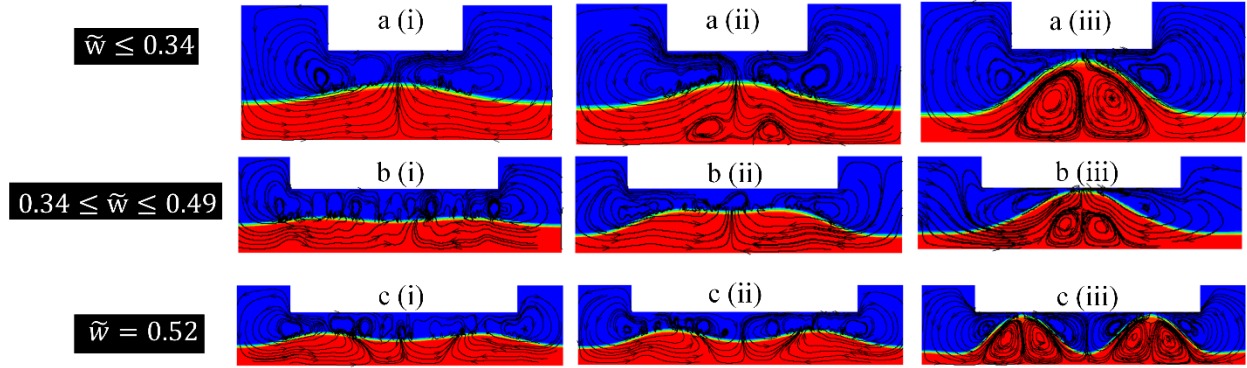


Figure 4.11. The different stages in the formation of the pillars by increasing the width of the protrusions where $\tilde{d}_1 = 3, \tilde{d}_2 = 2, \tilde{l}_p = 0.26$ and $\tilde{T} = 1$.

Figure 4.11 also highlights the streamlines for three different conditions. These conditions show that flow circulation takes place within both the polymer and the surrounding air. Viscous forces transfer the TC force at the interface to different fluid layers, which induces motion. The lateral flow of liquid at the surface takes place from the warmer regions to the cooler side under the protrusion, which forces the cooler liquid to descend. The downward movement of cooler liquid creates two convection cells, known as Bénard–convection cells, for each interface undulation. The formation of two recirculation regions for each pillar matches well with experimental and numerical data reported by Vanhook et al. [135].

A 2D map for both VOF and TF model is generated based on the normalized width of the protrusions (\tilde{w}) and the inverse filling ratios (\tilde{d}_2) to predict the threshold width value of \tilde{w}^* , in which the transition from single- to two-pillar formation occurred. The other parameters, such as temperature difference and thermal conductivities of the layers, are kept constant to generate this map. As shown in Fig. 4.12a, there is a linear relationship between the inverse filling ratio and the threshold width. As the inverse filling ratio increased, the threshold width increased as well. The equation of the dashed line in Fig. 4.12a is $\tilde{w}_{VOF} = 0.2\tilde{d}_{ave} - 0.08$, where \tilde{w} is the scaled width ($\tilde{w}_{VOF} = w/\lambda_{LS}$). The dimensional form of this equation ($w_{VOF} = 0.2\left(\frac{d_2}{h_0}\right)\lambda_{LS} - 0.08\lambda_{LS}$) can be

used to obtain the width of patterns as a preliminary choice for fabricating patterned masks. On the other hand, a similar equation for the TF model is obtained (Fig. 4.12b), which is $\tilde{w} = 0.32\tilde{d}_{ave} - 0.62$ and its dimensional form is $w_{VOF} = 0.32 \left(\frac{d_2}{h_0}\right) \lambda_{LS} - 0.62\lambda_{LS}$.

4.4.3.2. The effect of the distance between protrusions

The distance between two protrusions at the top mask is another geometrical property of the top plate that affects the fidelity of the pattern formation in TC-induced patterning. In all the cases discussed so far, no pillar formations are observed in the regions between each protrusion. Under certain conditions, secondary pillars can also form in the area between each protrusion. Here, we discuss the dynamics of interface evolution when the secondary pillars form. We will also look at the conditions required to avoid or mitigate the formation of such features.

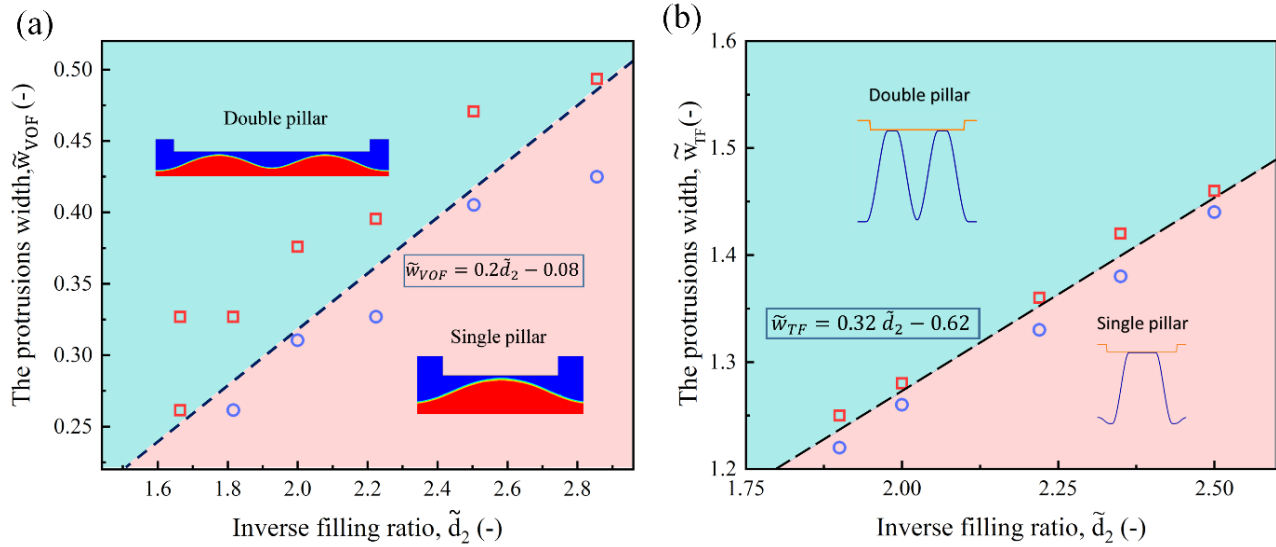


Figure 4.12. The threshold value for the width of the protrusions at different polymer thicknesses where $\tilde{l}_p = 0.26$ and $\Delta\tilde{T} = 1$, (a) VOF model (b) TF model.

The 2D time snapshots of the interface evolution for the case with $\tilde{d}_1 = 2, \tilde{d}_2 = 1.5, \tilde{w} = 0.31, (\tilde{l}_p)_{VOF} = 0.82$ and $\tilde{T} = 1$ shows the formation of the secondary pillar in the gap between two neighboring protrusions, as shown in Fig. 4.13. Like the previous cases, the thin film is initially flat (Fig. 4.13a(i)). The non-uniform temperature distribution along the interface destabilizes the liquid film under the protrusions (Fig.4.13a(ii)). This leads to the formation of primary pillars beneath each protrusion at later stages (Fig. 4.13a(iii)). Once the primary pillars are formed, the residual polymer between these pillars, which no longer has a flat interface, moves toward the top plate due to the heterogeneous distribution of the interfacial tension (Fig. 4.13a(iv)). The thinning of the film between two crests continues until the interface touches the top plate, and the secondary pillar is formed (Fig. 4.13a(v)). The thickness of the remnant polymer after the formation of primary pillars, the magnitude of temperature gradient in those regions, and the wetting properties of both top and bottom plates affect the dynamics and the evolution of the secondary pillars.

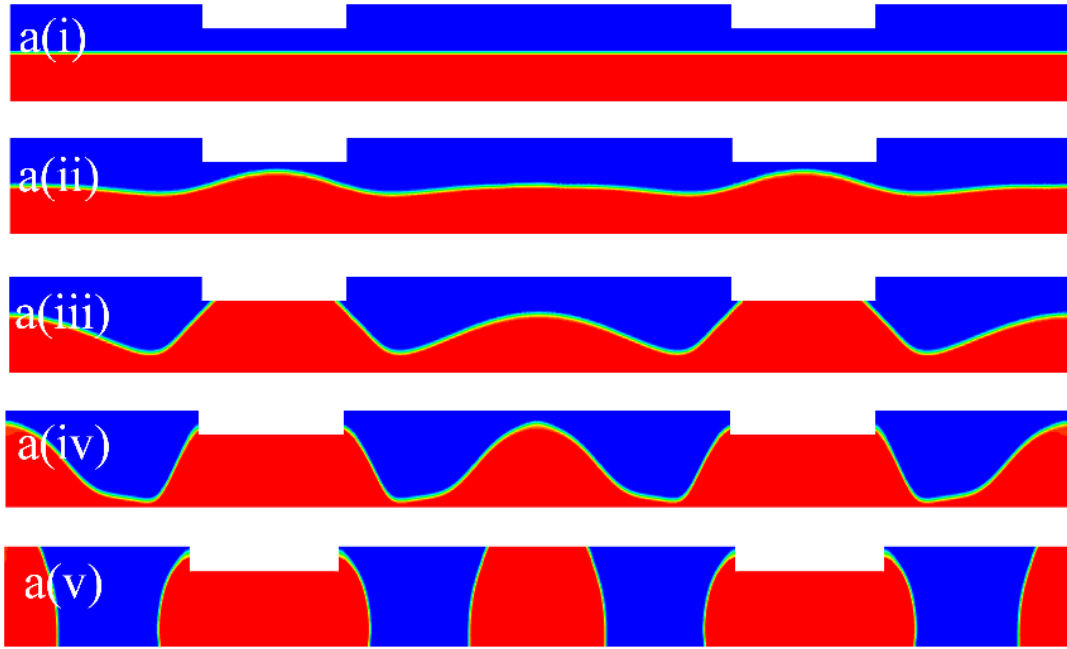


Figure 4.13. 2D time snapshots of the film interface in the TC induced patterning process focus on the secondary pillar formation, $\tilde{d}_1 = 2, \tilde{d}_2 = 1.5, \tilde{w} = 0.31, (\tilde{l}_p)_{VOF} = 0.82, \tilde{T} = 1,$ and $\lambda_{LS} = 2.03 \mu m.$

Figure 4.14 shows the snapshots of the thin film interface in the TC patterning obtained by the TF model. The formation of the primary and secondary pillars is similar to that of the VOF model. The primary pillar formed under each protrusion, and then the secondary pillar grew at later stages until it touched the top substrates (longer distance between substrates).

Figure 4.15 reveals the effect of the distance between neighboring protrusions (\tilde{l}_p) on the formation of secondary pillars. Fig. 4.11a(i) shows the case with $\tilde{l}_p < 0.8$, where no secondary pillars are formed. For the distances in the range of $0.8 < \tilde{l}_p < 1.4$, only one secondary pillar was formed, while multiple secondary pillars were generated for the higher spacing distances ($\tilde{l}_p > 1.4$). Evidently, the secondary pillars should be avoided when the high fidelity of the pattern replication is of concern since there is no control on the shape and size of the features.

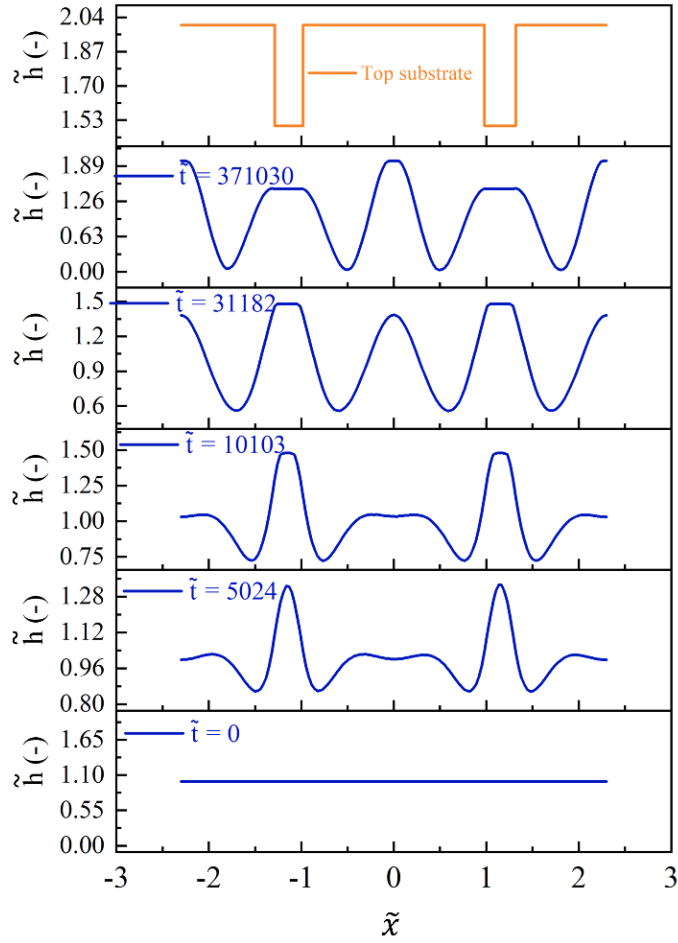


Figure 4.14. 2D time snapshots of the film interface in the TC induced patterning process focus on the secondary pillar formation, $\tilde{d}_1 = 2, \tilde{d}_2 = 1.5, \tilde{w} = 0.31, (\tilde{l}_p)_{VOF} = 2.1, \tilde{T} = 1,$ and $\lambda_{LS} = 2.03 \mu m.$

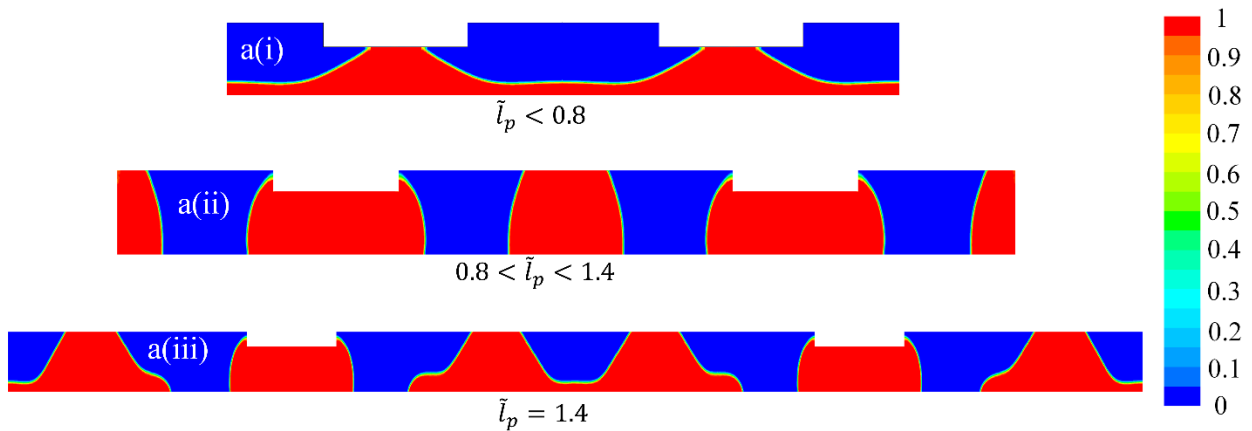


Figure 4.15. The final stage of the pattern formation for the different range of stamp periodicity where $\tilde{d}_2 = 1.5, \tilde{w} = 0.31$ and $\tilde{T} = 1.$

Similar to the map developed for the width of protrusions, we established a 2D map to find the threshold value for \tilde{l}_p that separates the patterns with primary and secondary pillars in both VOF and TF models. The effect of the distance between the protrusions on the number of pillars at different inverse filling ratios (\tilde{d}_2) are presented in Fig. 4.16. In both models, by increasing the distance between two protrusions beyond a threshold (say \tilde{l}_p^*), the secondary pillars appear. It is worth noting that even large spacing did not lead to the interface deformation for relatively high \tilde{d}_2 . Moreover, only primary pillars are formed under the protrusions. In all these cases, the Ma number remained constant since it affects the predicted value of \tilde{l}_p^* . In the VOF model, the equation of the dashed line in Fig. 4.16a is $(\tilde{l}_p)_{VOF} = 0.39\tilde{d}_2 - 0.04$, where $(\tilde{l}_p)_{VOF}$ is the scaled distance between two protrusions ($(\tilde{l}_p)_{VOF} = (l_p)_{VOF}/\lambda_{LS}$). By substituting the dimensionless parameters ($(l_p)_{VOF} = 0.9 \left(\frac{d_2}{h_0}\right) \lambda_{LS} - 0.36\lambda_{LS}$), the dimension size of the distance between two protrusions can be calculated and used as a preliminary choice for fabricating the patterned mask. On the other hand, a similar equation is obtained for the TF model, which is $(\tilde{l}_p)_{VOF} = 0.85\tilde{d}_2 - 0.02$ and its dimensional form is $(l_p)_{TF} = 0.85 \left(\frac{d_2}{h_0}\right) \lambda_{LS} - 0.02\lambda_{LS}$.

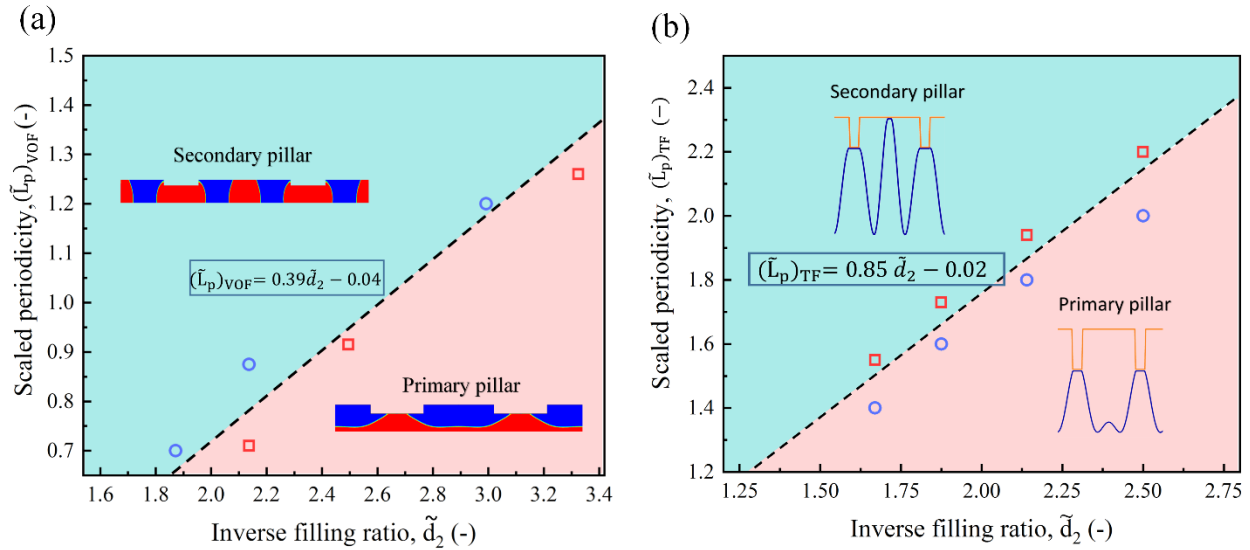


Figure 4.16. The threshold value for the distance between the protrusions at different polymer thicknesses where $\tilde{\omega} = 0.31$ and $\tilde{\Delta T} = 1$, (a) VOF model (b) TF model.

4.5. Conclusions

The volume of fluid (VOF) model, thin-film (TF) model, and linear stability (LS) analysis frameworks were used to simulate the thermocapillary (TC) induced instability and morphological evolutions in thin liquid films. In the VOF model, a multiphase flow interface tracking approach, the full continuity, Navier Stokes, energy, and volume fraction equations were solved. This also enables investigating more complex thin-film problems with multi-component films. The numerical approach presented in this study surpasses the long-wave limit inherent in the TF and LS models. It successfully predicts different interface deformation stages, including the initial linear and the late non-linear deformation. Compared to the experimental data[19], the VOF model predicted characteristic wavelength (λ) with significantly higher accuracy compared to the TF model and LS analysis. Several cases with different polymer thicknesses, gap spacing, and temperature differences were investigated to correlate the characteristic wavelength predicted by the VOF model and TF model with that theoretically found by the LS formulation. The effect of localized cooling/heating was also investigated by using a patterned top cold plate. Results showed that the interface deformation and pillar formation are sensitive to the localized cooled area (w , under the protrusions). It leads to the transition from single to twin pillars. The 2D maps for both VOF and TF model are generated based on the normalized width of the protrusions (\tilde{w}) and their separation distance (\tilde{l}_p), and the inverse filling ratio to predict the threshold values in which the transition from single- to two-pillar formation occurred and secondary pillar formed. Thus far, in all theoretical and numerical works in TC-induced patterning, the liquid film is assumed to be Newtonian with constant viscosity. However, many polymer solutions and molten polymers are non-Newtonian fluids. In the next chapter, a mathematical model is developed to characterize the thermocapillary destabilization of the air–polymer interface for non-Newtonian polymer films. A power-law model is adopted to model shear-thickening/thinning fluids and overcome the assumption limitations, such as the independence of viscosity from the shear rate.

Chapter 5 - Thermocapillary patterning of non-Newtonian thin films

5.1. Introduction

Interfacial instabilities of a thin film conduct interesting micro-and nano-sized patterns, with potential applications in microelectronics, drug delivery components, optoelectronic, and micro/nano- fluidic devices. There are different techniques for fabricating the patterns on liquid film surfaces, such as photolithography, nanoimprint lithography, and electron-beam lithography. Over the past few decades, some innovative approaches with low cost and high throughput have been developed to overcome lithographic process' limitations [115]. The lithographically induced self-assembly (LISA) is a recent novel approach that relies on self-organized instabilities triggered by external forces such as electrical [57,63,110,127], mechanical [146], and thermal [60,61]. Although LISA has a simple process to create micron and nano-scale patterns rather than conventional soft lithography techniques, the complexity of the mechanisms that lead to the destabilization of a thin polymer film must be summarized. Apart from patterning applications, thin-film instabilities expose the main fundamental issues on the rupture and deformation of the nanocomposite [147–152] and biological [153–155] membranes. Therefore, there have been many analytical and numerical works to understand the underlying science of thin-film instability and then control such instabilities to fabricate well-ordered structures with consistent sizes and shapes [18,22,116,121,122].

Thermally-induced instabilities in thick films (0.1-1 mm) are governed by short-wavelength Bénard-Marangoni instabilities and have been investigated over the past century [115]. Singer [60] reviewed thermocapillary approaches to polymer patterning and highlighted that these methods had been developed and applied only since the early 2010s. Moreover, the thermocapillary methods' merits over other patterning approaches assure that their uses will continue to expand and develop. Conversely, studies into nanofilms recently started with the preliminary finding of the one-dimensional ridge and two-dimensional pillar in an ultrathin molten polymer film heated from the bottom and cooled from above [63]. The image charge (SC)-induced electrohydrodynamics (EHD) instability model was proposed to justify the observations. However, Schaffer et al. [65,66] repeated the experiments with the same conditions but by grounding the

experiment setup. They ruled out the SC model as the responsible mechanism for instabilities growth and proposed an acoustic phonon (AP) model, which relies on low-frequency acoustic phonons as a dominant mechanism for the growth of micropillar formation. A model has been derived more recently based on the Bénard-Marangoni instability in the long-wave limit called thermocapillary (TC) model [18,19]. The temperature gradient at the polymer-air interface creates the surface tension non-homogeneity that applies a tangential TC stress at the interface. The TC stress destabilizes the interface, whereas the Laplace and viscous stresses tend to stabilize the interface. In the LW-TC instability, the film deforms and grows over time. It is a transient process like other self-organized pattern formation phenomena [59]. The formed structures' size and shape are highly dependent on the time when the system becomes cold to solidify the structures.

There have been many analytical and numerical works to understand the film's dynamics, instability, and morphological evolution. The previous studies are mostly focused on the use of simplified governing equations using a long-wave approximation for linear and nonlinear modes [84,112,137]. Many studies applied an analytical solution to evaluate the length and time scales in thermal-induced patterning process [19,63]. This nonlinear approach, called the "thin-film" equation, derived employing the lubrication approximation, assuming the film thickness much smaller than the wavelength for growing instabilities [$(h_0/\lambda) \ll 1$]. The thin-film equation is a fourth-order non-linear partial differential equation (PDE), and its solution provides the interface profile at each time step [13,22,58,103]. More recently, with developing the computational scheme enabling the interface tracking in the multi-phase flow systems, the computational fluid dynamic (CFD) is used considering the full momentum equations coupled with energy equation and employing stress balance boundary conditions [96,107,138,139]. Most of the studies carry on these polymer patterns considered the fluids to be Newtonian. The dynamics of polymer with complex rheology, however, have received less attention in the literature. The power-law fluid is an important type of a non-Newtonian fluid [156]. Some previous studies on a thin film of power-law fluids on a substrate have investigated the dynamics of films moving down inclined planes [157], falling films [158], films on cylinder [159] and rotation discs [160], and self-similar dynamics of rupture of thin free films [161].

A few studies have been devoted to the investigation of thermocapillary flows for viscoelastic flows [131,162–164]. The Marangoni convection is a shallow rectangular cavity of power-law fluids that have been studied, and the non-Newtonian effect on the temperature field, fluid flow, and heat transfer is

discussed [165,166]. Moreover, the impact of Marangoni convection for a power-law fluid for several power-law indexes is demonstrated [167]. The long-wave instability of a power-law fluid flowing down an inclined plane due to non-uniform heating has been studied [168]. The linear stability analysis has indicated that enhancing the downstream's plane temperature generates a significant stabilizing effect on the Newtonian fluid. Such an outcome is increased for the dilatant fluid while the stabilizing effect is reduced for the pseudoplastic fluid. Non-modal instability in plane Couette flow of a power-law fluid is examined. The results show that shear thinning considerably increases the amplitude of external force and initial conditions. Although several works have studied the influence of viscoelastic fluid in the thermocapillary and electrical induced patterning [21,169], the shear thinning and shear thickening effect for the thermal-induced patterning has not been discussed.

This study will employ the linear and nonlinear analysis for thermocapillary induced instability of power-law fluids to study the formed structures. In the proposed approach, a power-law model is implemented for the patterning of polymer film, and a thin-film equation for a shear-thinning/shear thickening fluid has been derived. The effect of power-law rheology on the time scale is studied. We study the effect of shear rate and viscosity variation on the size and number of formed pillars. The influence of effective parameters, including filling ratio and flow behavior indexes on the formed structures' final shape, is investigated

5.2. Mathematical Model

5.2.1. Problem statement

A three-dimensional (3D) schematic of the ultra-thin liquid film with the mean initial thickness of h_0 is shown in Figure 5.1. The liquid film and air bounding layer are heated from the bottom boundary (T_H) to above its glass transition temperature of the polymer (T_g) and cooled from the top boundary (T_C) so that $T_H - T_C > T_g$. A transverse thermal gradient at the interface generates an interfacial thermal pressure (a tangential TC stress) that leads to nonuniformity in the interfacial tension. A local decrease in the interfacial temperature leads to a higher interfacial tension compared to neighboring hot areas. The lower interfacial areas (hot region) are pulled toward higher interfacial areas (cold region), leading to interface deformation and pattern evolution in the thin film.

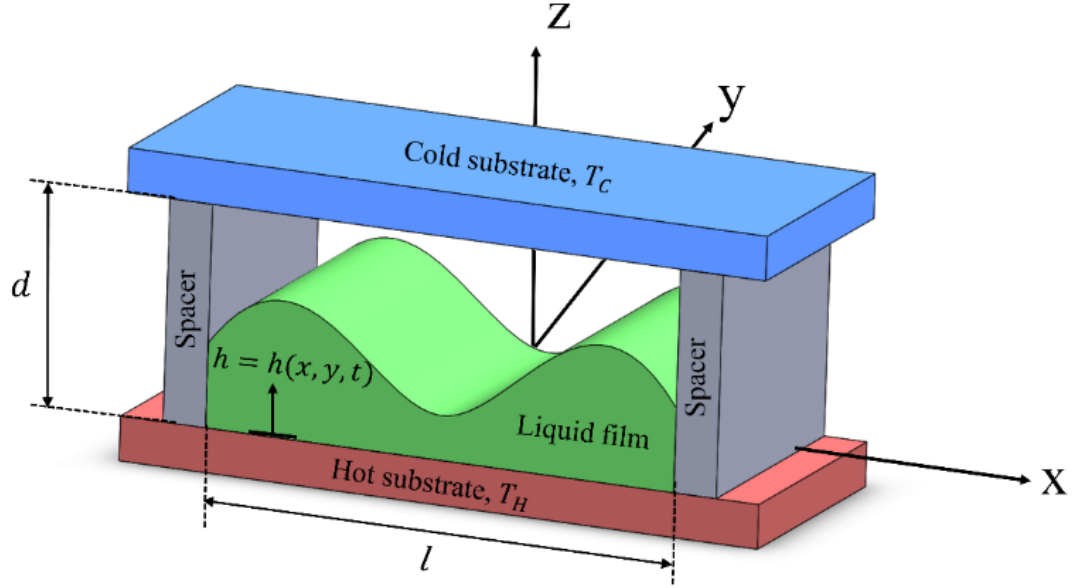


Figure 5.1. Schematic of the ultrathin liquid film placed between the top (cold) and bottom (hot) substrates, where $T_H > T_C > T_g$. Here, T_g is the glass transition temperature of the polymer film.

5.2.2. Power-law for modeling non-Newtonian fluids

Although most of the literature related to TC patterning is concerned with the Newtonian fluids, many polymers in industrial-scale patterning applications are non-Newtonian. An essential type of non-Newtonian fluid is the so-called power-law fluid and is widely used for molten polymers [170]. For power-law fluid, the viscous shear stress is proportional to the shear rate increased to an exponent, n , as follows:

$$\tau_{xy} = K\dot{\gamma}^n \quad (5.1)$$

where τ_{xy} is the shear stress, K is the flow consistency index, $\dot{\gamma}$ is the shear rate, and n is the dimensionless flow behavior index. The value of the exponent, n , can determine the fluid's rheology in terms of the applied shear. When n , is equal to unity, the fluid is Newtonian, for n less than one liquid is shear-thinning, whereas n is greater than one for a shear-thickening fluid. The effective viscosity, the viscosity of a Newtonian fluid that gives the same shear stress at the same shear rate, is expressed as a nonlinear function of the shear rate as follows:

$$\mu_{\text{eff}} = K\dot{\gamma}^{n-1} \quad (5.2)$$

where μ_{eff} is the effective viscosity. The shear rate ($\dot{\gamma}$) is the second invariant of the rate of deformation tensor (\mathbf{D}), which describes the rate of strain and shearing and is related to the viscosity gradient as follows:

$$\dot{\gamma} = \left[\frac{1}{2} (\mathbf{D} : \mathbf{D}) \right]^{\frac{1}{2}} \quad (5.3)$$

$$\mathbf{D} = \frac{1}{2} [\nabla \vec{u} + (\nabla \vec{u})^T] \quad (5.4)$$

where $\vec{u} = (u, v, w)$ is the flow velocity. Therefore, the effective viscosity is a nonlinear function of the symmetrized gradient of the velocity given by:

$$\mu_{\text{eff}} = \mu_0 [2K \dot{\gamma}]^{n-1} \quad (5.5)$$

where μ_0 is the zero-deformation-rate viscosity of the fluid ⁴⁰.

5.2.3. Thin-film evolution equation

To describe the spatiotemporal evolution of the film under TC stress, we employ the mass conservation, the Cauchy momentum and energy balances for an incompressible film, which are respectively written as

$$\nabla \cdot \vec{u}_i = 0, \quad (5.6)$$

$$\rho_i \left[\frac{\partial \vec{u}_i}{\partial t} + (\vec{u}_i \cdot \nabla) \vec{u}_i \right] = -\nabla \cdot \boldsymbol{\tau}, \quad (5.7)$$

$$\rho_i C_{p_i} \left(\frac{\partial T_i}{\partial t} + \vec{u}_i \cdot \nabla T_i \right) = k_i \nabla^2 T. \quad (5.8)$$

where $\boldsymbol{\tau}$ is the Cauchy stress tensor, which is defined as the summation of hydrostatic and viscous stresses. ($\boldsymbol{\tau} = -\tilde{p}\mathbf{I} + 2\mu_{\text{eff}}\mathbf{D}$). The pressure (\tilde{p}) is defined as ($p + \phi$). The term of p is capillary pressure, and $\phi = -\rho g z + \phi_{LW}$ incorporates the hydrodynamic pressure and intermolecular interactions. Since the film thickness is in the range of submicron, Lifshitz- van der Waals interactions, $\phi_{LW} = -A/6\pi h^3$, are considered (A is the effective Hamaker constant). Subscript i differentiates between the following fluid phases: molten polymer film and air as a bounding layer. In the energy balance equation, energy dissipation due to viscous forces is assumed to be

negligible. The thermal conductivity is k_i , heat capacity is C_{p_i} , and fluid velocity is \vec{u}_i . The Cauchy momentum equation, Eq. (5.8), can simplify using power-law model and Eq. (5.4) as follows:

$$\rho \left[\frac{\partial \mathbf{u}_i}{\partial t} + (\vec{u}_i \cdot \nabla) \vec{u}_i \right] = -\nabla \tilde{p} + \nabla \cdot [\mu_{\text{eff}} (\nabla \vec{u}_i + (\nabla \vec{u}_i)^T)] \quad (5.9)$$

The hydrodynamic and thermal boundary conditions are

$$\vec{u}_1 = 0; \quad T_1 = T_H \quad \text{at } z = 0, \quad (5.10)$$

$$\vec{u}_2 = 0; \quad T_2 = T_C \quad \text{at the top substrate,} \quad (5.11)$$

At the interface [$z = h(x, t)$] the boundary conditions are

$$\vec{u}_{\text{relative}} = 0 \quad \text{and} \quad T_1 = T_2, \quad (5.12)$$

$$\text{Thermal conduction: } \vec{n} \cdot (k_1 \nabla T_1 - k_2 \nabla T_2) = 0. \quad (5.13)$$

Finally, the normal and tangential stress balances are:

$$\vec{n} \cdot [\boldsymbol{\tau}_1 \cdot \vec{n} - \boldsymbol{\tau}_2 \cdot \vec{n}] = \kappa \sigma, \quad (5.14)$$

$$\vec{t}_j \cdot [\boldsymbol{\tau}_1 \cdot \vec{n} - \boldsymbol{\tau}_2 \cdot \vec{n}] = \nabla_s \sigma \cdot \vec{t}_j, \quad (5.15)$$

The term $\kappa \sigma$ is the mean interfacial curvature of the film interface while \vec{n} and \vec{t}_j are the normal and tangential vectors. The term $\nabla_s \sigma = (d\sigma/dT) \nabla_s T|_{z=h}$ is the interfacial tension gradient along the interface, which represents the TC pressure in the tangential stress balance at the interface. The surface tension is assumed to decrease linearly with the interfacial temperature [13], i.e., $\sigma = \sigma_0 - \sigma_T(T - T_0)$ where $\sigma_T (>0)$, σ_0 and T_0 are the surface tension gradient, the reference interfacial tension, and the reference temperature, respectively.

Finally, to relate the interface height to the interfacial velocity components, a kinematic boundary condition is imposed:

$$w = \frac{\partial h}{\partial t} + u \frac{\partial h}{\partial x} + v \frac{\partial h}{\partial y} \quad \text{at } z = h(x, y, t) \quad (5.16)$$

The governing equations (Eqs. (5.6), (5.8), and (5.9)) and boundary conditions (Eqs. (5.10)-(5.15)) are normalized using different scaling factors based on their physical significance. The initial film thickness (h_0) is used as a scaling factor for the vertical dimensions, whereas the characteristic wavelength for the growth of instabilities (L) is used to normalize the lateral dimensions.

$$\begin{aligned}
\tilde{d} &= \frac{d}{h_0}, & \tilde{t} &= \left(\frac{u_c}{L}\right)t, & \tilde{x} &= \frac{x}{L}, & \tilde{y} &= \frac{y}{L}, & \tilde{z} &= \frac{z}{h_0}, & \tilde{T} &= \frac{T - T_c}{\Delta T}, \\
\tilde{h} &= \frac{h}{h_0}, & \tilde{u} &= \frac{u}{u_c}, & \tilde{v} &= \frac{v}{u_c}, & \tilde{w} &= \frac{L w}{h_0 u_c}, \\
\tilde{p} &= \left(\frac{L}{\mu_0 u_c}\right)(p + \phi), & \tilde{\sigma} &= \frac{\sigma}{\mu_0 u_c}, & \tilde{A} &= \frac{A/(6\pi)}{(\mu_0 u_c/\epsilon h_0)}
\end{aligned} \tag{5.17}$$

Here $\epsilon = h_0/L$ is the ratio of initial film thickness to the lateral length scale, u_c is the characteristic lateral velocity and ΔT is the maximum temperature difference ($T_H - T_c$). Although the hydrodynamics of the polymer film is unaffected by the air bounding layer ($\mu_2/\mu_1 \ll 1$ and $\rho_2/\rho_1 \ll 1$), the two sets of governing equations (polymer and air) are coupled at the interface by stress balances. The Reynolds number, $Re = \rho u_c h_0/\mu_0$, is less than unity, so the flow is considered a creeping flow. Employing scaling factors and applying the long-wavelength approximation (ϵ and $\epsilon^2 \ll 1$), the governing equations are simplified as follows:

$$\tilde{\nabla} \cdot \tilde{u} = 0, \tag{5.18}$$

$$-\tilde{\nabla}_H \tilde{p} + \frac{\partial}{\partial \tilde{z}} \left(\mu_{\text{eff}} \frac{\partial \tilde{u}_H}{\partial \tilde{z}} \right) = 0 \quad , \quad \frac{\partial \tilde{p}}{\partial \tilde{z}} = 0 \tag{5.19}$$

$$\frac{\partial^2 \tilde{T}}{\partial \tilde{z}^2} = 0 \tag{5.20}$$

The corresponding boundary conditions on the walls are

$$\tilde{u}_1 = 0; \quad \tilde{T} = 1 \quad \text{at} \quad \tilde{z} = 0 \tag{5.21}$$

$$\tilde{T} = 0 \quad \text{at} \quad \tilde{z} = \tilde{d} \tag{5.22}$$

and at the interface [$\tilde{z} = \tilde{h}(\tilde{x}, \tilde{y}, \tilde{t})$] are

$$\tilde{u}_{\text{relative}} = 0 \quad \text{and} \quad \tilde{T}_1 = \tilde{T}_2 \tag{5.23}$$

$$\text{Thermal conduction: } k_1 d\tilde{T}_1/d\tilde{z} - k_2 d\tilde{T}_2/d\tilde{z} = 0$$

The stress balances are

$$\tilde{p} = -Ca^{-1} \nabla^2 \tilde{h} + Ca^{-1} Bo \tilde{h} + \tilde{A} \tilde{h}^{-3} \tag{5.24}$$

$$(\partial \tilde{u}/\partial \tilde{z}) = (\partial \Gamma/\partial \tilde{x}) \quad , \quad (\partial \tilde{v}/\partial \tilde{z}) = (\partial \Gamma/\partial \tilde{y}) \tag{5.25}$$

where $Ca = \mu_0 u_c / \epsilon^3 \sigma$ is the capillary number and $Bo = \rho g L^2 / \sigma$ is the Bond number. The term $\Gamma = \sigma / (\mu_0 u_c / \epsilon)$ is the scaled interfacial tension, and its gradient is related to the temperature gradient at the interface as

$$\nabla_s \Gamma = -Ma \nabla \tilde{T} |_{\tilde{z}=\tilde{h}}, \quad (5.26)$$

where $Ma = \epsilon \sigma_T \Delta T / (\mu_0 u_c)$ is the Marangoni number. From Eqs. (5.17) and its boundary conditions, the temperature distribution along the interface is given by $\tilde{T} |_{\tilde{z}=\tilde{h}} = k_r (\tilde{d} - \tilde{h}) / [(1 - k_r) \tilde{h} + k_r \tilde{d}]$ where $k_r = k_1 / k_2$ is the relative thermal conductivity of polymer and air. Substituting the temperature distribution into Eq. (5.26)

$$\nabla_s \Gamma = \frac{Ma k_r \tilde{d}}{[(1 - k_r) \tilde{h} + k_r \tilde{d}]^2} \nabla \tilde{h} \quad (5.27)$$

The characteristic lateral velocity, $u_c = \epsilon \sigma_T k_r \tilde{d} \Delta T / \{\mu_0 [k_r (\tilde{d} - 1) + 1]^2\}$ and Marangoni number, $Ma = ((1 - k_r) + k_r \tilde{d})^2 / k_r \tilde{d}$, are found when the film thickness \tilde{h} , interfacial slope $\nabla \tilde{h}$, and TC stress $(\partial \tilde{u} / \partial \tilde{z}) = (\partial \Gamma / \partial \tilde{x})$ in Eq. (5.27) are on the order of unity and are set to one. Obtaining the velocity components using Eqs. (5.18)-(5.25) and then substituting into the kinematic boundary condition relation

$$\frac{\partial \tilde{h}}{\partial \tilde{t}} + \tilde{\nabla}_H \cdot \int_0^{\tilde{h}} \tilde{u}_H d\tilde{z} = 0 \quad (5.28)$$

Results in the following scaled equation, which describes the spatiotemporal evolution of thin film.

$$\frac{\partial \tilde{h}}{\partial \tilde{t}} + \nabla \cdot \left[c_1 c_2 \tilde{h}^{\left(\frac{1}{n}+2\right)} (\nabla \tilde{p})^{\left(\frac{1}{n}\right)} + \frac{\tilde{h}^2}{2} \nabla(\Gamma) \right] = 0 \quad (5.29)$$

where $c_1 = \left(1 / K^{n-1} \sqrt{2}^{n-1}\right)^{\frac{1}{n}}$ and $c_2 = (2n^2 - (n+1)(2n+1)) / (2n^2 - (n+1)(2n+1))$.

The first term indicates the transient term of thin-film evolution, the second term (first term in bracket) shows the stabilizing force due to Laplace pressure, and the last term presents the destabilizing force due to TC stress.

5.2.4. Linear stability analysis

Linear stability (LS) analysis is conducted for the thin film evolution equation to predict the maximum and characteristic wavelength of the TC instabilities. The corresponding wavelength is obtained by replacing the uniform interface height (\tilde{h}) in the thin film equation with a periodic perturbation of $\tilde{h} = 1 + \xi \exp[\bar{\kappa}(\tilde{x} + \tilde{y})i + S(\bar{\kappa})\tilde{t}]$, where $i = \sqrt{-1}$, $\bar{\kappa}$ is the wavenumber, $S(\bar{\kappa})$ is the growth coefficient, and ξ ("1) is the infinitesimal amplitude coefficient. The wavenumber corresponds to the growth rate $[S(\bar{\kappa})]$ and the wavelength ($\lambda = 2\pi L/\bar{\kappa}$). After substituting \tilde{h} in Eq. (5.29) with sinusoidal perturbation, and neglecting all resulting nonlinear terms, a dispersion relation is calculated as follows:

$$S(\bar{\kappa}) + \frac{\bar{\kappa}^4}{Ca} - \frac{3nMa k_r \tilde{d}}{2c_1 c_2 [(1-k_r) + k_r \tilde{d}]^2} \bar{\kappa}^2 = 0. \quad (5.30)$$

When this dispersion relation $S(\bar{\kappa}_0) = 0$, the disturbance remains unchanged over time. The film remains stable if $S(\bar{\kappa}_0) < 0$, indicates the disturbances are damped over time. When $S(\bar{\kappa}_0) > 0$, there is always a wavenumber, $0 < \bar{\kappa} < \bar{\kappa}_0 = \sqrt{(3n Ca Ma k_r \tilde{d})/2c_1 c_2 [(1 - k_r) + k_r \tilde{d}]^2}$, shows TC-induced instabilities in nanofilms always lead to a pattern formation at this condition.

The fastest-growing wavelength (λ_{LS}) corresponds to the positive root of $\frac{\partial S}{\partial \bar{\kappa}} = 0$,

$$\lambda_{max} = 2\pi[h_0(1 - k_r) + k_r d_2] \sqrt{\frac{4 c_1 c_2 \sigma h_0}{3n d_2 \sigma_T k_r \Delta T}}. \quad (5.31)$$

A list of all dimensionless numbers and their values in this study is presented in Table 5.1.

Table 5.1. List of dimensionless parameters and their values.

Dimensionless number	Definition	Value
Interface height (\tilde{h})	$h(x, y, t)/h_0$	0.02-4.00
Marangoni number (Ma)	$[(1 - k_r) + k_r \tilde{d}]^2 / k_r \tilde{d}$	1.56-9.69
Capillary number (Ca)	$\mu_0 u_c / \epsilon^3 \sigma$	1.00-52.67
Bond number (Bo)	$\rho g L^2 / \sigma$	10^{-8} - 10^{-6}
Inverse filling ratio (\tilde{d})	d/h_0	1.5-4.0
Slender gap ratio (ϵ)	h_0/λ_{max}	0.1-0.01

5.2.5. Numerical modeling

To obtain the dynamics, instability, and morphological evolution of the nanofilms, we solved the nonlinear thin film equation (Eq. (5.29)) that is a 4th order nonlinear partial differential equation (PDE). Employing the finite difference discretization and applying a second-order central finite difference scheme that converts the PDE to a linear system of differential algebraic equations (DAEs) in time:

$$F(\tilde{t}, \tilde{h}, \partial\tilde{h}/\partial\tilde{t}) = 0, \quad (5.32)$$

where F , \tilde{h} , and $\partial\tilde{h}/\partial\tilde{t}$ are vectors and their lengths are related to the dimension of the spatial grid. Differential algebraic solver (DASSL) with an adapting time stepping is used to solve the resulting sets of DAEs [171–173]. Numerical simulations performed in a square domain with the length of $5\lambda_{\max}$ using a periodic boundary conditions. The domain size is large enough to ensure that the instabilities will not damp due to small computational domain constraints [17]. A volume conserving random distribution is employed for the initial condition of the interface height that avoids any spatial bias for instabilities growth [62,84]. Many laboratory experiments have used polystyrene (PS) [112], and we also consider constants and parameters obtained from the reported properties of PS polymer [17–19,51,66,112] for our computations. The properties are summarized in Table 5.2.

Table 5.2. Constants and parameters used in simulations.

Parameter	Value
Interface tension (σ)	0.045 N/m
Interfacial tension gradient (σ_T)	88.5×10^{-5} N/m °C
Viscosity of liquid film (μ)	1 Pa.s
Thermal conductivity of liquid film (k_p)	0.13 W/m °C
Thermal conductivity of air (k_a)	0.036 W/m °C
Effective Hamaker constant (A)	-1.5×10^{-21} J
Mean initial film thickness (h_0)	25-65 nm
Plate separation distance (d)	100 nm
Equilibrium distance (l_0)	1 nm
Temperature difference (ΔT)	46 °C
Speed of sound in the polymer (u_p)	1850 m/s

Different spatial grid element sizes are considered to find the optimum mesh size that can predict the interface deformation accurately with the minimal computational expense. Three cases (Grid 1, Grid 2, and Grid 3) are presented here to illustrate the effect of the spatial grid on the results. Here, the number of grid points is increased from Grid 1 (61×61) to Grid 3 (121×121) while keeping the same uniform Cartesian grid distribution. The exact location of the interface for each grid is compared, and the results are presented in Fig. 5.2. The error shown in the table is calculated as follows:

$$error (\%) = \frac{1}{n} \sum_{i=1}^n \frac{h_{new,i} - h_{old,i}}{h_{old,i}} \times 100 \quad (5.33)$$

where n is the number of extracted data points for interface height. The relative mean error is less than 2% for Grid 2, which shows that this mesh size (91×91) is sufficient to track the interface deformation accurately.

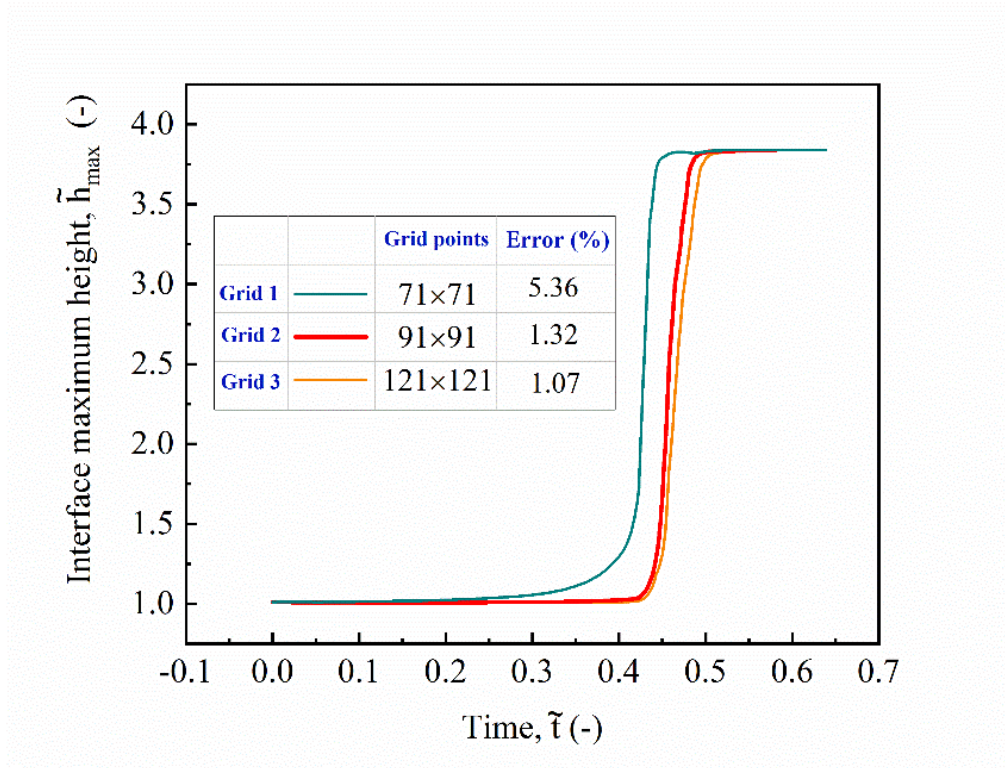


Figure 5 2. The effect of grid size on transient growth of interface height

5.3. Results and Discussion

5.3.1. Newtonian Fluid

A Newtonian fluid film ($n=1$) is simulated as a baseline case compared to provide insight into the effect of rheology on the TC pattern formation process. The height of the liquid film is 25 nm, and the distance between the two substrates is 100 nm, while the temperature difference is 46 °C. Fig. 5.3a shows the maximum and minimum interface height location over time. This plot also shows the time which the first pillar touches the upper cold plate. The initial random perturbations redistribute and grow slowly in time at the early stage of pattern evolution and followed with an exponential growth until the first pillar touch the top substrate ($\tilde{t} = 0.25$). Pillars are formed and randomly distributed over the domain area, and the number of formed pillars increases over time. The minimum height proceeds to decrease until the thickness of the liquid film reaches the born repulsion length (l_0). Fig. 5.3b shows a 3D plot of a thin film interface after all pillars reached the top substrate. It indicates the random distribution of pillars across the domain and their columnar and final shape at the quasi-steady stage of the patterning process.

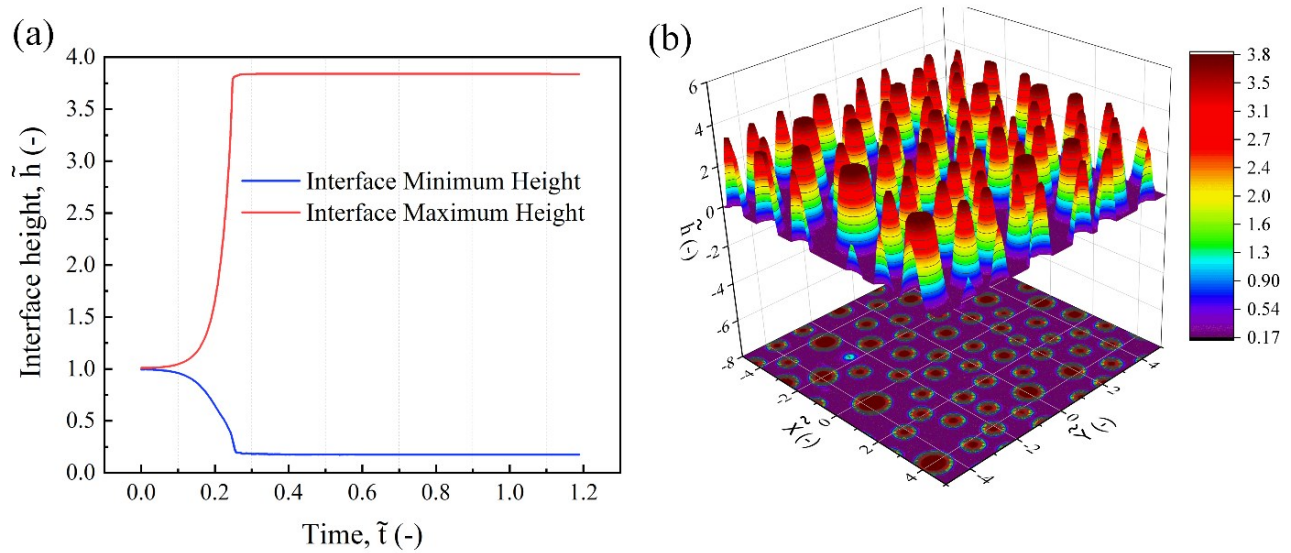


Figure 5.3. (a) Nondimensional pillars' height over time for a Newtonian fluid ($n=1$), (b) Plot showing 3D pillar distribution for a Newtonian film with $h_0 = 25$ nm.

5.3.2. Time scale and spatiotemporal evolution in non-Newtonian TC patterning

In the TC process, the transition from pillars to the bicontinuous structure is observed when the filling ratio (h_0/d) is more than 0.5 [19,84,96]. In the present study, we focus on the filling ratio of less than 0.5. The tracking of minimum and maximum interface height over time, along with the 3D and 2D snapshots of the liquid film interface for a shear-thinning case ($n=0.75$) at different stages of the evolution process, are presented in Fig 5.4. Image shows the interface maximum and minimum height over time. It grew exponentially from the early stages until it reached the top substrate at the scaled time of 0.49. Compared to the Newtonian case shown in (Fig. 5.3a), the growth rate of the TC-induced instabilities is slower in a similar shear-thinning fluid film. Initial random perturbations redistributed at the early stages of pattern formation into ridges and valleys and form bicontinuous structures. After that, fragmentation happens, and isolated islands are formed. A negative liquid flow from thinner regions of the film to the thicker ones results in amplification of the interface height at thicker regions and leading to a pillar formation (stage (i)). After bridging top and bottom substrates, there is an increase in contact area over time which causes to form columnar raised structures with circular cross-sections or pillars (stage (ii) and stage (iii)). Fig. 5.5c shows the final shape and size of formed pillars from the top view at the end of the process. The maximum and average shear rate variation over time is presented in Fig. 5.5d. At the beginning of the TC process, the shear rate is low since random perturbations' growth rate is still slow. Once the fastest growth pillar moves towards the top substrate, the shear rate increases and reaches its maximum. This is the stage where the highest polymer deformation happens. After the first pillar reached the top substrate, the remaining polymer, which is in the later stage of pattern formation and close to touch the top surface, starts to flow faster and form more pillars over time, resulting in higher shear rates. After the scaled time of 0.49, the maximum and average shear rate remained almost unchanged.

Fig. 5.5 shows the interface's tracking over time along with the 3D snapshots of the thin film interface for a shear-thickening case ($n=1.2$) at different stages of pattern formation. Fig. 5.5a shows that the fastest growth pillar touched the top substrate after a scaled time of 0.17, which is faster than that of shear-thinning ($\tilde{t} = 0.49$) and Newtonian ($\tilde{t} = 0.25$) cases. Fig. 5.5b(i-iii) shows 3D snapshots of the pattern evolution in a shear-thickening case. When the first pillar touched the

top substrate, other interface undulations are still at the early stages of pattern formation (Fig. 5.5b(ii)). However, in the shear-thinning case shown in Fig. 5.4b(ii), the interface undulation is well progressed and reached close to the top plate when the first pillar bridges the top and bottom plate. This difference is correlated to the shear rate variation as the pillars form, which is depicted in Fig. 5.5d. The magnitude of shear rate (both maximum and average) in the shear-thinning case is higher than that in the shear-thickening case. Also, there is a fluctuation in the shear rate plot after the scaled time of 0.17, likely due to gradual pillar formation with different sizes.

The number of formed pillars in the shear-thickening case is higher than the shear-thinning and Newtonian cases, as shown in Fig. 5.5c. Consequently, the TC patterning process in the shear thickening case is faster, and the number of pillars is much more than that of the shear-thinning case.

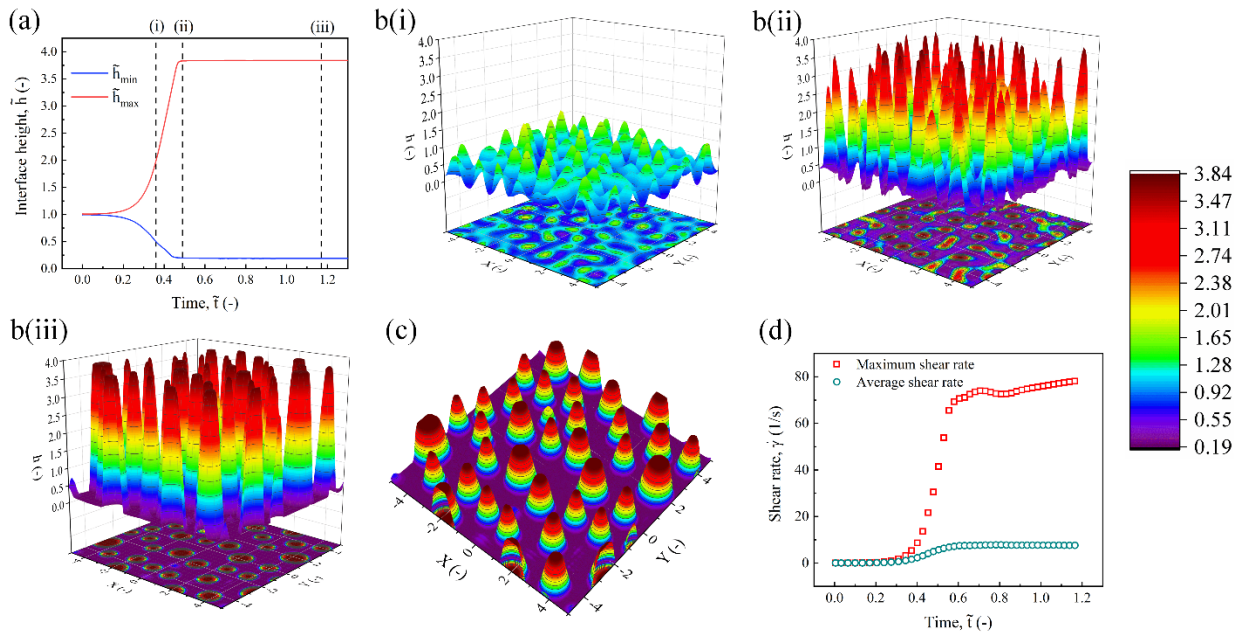


Figure 5.4. Interface height of the fastest growth pillar and 3D snapshots of the interface structure over time for a shear-thinning case ($n=0.75$), (a) Maximum and minimum interface height vs. time, (b(i-iii)) 3D and 2D snapshots of the interface at three different times; b(i) $\tilde{t} = 0.36$, b(ii) $\tilde{t} = 0.45$, b(iii) $\tilde{t} = 1.17$. The parameters in this study are $h_0 = 25$ nm, $d = 100$ nm, $\Delta T = 46$ °C, and $n = 0.75$. (c) Final shape and structure of the pillars from top view, (d) Nondimensional pillars' shear rate versus scaled time for a shear thinning case.

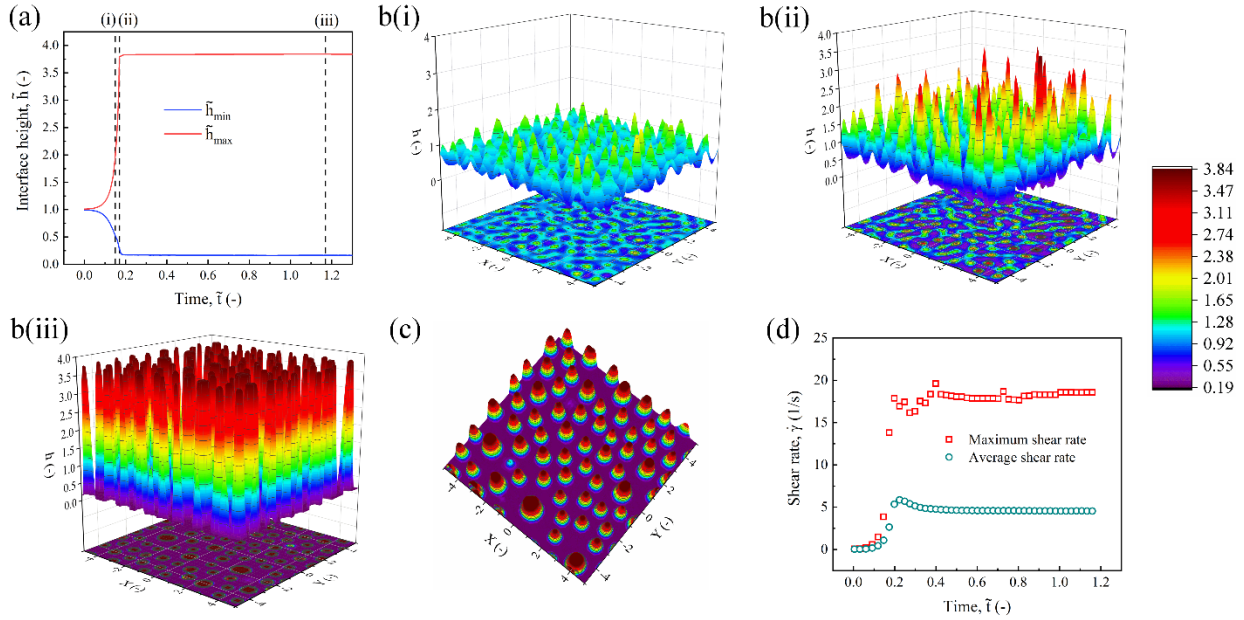


Figure 5.5. Interface height of the fastest growth pillar and 3D snapshots of the interface structure over time for a shear-thickening case ($n=1.2$), (a) Maximum and minimum interface height vs. time, (b(i-iii)) 3D and 2D snapshots of the interface at three different times; b(i) $\bar{t} = 0.15$, b(ii) $\bar{t} = 0.17$, b(iii) $\bar{t} = 1.17$. The parameters in this study are $h_0 = 25$ nm, $d = 100$ nm, $\Delta T = 46$ °C, and $n = 1.2$, (c) Final shape and structure of the pillars from the top view, (d) Nondimensional pillars' shear rate versus scaled time for a shear thickening case.

5.3.3. Local effective viscosity distribution and its effect on pattern morphology

The effect of local variation in viscosity on the dynamics and morphology of the interface is studied. In contrast to the Newtonian fluid that the fluid resistance against motion remains unchanged; in the power-law model's resistance is a function of shear rate, which is not constant during the TC-induced patterning formation. The TC stress acting on the interface varies as the film thickness changes. The thinner areas experience lower TC stress than the thicker regions, and consequently, the pillar growth accelerates as the pillar's height increases. In Fig. 5.6, the variation of scaled viscosity over time is correlated to the interface height profile for a shear-thinning case. The average and minimum scaled viscosity over time is presented in Fig. 5.6b. The scaled viscosity has its higher value at the beginning of the process, whereas the shear rate has its minimum value (Fig. 5.4b). The scaled viscosity sharply decreases from 0.17 to 0.02 where the first pillar touched the top plate (stage (ii)), then it remained unchanged. The maximum viscosity reduction from the early stage of pattern formation to the end of the process is about 88%, significantly affecting the size and final shape of the structures in a shear-thinning case. Fig. 5.6c(i-iii) shows the 2D

snapshots of the interface height profile at three pattern formation stages. The blue color indicates the minimum interface height, and the red color represents the maximum interface height. Initially, the interface deforms due to the presence of TC stress (stage (i)), and then the first pillar reached the top substrate at the scaled time of 0.49 (stage (ii)). Meanwhile, other formed pillars have reached close to the top plate. The quasi-steady stage of pattern formation where the pattern remained unchanged is presented in Fig. 5.6c(iii).

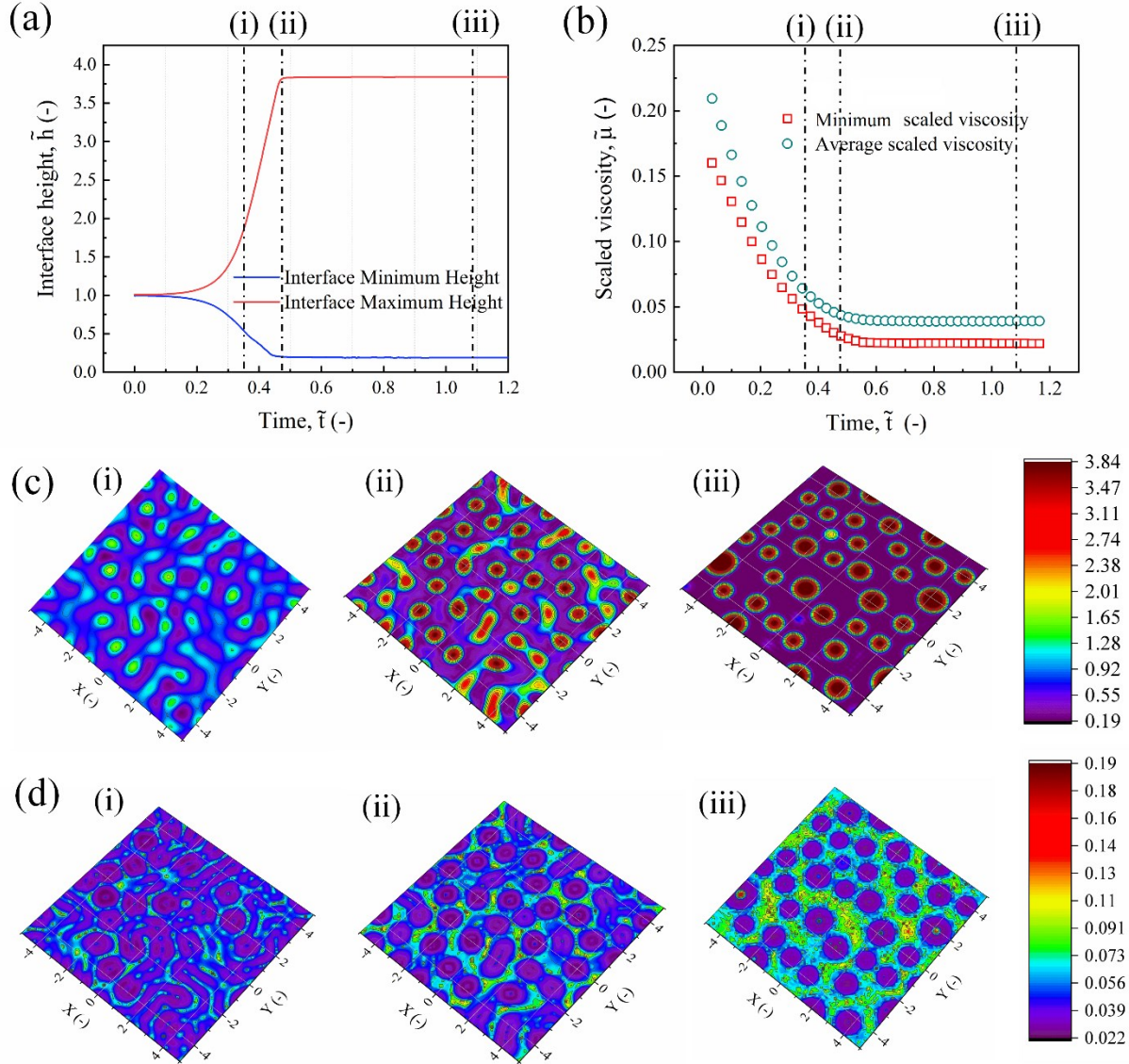


Figure 5.6. (a) Tracking interface height over time for a shear-thinning fluid ($n=0.75$), (b) Nondimensional pillars' viscosity versus scaled time for a shear-thinning film, (c(i-iii)) Spatiotemporal evolution of the interface at nondimensional times $\bar{t} = 0.36$, $\bar{t} = 0.49$ and $\bar{t} = 1.17$, (d(i-iii)) Effective viscosity distribution at nondimensional times $\bar{t} = 0.36$, $\bar{t} = 0.49$ and $\bar{t} = 1.17$.

In Fig. 5.6d(i-iii), the 2D contour plots of local scaled viscosity are presented at the same time snapshots of Fig. 5.6c. The locations of minimum viscosity are located where the gradient of interface height with respect to the x and y direction is small. For instance, at points where pillars touched the top plate, the effect of viscosity variation is negligible. Shear-thinning of fluid occurred in rings around the pillars due to a higher shear rate of deformation in those regions. Moreover, since the scaled viscosity values are less than unity, the effective viscosity would be smaller than that in the Newtonian case.

However, Fig. 5.7a shows the first pillar reached the top substrate in the scaled time of 0.17, which is faster than the pseudoplastic case. The scaled maximum and minimum viscosity experienced a sharp increase from the first stage to the final stage of the pattern evolution as the shear rate increases (Fig. 5.7b). The maximum viscosity is greater than unity; therefore, the effective viscosity is greater than the similar Newtonian case. The 2D snapshots of interface height profile in a shear-thickening case are presented in Fig. 5.7c. However, the number of formed pillars at the end of the process increases compared to the Newtonian and shear-thinning cases. Fig. 5.7d shows that the location of maximum viscosity is substantially the same as those where pillars are formed. This can be attributed to the shear-thickening behavior of the fluid. In TC, the pillars formed in those locations with the highest shear rates in the fluid. A high shear rate makes the fluid more viscous in those regions, increasing its local viscosity.

5.3.4. Rheological effects on pillar density and the characteristic wavelength

The effect of rheology on the pillar density, the characteristic wavelength, and the final formed pattern is investigated. Fig. 5.8 shows the effect of film thickness and flow behavior index on the characteristic wavelength predicted by linear stability (LS) analysis. The distance between the two plates is set to 100 nm, and the temperature difference is 46 °C. Fig. 5.8a indicates as the flow behavior index increases, the characteristic wavelength decreases at all film thickness values. The λ_{max} obtained from LS for a shear thickening case ($n=1.2$) is smaller than a shear-thinning case ($n=0.75$) for a constant film thickness. The λ_{max} profile for different initial film thicknesses is presented in Fig. 5.8b. In both shear thinning and shear thickening case, it shows a parabolic increase reaching its maximum at $h_0 = 46 \text{ nm}$. To obtain the maximum point, the derivative of λ_{max} in LS concerning h_0 is set to zero ($d\lambda/dh_0 = 0$) in Eq. (5.31). Therefore, a relation is found for d/h_0 as a function of k_r as $(d/h_0) = 3(1 - k_r)/(-k_r)$. Since k_r is a material property, the

maximum value for \tilde{d} can be adjusted based on the geometrical limitations concerning the thermal properties of the film. In this study, where the ratio of the thermal conductivity of polymer to air is $k_r = 3.61$, and the distance between two substrates is 100 nm, h_0 is found as 46 nm showed by dash-line in Fig. 5.8b. This extremum point is found independent of the flow index parameter; however, the rate of change in λ_{max} as the film thickness varies is higher in shear-thinning fluids.

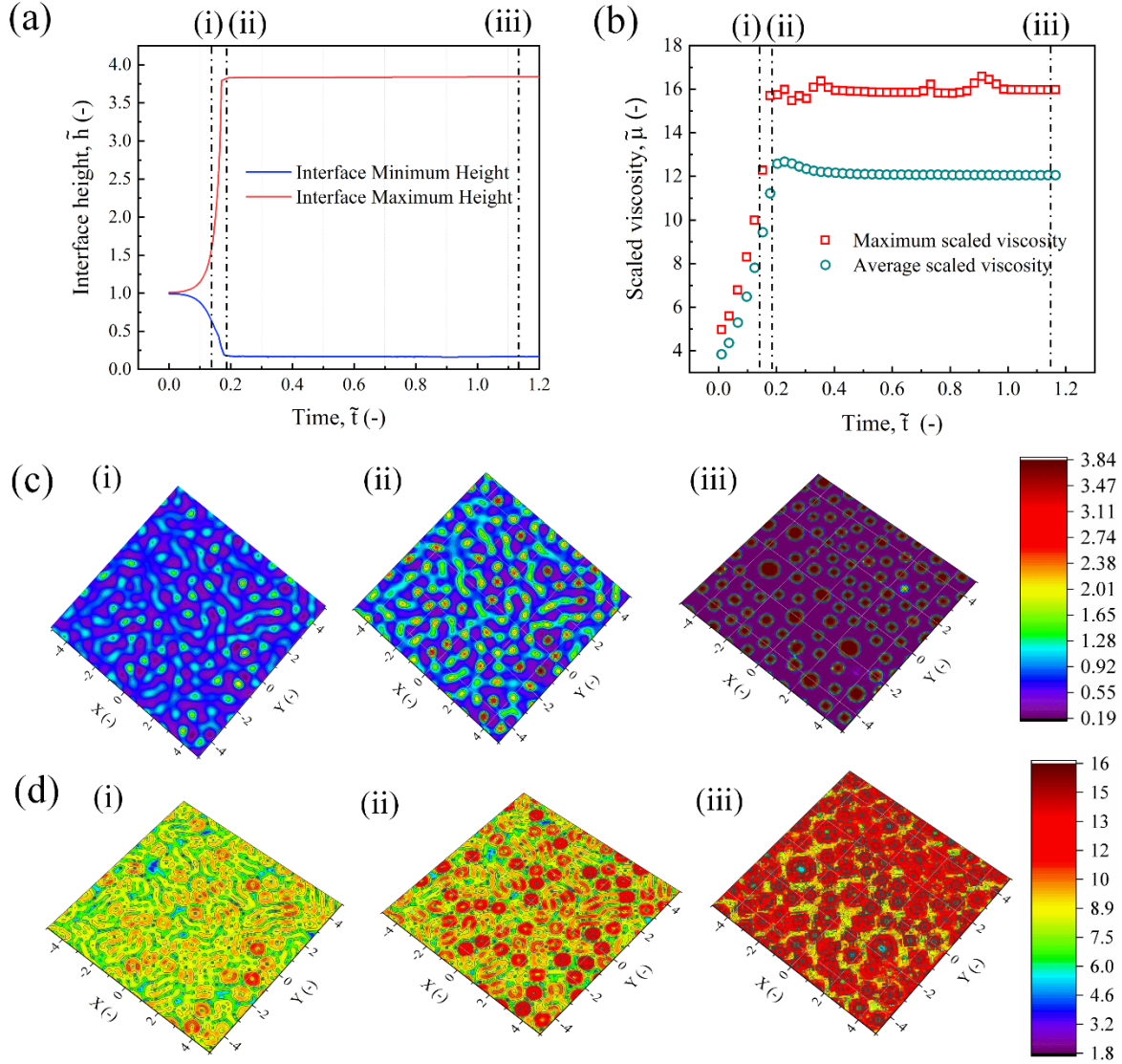


Figure 5.7. (a) Tracking interface height over time for a shear-thickening fluid ($n=1.2$), (b) Nondimensional pillars' viscosity versus scaled time for a shear thickening film, (c(i-iii)) Spatiotemporal evolution of the interface at nondimensional times $\tilde{t} = 0.15$, $\tilde{t} = 0.17$ and $\tilde{t} = 1.17$, (d(i-iii)) Effective viscosity distribution at nondimensional times $\tilde{t} = 0.15$, $\tilde{t} = 0.17$ and $\tilde{t} = 1.17$.

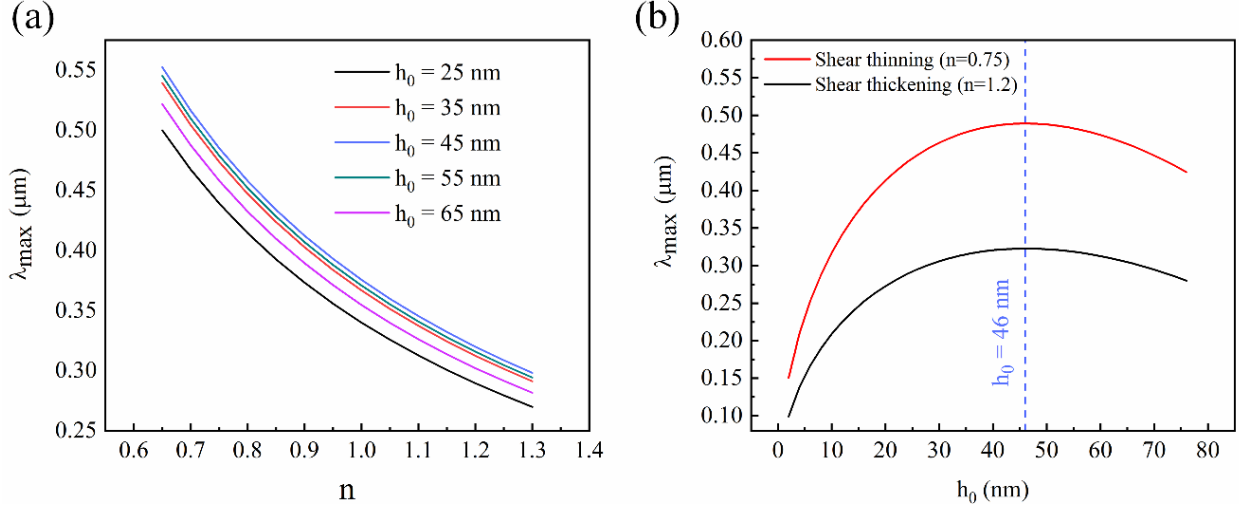


Figure 5.8. (a) The characteristic wavelength obtained from linear stability (LS) analysis versus flow behavior index for different film thicknesses, (b) The characteristic wavelength at different film thicknesses for both shear thinning and shear thickening cases.

3D snapshots of the interface at the quasi-steady stage of pattern formation for a shear-thinning liquid film for different filling ratios are compared in Figs. 5.4(i-v). There is a change in pattern morphology from bicontinuous structures (Fig. 5.4(i)) to pillars (Fig. 5.4(v)) as the film thickness decreases. For a small value of \tilde{d} (thicker films), the formed pillars are tightly arranged that increases the merging of neighboring pillars. Therefore, regardless of the size of formed pillars, using thinner films is recommended. The Ma , which defines the relative strength of the TC force to the viscous force, increases linearly with \tilde{d} . The trend of the characteristic wavelength predicted by LS (blue line of 2D plot in Fig. 5.9) was already discussed in Fig. 5.8b, which shows either using very thin (large \tilde{d}) or very thick (small \tilde{d}) films lead to well-organized pillar structures. However, the nonlinear simulation illustrates that the desired columnar structures are obtained with thinner films as in thicker films, the coalescence of neighbor pillars leads to coarse structure formation.

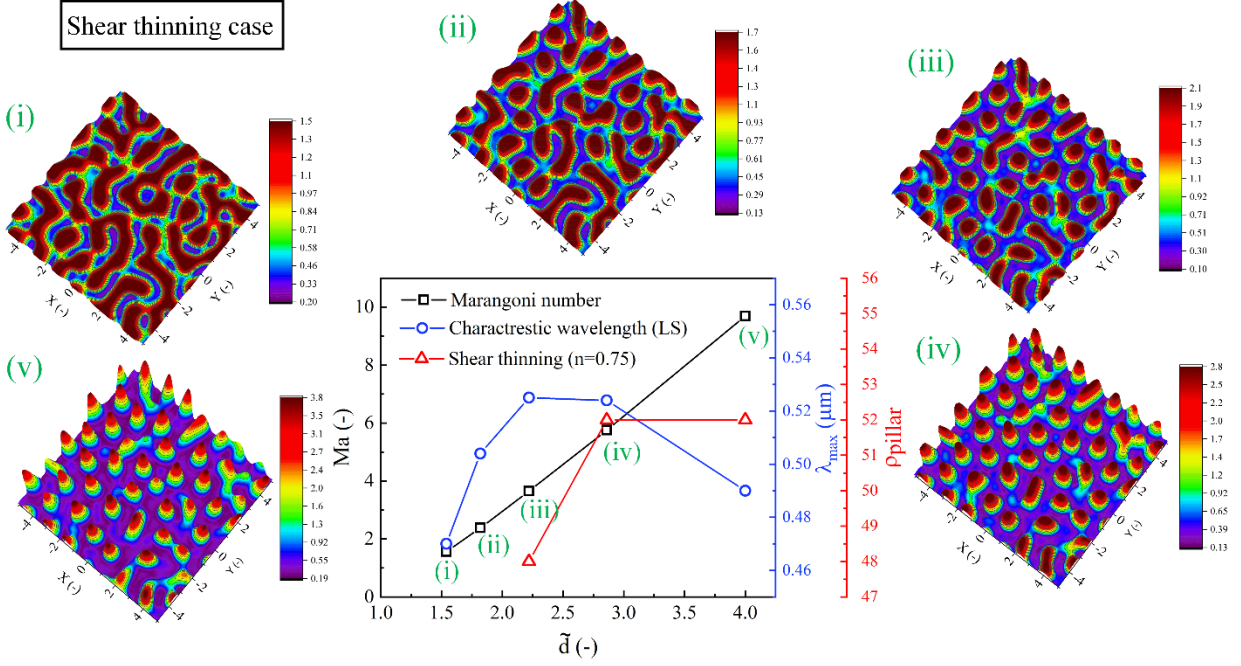


Figure 5.9. Shear thinning case, (i-v) 3D snapshots of the interface profile. Initial film thickness, $h_0 =$ (i) 65 nm, (ii) 55 nm, (iii) 45 nm, (iv) 35 nm, (v) 25 nm. $Ma =$ (i) 1.54, (ii) 2.38, (iii) 3.65, (iv) 5.76, and (v) 9.69. Plates distance, $d = 100$ nm, temperature difference, $\Delta T = 46$ °C.

The red line in Fig. 5.9 shows the pillar number density, ρ_{pillar} , which is defined as the number of pillars formed in $1 \mu m^2$ area. The higher the ρ_{pillar} indicates the compactness of the structure formed. It is worth noting that in bicontinuous structures (case (i) and case (ii)), the pillar density cannot be defined. Although increasing \tilde{d} causes well-defined pillars, which are more stable and where λ_{max} is comparatively small, the pillar density changes insignificantly. In TC patterning, both the size and uniformity (less coarsening effect) of the formed structures are important. Based on the nonlinear outcome for both shear thinning and shear thickening cases, a system with $\tilde{d} > 2.5$ (cases (iv) and (v)) have higher chances to result in smaller and more stable pillars.

3D snapshots of the features form at the quasi-steady stage of pattern formation, and a 2D plot of Ma , the characteristic wavelength, and pillar density at the different filling ratios for a shear thickening case are presented in Fig. 5.10. The trend of changing the morphology of features is found similar to the shear-thinning case shown in Fig. 5.9. However, the number of formed pillars is nearly half of that in a shear-thinning case.

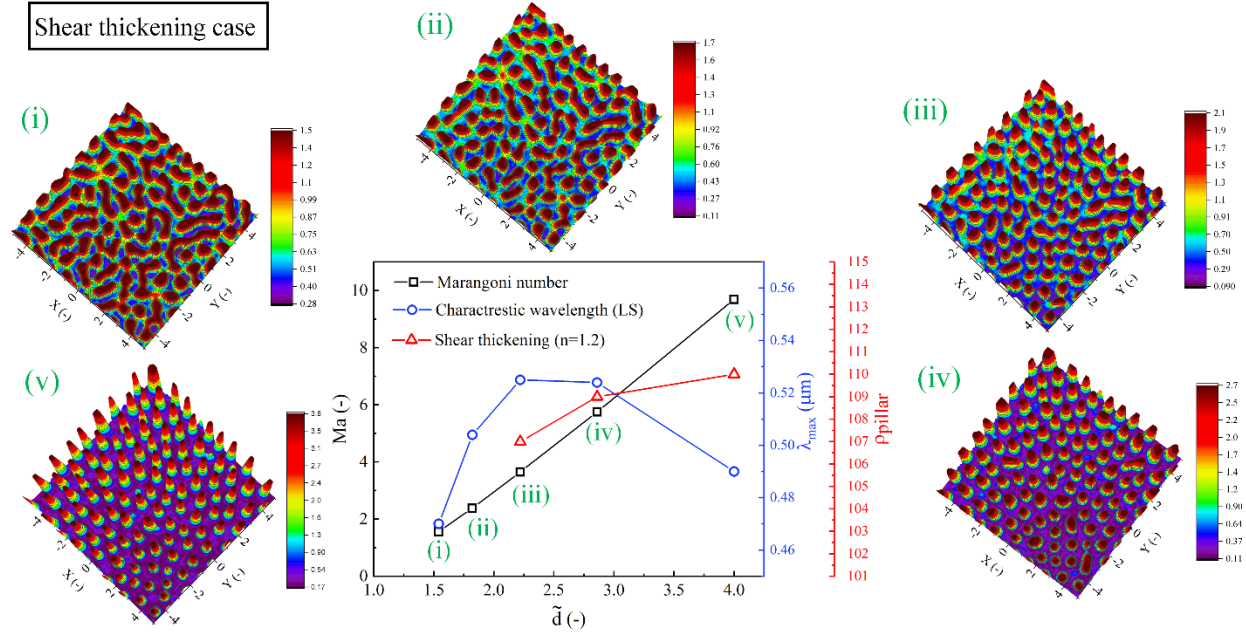


Figure 5.10. Shear thickening case, (i-v) 3D snapshots of the interface profile. Initial film thickness, $h_0 =$ (i) 65 nm, (ii) 55 nm, (iii) 45 nm, (iv) 35 nm, (v) 25 nm. $Ma =$ (i) 1.54, (ii) 2.38, (iii) 3.65, (iv) 5.76, and (v) 9.69. Plates distance, $d = 100$ nm, temperature difference, $\Delta T = 46$ °C.

5.4. Conclusions

The dynamics, instability, and pattern formation of thermally induced instabilities in thin liquid films are studied numerically. We have investigated the nonlinear interface deformations in shear-thinning and shear-thickening confined fluid films under transverse thermal gradient. Lubrication theory and the power-law model are employed to derive a fourth-order nonlinear thin film equation, which describes the spatiotemporal evolution of the polymer-air interface and the local viscosity variation. The thin-film equation is parametrized by the system's physical properties, such as the interfacial tension, temperature difference, the viscosity, thermal conductivity of polymer and air, and flow behavior index. The finite difference with pseudo-staggered discretization and an adaptive time step is used to solve the nonlinear thin film equation. Linear stability (LS) analysis is then applied to find the characteristic wavelength for the growth of instabilities. The results show that the growth rate of instabilities and the time takes the first pillar touches the top substrate is strongly affected by the power-law index and is relatively longer for shear-thinning ($\tilde{\epsilon} = 0.49$) than shear thickening ($\tilde{\epsilon} = 0.17$). The effect of local variation in viscosity on the dynamics and morphology of the interface is also studied. In shear-thinning fluid film, the pillars

are formed where the viscosity experiences its minimum value. In contrast, the pillars' location in a shear thickening case is the same spot that the viscosity reached its maximum value. The compactness and fidelity of the formed columnar structures have been investigated considering different filling ratios. It was found that the pillar density (number of pillars form in $1\mu m^2$ area) has improved as the fluid behavior index increased. An increase in the filling ratio \tilde{d} leads to smaller and more stable structures in both shear thinning and shear thickening fluid films.

Chapter 6 - Conclusion and future work

6.1. Conclusion

To enhance the thermal-induced (TC) patterning to achieve the smaller sized structures uniformly distributed over the whole domain area is the main objective of this thesis. Since there were discrepancies in predicting the characteristic wavelength obtained from the experimental data and theoretical models, a nonlinear numerical model with high accuracy was required to predict better the characteristic wavelength, which is the focus of this study. A phase-field numerical model was initially used to simulate the dynamic process of TC-induced patterning. In this model, the deformation liquid film connects to two-phase flow, as defined by the phase parameter. Using the phase field model, the dynamic thermal-induced patterning process was studied while highlighting various parameters' effects.

The non-uniform temperature along the polymer-air interface creates an interfacial tension gradient. The spatial heterogeneity of the surface tension force in the interface induces the non-uniform pressure distribution. This uneven pressure distribution is responsible for the flow mechanism and interface deformation in the TC patterning process. As time progressed, the pressure increases in the area under the protrusion as air is squeezed out of that region. This is due to the circulation effects in the gap between the protrusions, which forces the polymer upwards to create the patterns under each protrusion. It was found that the temperature gradient in the interface can significantly affect the dynamic process. Applying higher temperature gradient results in a higher TC-induced force on the interface through the pattern evolution and faster interface deformation. In terms of the effect of polymer's thermal conductivity, the temperature at the interface increases, which leads to a uniform temperature distribution at the interface. Thus, the processing time was longer. As protrusion height increased, it was observed that a large protrusion height could enhance the growth rate and could decrease the processing time.

However, a further increase in the protrusion height became insignificant. The width of top protrusions affects the size and number of pillars forming in the TC patterning process. When the width is higher than the characteristic wavelength, two small instabilities grow without merging leading to twin pillars under the protrusion. Examining the effect of the distance between two

protrusions revealed that as the primary pillars touched the top substrate, the residual polymer between pillars has formed secondary pillars. This indicated that pillars could form under protrusions and between them, depending on their spacing distance. This enables reducing the number of protrusions. Moreover, it was determined that the contact angle was critical in establishing the final structure of the pillars. Well-ordered pillars appeared when the surface had higher surface energy compared to the liquid film.

Using systematic study, it was shown that effective parameters impact the shape and size of the final features. However, further studies were needed to show the relationship between the characteristic wavelength obtained by linear stability analysis and the CFD model. Hence, the second part of this thesis focused on how the temperature difference, polymer thickness, and the distance between two substrates impact the characteristic wavelength of created pillars. The volume of fluid (VOF) model, thin-film (TF) model, and linear stability (LS) analysis frameworks were used to simulate the thermocapillary (TC) induced instability and morphological evolutions in thin liquid films. In the VOF model, a multiphase flow interface tracking approach, the full continuity, Navier Stokes, energy, and volume fraction equations were solved. This also enables investigating more complex thin-film problems with multi-component films. The numerical approach presented in this study surpasses the long-wave limit inherent in the TF and LS models. It successfully predicts different interface deformation stages, including the initial linear and the late nonlinear deformation. Compared to the experimental data [19], the VOF model predicted characteristic wavelength (λ) with significantly higher accuracy compared to the TF model and LS analysis. Several cases with different polymer thicknesses, gap spacing, and temperature differences were investigated to correlate the characteristic wavelength predicted by the VOF model and TF model theoretically found by the LS formulation. The variation of the characteristic wavelength predicted by the VOF, TF model, and LS analysis with the increase of inverse filling ratio were studied. It was found that the characteristic wavelength predicted by the LS analysis (λ_{LS}) increased sharply for small \tilde{d}_2 up to a maximum at $\tilde{d}_2 = 2.44$. The same trends were observed for the characteristic wavelength obtained from the VOF and TC models; however, the maximum point was located at $\tilde{d}_2 = 2.5$. It is worth noting that the Marangoni and Capillary inverse numbers increase as the inverse filling ratio increases. All the characteristic wavelengths from LS analysis, TF model, and VOF simulation decreased with an increase in the applied thermal gradient.

The size and periodicity of the protrusions need to be tailored to avoid secondary pillar formations when using plates with protrusions to generate the non-uniform thermal gradient and enable forming well-ordered patterns. Thus, the effect of localized cooling/heating was also investigated by using a patterned top cold plate. Results showed that the interface deformation and pillar formation are sensitive to the localized cooled area (w , under the protrusions). It leads to the transition from single to twin pillars for both VOF and TF models. However, the magnitude of normalized width of the protrusions (\tilde{w}) for making two twin pillars in the TF model is higher than that of the VOF approach. The deformation of the interface was studied at the early, later, and final stages of pattern formation at different widths of the protrusion in the VOF model. The results showed that the case with $\tilde{w} < 0.34$ leads to the formation of only one pillar under the protrusion, the case with $\tilde{w} = 0.52$ result in the formation of two separate pillars. Regarding the effect of separation distance (\tilde{l}_p) on the TC-induced patterning process, it was found when $\tilde{l}_p < 0.8$, no secondary pillars formed between two protrusions, while when $\tilde{l}_p = 1.4$, a secondary pillar was observed. A similar trend was observed in the TF model; however, the magnitude of the width of protrusions and the separation distance must be greater than that of the VOF model to form an additional pillar. Finally, the 2D maps for both VOF and TF model are also generated based on the normalized width of the protrusions (\tilde{w}) and their separation distance (\tilde{l}_p) and the inverse filling ratio to predict the threshold values in which the transition from single- to two-pillar formation occurred and secondary pillar formed.

The polymer film in the first and second parts of the thesis is assumed to behave as a Newtonian fluid. In contrast, many polymer solutions and molten polymers are non-Newtonian fluids. Hence, the last part of this study focuses on a power-law model for the TC patterning of polymer films showing shear-thickening/ thinning behaviors. This enables overcoming the limitation associated with assuming that viscosity is independent of shear rate. We have investigated the nonlinear interface deformations in shear-thinning and shear-thickening confined fluid films under transverse thermal gradient. Lubrication theory and the power-law model are employed to derive a fourth-order nonlinear thin film equation, which describes the spatiotemporal evolution of the polymer-air interface and the local viscosity variation. The thin-film equation is parametrized by the system's physical properties, such as the interfacial tension, temperature difference, the viscosity, thermal conductivity of polymer and air, and flow behavior index. The finite difference with pseudo-staggered discretization and an adaptive time step is used to solve the nonlinear thin film

equation. Linear stability (LS) analysis is then applied to find the characteristic wavelength for the growth of instabilities. The results show that the growth rate of instabilities and the time takes the first pillar touches the top substrate is strongly affected by the power-law index and is relatively longer for shear-thinning ($\tilde{\tau} = 0.49$) than shear thickening ($\tilde{\tau} = 0.17$). The effect of local variation in viscosity on the dynamics and morphology of the interface is also studied. In the shear-thinning fluid film, the pillars are formed where the viscosity experiences its minimum value. In contrast, the pillars' location in a shear thickening case is the same spot that the viscosity reached its maximum value. The compactness and fidelity of the formed columnar structures have been investigated considering different filling ratios. It was found that the pillar density (number of pillars form in $1\mu m^2$ area) has improved as the fluid behavior index increased. An increase in the filling ratio \tilde{d} leads to smaller and more stable structures in both shear thinning and shear thickening fluid films. As a contribution to science, for the first time in this thesis, the full Navier Stokes equations without LW approximation coupled with the interface tracking methods were solved. The characteristic wavelength from different approaches including VOF, Phase field, and thin film were compared and a correlation was derived. Insights into fabrication of well-ordered nanostructures based on an interplay between the height and width of protrusions, as well as the pattern of plate periodicity and initial thickness were provided. It can be used as a preliminary choice for fabricating patterned masks. Finally, a new model for TC patterning of non-Newtonian power law fluids was developed.

6.2. Future work

Further studies that can be done as a continuation of the present study are listed as follows:

- The dependence of viscosity on the temperature can be studied in the VOF and phase-field models. Moreover, changing the geometry from 2D to 3D can affect the final shape and size of the formed features since they can interact with each other at the later stage of the pattern formation.
- The effect of thermal evaporation can also be considered on the TC-induced patterning system. This could be done by adding the thermal evaporation term to the thin film equation. It will be more practical for heated molten polymer when the solvent evaporation happens during the evolution process in the TC process.

- The TC-induced patterning of bilayer systems can be studied. Both thermocapillary modes (long-wave and short-range instability) can be significantly affected by the relative viscosity of film and bounding layer.
- The combination of TC and EHD as two self-organized patterning methods can be investigated. Temperature gradient and electrostatic force can be both applied across the liquid film and the effect of this combined phenomenon on the characteristic wavelength of the formed pillars can be studied.

References

- [1] D. Quéré, FLUID COATING ON A FIBER, *Annu. Rev. Fluid Mech.* 31 (1999) 347–384. doi:10.1146/annurev.fluid.31.1.347.
- [2] S.P. Lin, H. Brenner, Marangoni convection in a tear film, *J. Colloid Interface Sci.* 85 (1982) 59–65. doi:10.1016/0021-9797(82)90235-1.
- [3] O.A. Kabov, E.Y. Gatapova, D. V. Zaitsev, Cooling technique based on evaporation of thin and ultra thin liquid films, in: 2008 11th IEEE Intersoc. Conf. Therm. Thermomechanical Phenom. Electron. Syst. I-THERM, 2008: pp. 520–527. doi:10.1109/ITHERM.2008.4544312.
- [4] A. Sharma, Relationship of Thin Film Stability and Morphology to Macroscopic Parameters of Wetting in the Apolar and Polar Systems, *Langmuir.* 9 (1993) 861–869. doi:10.1021/la00027a042.
- [5] A. Sharma, R. Khanna, Pattern formation in unstable thin liquid films under the influence of antagonistic short- and long-range forces, *J. Chem. Phys.* 110 (1999) 4929–4936. doi:10.1063/1.478378.
- [6] D.Y.C. Chan, E. Klaseboer, R. Manica, Film drainage and coalescence between deformable drops and bubbles, *Soft Matter.* 7 (2011) 2235–2264. doi:10.1039/c0sm00812e.
- [7] J.S. Eow, M. Ghadiri, Electrostatic enhancement of coalescence of water droplets in oil: A review of the technology, *Chem. Eng. J.* 85 (2002) 357–368. doi:10.1016/S1385-8947(01)00250-9.
- [8] F. Mostowfi, K. Khristov, J. Czarnecki, J. Masliyah, S. Bhattacharjee, Electric field mediated breakdown of thin liquid films separating microscopic emulsion droplets, *Appl. Phys. Lett.* 90 (2007) 184102. doi:10.1063/1.2735550.
- [9] A. Vrij, Possible mechanism for the spontaneous rupture of thin, free liquid films, *Discuss. Faraday Soc.* 42 (1966) 23–33. doi:10.1039/DF9664200023.
- [10] A. Sheludko, Thin liquid films, *Adv. Colloid Interface Sci.* 1 (1967) 391–464.

doi:10.1016/0001-8686(67)85001-2.

- [11] E. Ruckenstein, R.K. Jain, Spontaneous rupture of thin liquid films, *J. Chem. Soc. Faraday Trans. 2 Mol. Chem. Phys.* 70 (1974) 132–147. doi:10.1039/F29747000132.
- [12] M.B. Williams, S.H. Davis, Nonlinear theory of film rupture, *J. Colloid Interface Sci.* 90 (1982) 220–228. doi:10.1016/0021-9797(82)90415-5.
- [13] A. Oron, S.H. Davis, S.G. Bankoff, Long-scale evolution of thin liquid films, *Rev. Mod. Phys.* 69 (1997) 931–980. doi:10.1103/revmodphys.69.931.
- [14] A. Ghatak, R. Khanna, A. Sharma, Dynamics and morphology of holes in dewetting of thin films, *J. Colloid Interface Sci.* 212 (1999) 483–494. doi:10.1006/jcis.1998.6052.
- [15] A. Sharma, E. Ruckenstein, An analytical nonlinear theory of thin film rupture and its application to wetting films, *J. Colloid Interface Sci.* 113 (1986) 456–479. doi:10.1016/0021-9797(86)90181-5.
- [16] V.S. Mitlin, Dewetting of solid surface: Analogy with spinodal decomposition, *J. Colloid Interface Sci.* 156 (1993) 491–497. doi:10.1006/jcis.1993.1142.
- [17] E. Schäffer, S. Harkema, M. Roerdink, R. Blossey, U. Steiner, Thermomechanical Lithography: Pattern Replication Using a Temperature Gradient Driven Instability, *Adv. Mater.* 15 (2003) 514–517. doi:10.1002/adma.200390119.
- [18] M. Dietzel, S.M. Troian, *Thermocapillary Patterning of Nanoscale Polymer Films*, Cambridge University Press, 2009. doi:10.1557/PROC-1179-BB08-02.
- [19] M. Dietzel, S.M. Troian, Mechanism for spontaneous growth of nanopillar arrays in ultrathin films subject to a thermal gradient, *J. Appl. Phys.* 108 (2010) 074308. doi:10.1063/1.3475516.
- [20] H. Nazaripoor, C.R. Koch, M. Sadrzadeh, Enhanced Electrically Induced Micropatterning of Confined Thin Liquid Films: Thermocapillary Role and Its Limitations, 56 (2017). doi:10.1021/acs.iecr.7b02814.
- [21] A. Riad, H. Nazaripoor, A. Mohammadtabar, M. Sadrzadeh, Electrohydrodynamic Patterning of non-Newtonian Thin Films, *APS.* (2019) Q34.004.

- <https://ui.adsabs.harvard.edu/abs/2019APS..DFDQ34004R/abstract> (accessed March 5, 2021).
- [22] H. Nazaripoor, C.R. Koch, M. Sadrzadeh, S. Bhattacharjee, Electrohydrodynamic patterning of ultra-thin ionic liquid films, *Soft Matter*. 11 (2015) 2193–2202. doi:10.1039/c4sm02477j.
- [23] H. Nazaripoor, C.R. Koch, S. Bhattacharjee, Electrical Perturbations of Ultrathin Bilayers: Role of Ionic Conductive Layer, *Langmuir*. 30 (2014) 14734–14744. doi:10.1021/la503839x.
- [24] J. Israelachvili, *Intermolecular and Surface Forces*, Elsevier Inc., 2011. doi:10.1016/C2009-0-21560-1.
- [25] Jacob H. Masliyah and Subir Bhattacharjee, *Electrokinetic and Colloid Transport Phenomena*, Wiley, 2008. doi:10.1002/cjce.5450840612.
- [26] G.G. Reiter, Dewetting of thin polymer films, *Phys. Rev. Lett.* 68 (1992) 75–78. doi:10.1103/PhysRevLett.68.75.
- [27] A. Sharma, G. Gu, G. Reiter, *Instability of Thin Polymer Films on Coated Substrates: Rupture, Dewetting, and Drop Formation*, 1996.
- [28] G. Reiter, Unstable Thin Polymer Films: Rupture and Dewetting Processes, *Langmuir*. 9 (1993) 1344–1351. doi:10.1021/la00029a031.
- [29] K. Jacobs, R. Seemann, S. Herminghaus, Stability and Dewetting of Thin Liquid Films, in: 2008: pp. 243–265. doi:10.1142/9789812818829_0010.
- [30] K.A. Barnes, A. Karim, J.F. Douglas, A.I. Nakatani, H. Gruell, E.J. Amis, Suppression of Dewetting in Nanoparticle-Filled Polymer Films, (n.d.). doi:10.1021/ma990614s.
- [31] D. Gentili, G. Foschi, F. Valle, M. Cavallini, F. Biscarini, Applications of dewetting in micro and nanotechnology, *Chem. Soc. Rev.* 41 (2012) 4430–4443. doi:10.1039/c2cs35040h.
- [32] D. Peschka, S. Haefner, L. Marquant, K. Jacobs, A. Münch, B. Wagner, Signatures of slip in dewetting polymer films, *Proc. Natl. Acad. Sci. U. S. A.* 116 (2019) 9275–9284.

- doi:10.1073/pnas.1820487116.
- [33] U. Thiele, M. Mertig, W. Pompe, Dewetting of an Evaporating Thin Liquid Film: Heterogeneous Nucleation and Surface Instability, *Phys. Rev. Lett.* 80 (1998) 2869–2872. doi:10.1103/PhysRevLett.80.2869.
- [34] J. Singh, A. Sharma, Self-organization in unstable thin liquid films: Dynamics and patterns in systems displaying a secondary minimum, *J. Adhes. Sci. Technol.* 14 (2000) 145–166. doi:10.1163/156856100742519.
- [35] D. Bonn, J. Eggers, J. Indekeu, J. Meunier, E. Rolley, Wetting and spreading, *Rev. Mod. Phys.* 81 (2009) 739–805. doi:10.1103/RevModPhys.81.739.
- [36] D.T. Wasan, A.D. Nikolov, L.A. Lobo, K. Koczo, D.A. Edwards, Foams, thin films and surface rheological properties, *Prog. Surf. Sci.* 39 (1992) 119–154. doi:10.1016/0079-6816(92)90021-9.
- [37] E. Chatzigiannakis, P. Veenstra, B. Dick Ten Bosch, J. Vermant, Mimicking coalescence using a pressure-controlled dynamic thin film balance †, *Cite This Soft Matter.* 16 (2020) 9410. doi:10.1039/d0sm00784f.
- [38] *Characterization of Food*, Elsevier, 1995. doi:10.1016/b978-0-444-81499-9.x5000-8.
- [39] M.M. Abdulredha, H. Siti Aslina, C.A. Luqman, Overview on petroleum emulsions, formation, influence and demulsification treatment techniques, *Arab. J. Chem.* 13 (2020) 3403–3428. doi:10.1016/j.arabjc.2018.11.014.
- [40] C.-Y. Lin, J.C. Slattery, Thinning of a liquid film as a small drop or bubble approaches a fluid–fluid interface, *AIChE J.* 28 (1982) 786–792. doi:10.1002/aic.690280513.
- [41] S.I. Karakashev, D.S. Ivanova, Thin liquid film drainage: Ionic vs. non-ionic surfactants, *J. Colloid Interface Sci.* 343 (2010) 584–593. doi:10.1016/j.jcis.2009.11.065.
- [42] S.I. Karakashev, E.D. Manev, Hydrodynamics of thin liquid films: Retrospective and perspectives, *Adv. Colloid Interface Sci.* 222 (2015) 398–412. doi:10.1016/j.cis.2014.07.010.
- [43] K. Ziemelis, The future of microelectronics, *Nat.* 2000 4066799. (n.d.).

- <https://www.nature.com/articles/35023221> (accessed March 14, 2021).
- [44] M. Wilson, The future of telemedicine, *Stud. Health Technol. Inform.* 80 (2002) 129–136. doi:10.3233/978-1-60750-924-0-129.
- [45] I. Nejati, M. Dietzel, S. Hardt, Exploiting cellular convection in a thick liquid layer to pattern a thin polymer film, *Cit. Appl. Phys. Lett.* 108 (2016) 51604. doi:10.1063/1.4940366.
- [46] L. Peng, Y. Deng, P. Yi, X. Lai, Micro hot embossing of thermoplastic polymers: a review, *J. Micromechanics Microengineering.* 24 (2014) 013001. doi:10.1088/0960-1317/24/1/013001.
- [47] H. Sirringhaus, T. Kawase, R.H. Friend, T. Shimoda, M. Inbasekaran, W. Wu, E.P. Woo, High-resolution inkjet printing of all-polymer transistor circuits., *Science.* 290 (2000) 2123–6. <http://www.ncbi.nlm.nih.gov/pubmed/11118142> (accessed November 26, 2018).
- [48] T.R. Hebner, C.C. Wu, D. Marcy, M.H. Lu, J.C. Sturm, Ink-jet printing of doped polymers for organic light emitting devices, 1998. doi:10.1063/1.120807.
- [49] J. Kim, H. Oh, S.S. Kim, Electrohydrodynamic drop-on-demand patterning in pulsed cone-jet mode at various frequencies, *Aerosol Sci.* 39 (2008) 819–825. doi:10.1016/j.jaerosci.2008.05.001.
- [50] S.Y. Chou, L. Zhuang, L. Guo, Lithographically induced self-construction of polymer microstructures for resistless patterning, *Appl. Phys. Lett.* 75 (1999) 1004. doi:10.1063/1.124579.
- [51] E. McLeod, Y. Liu, S.M. Troian, Experimental Verification of the Formation Mechanism for Pillar Arrays in Nanofilms Subject to Large Thermal Gradients, *Phys. Rev. Lett.* 106 (2011) 175501. doi:10.1103/PhysRevLett.106.175501.
- [52] J.-H. Lee, J.P. Singer, E.L. Thomas, Micro-/Nanostructured Mechanical Metamaterials, *Adv. Mater.* 24 (2012) 4782–4810. doi:10.1002/adma.201201644.
- [53] P. Van Der Asdonk, P.H.J. Kouwer, Liquid crystal templating as an approach to spatially and temporally organise soft matter, *Chem. Soc. Rev.* 46 (2017) 5935–5949.

doi:10.1039/c7cs00029d.

- [54] R.A. Segalman, Patterning with block copolymer thin films, *Mater. Sci. Eng. R Reports*. 48 (2005) 191–226.
- [55] H. Ebrahimnejad, G.A. Sawatzky, M. Berciu, Differences between the insulating limit quasiparticles of one-band and three-band cuprate models, *J. Phys. Condens. Matter*. 28 (2016). doi:10.1088/0953-8984/28/10/105603.
- [56] J. Zhu, M.C. Hersam, Assembly and Electronic Applications of Colloidal Nanomaterials, *Adv. Mater.* 29 (2017) 1603895. doi:10.1002/adma.201603895.
- [57] N. Wu, W.B. Russel, Micro- and nano-patterns created via electrohydrodynamic instabilities, *Nano Today*. 4 (2009) 180–192. doi:10.1016/J.NANTOD.2009.02.002.
- [58] H. Nazaripoor, C.R. Koch, M. Sadrzadeh, Ordered high aspect ratio nanopillar formation based on electrical and thermal reflowing of prepatterned thin films, *J. Colloid Interface Sci.* 530 (2018) 312–320. doi:10.1016/J.JCIS.2018.06.080.
- [59] R. Mukherjee, A. Sharma, Instability, self-organization and pattern formation in thin soft films, *Soft Matter*. 11 (2015) 8717–8740. doi:10.1039/C5SM01724F.
- [60] J.P. Singer, Thermocapillary approaches to the deliberate patterning of polymers, *J. Polym. Sci. Part B Polym. Phys.* 55 (2017) 1649–1668. doi:10.1002/polb.24298.
- [61] E. Albisetti, D. Petti, M. Pancaldi, M. Madami, S. Tacchi, J. Curtis, W.P. King, A. Papp, G. Csaba, W. Porod, P. Vavassori, E. Riedo, R. Bertacco, Nanopatterning reconfigurable magnetic landscapes via thermally assisted scanning probe lithography, *Nat. Nanotechnol.* 11 (2016) 545–551. doi:10.1038/nnano.2016.25.
- [62] H. Nazaripoor, C.R. Koch, M. Sadrzadeh, S. Bhattacharjee, Thermo-Electrohydrodynamic Patterning in Nanofilms, *Langmuir*. 32 (2016) 5776–5786. doi:10.1021/acs.langmuir.6b01810.
- [63] S.Y. Chou, L. Zhuang, Lithographically induced self-assembly of periodic polymer micropillar arrays, *J. Vac. Sci. Technol. B Microelectron. Nanom. Struct. Process. Meas. Phenom.* 17 (1999) 3197. doi:10.1116/1.590979.

- [64] K.R. Fiedler, *Fundamentals of Thermocapillary Sculpting of Liquid Nanofilms and Applications to Thin Film Micro-Optics*, 2017.
- [65] E. Schäffer, S. Harkema, M. Roerdink, R. Blossey, U. Steiner, Morphological instability of a confined polymer film in a thermal gradient, *Macromolecules*. 36 (2003) 1645–1655. doi:10.1021/ma021080p.
- [66] E. Schäffer, S. Harkema, R. Blossey, U. Steiner, Temperature-gradient-induced instability in polymer films, *Europhys. Lett.* 60 (2002) 255–261. doi:10.1209/epl/i2002-00344-9.
- [67] E.S. Schäffer, *Instabilities in Thin Polymer Films: Structure Formation and Pattern Transfer*, 2001.
- [68] M. Salari, M. Mohammadtabar, A. Mohammadtabar, Numerical solutions to heat transfer of nanofluid flow over stretching sheet subjected to variations of nanoparticle volume fraction and wall temperature, *Appl. Math. Mech. (English Ed.)* 35 (2014) 63–72. doi:10.1007/s10483-014-1772-8.
- [69] M. Salari, A. Rezvani, A. Mohammadtabar, M. Mohammadtabar, Numerical study of entropy generation for natural convection in rectangular cavity with circular corners, *Heat Transf. Eng.* 36 (2014) 186–199. doi:10.1080/01457632.2014.909221.
- [70] M. Salari, A. Mohammadtabar, M. Mohammadtabar, Effects of circular corners and aspect-ratio on entropy generation due to natural convection of nanofluid flows in rectangular cavities, *Therm. Sci.* 19 (2015) 1621–1632. doi:10.2298/TSCI130201034S.
- [71] M. Salari, A. Mohammadtabar, Mohammad Mohammadtabar, H. Ahmadi Danesh, M.M. Tabar, A.M. Tabar, H.A. Danesh, Mixed Convection of Nanofluid Flows in a Square Lid-Driven Cavity Heated Partially From Both the Bottom and Side Walls, *Numeical Heat Transf. PartA.* 62 (2012) 37–41. doi:10.1080/10407782.2012.691055.
- [72] J.R.A. Pearson, On convection cells induced by surface tension, *J. Fluid Mech.* 4 (1958) 489. doi:10.1017/S0022112058000616.
- [73] E.L. Koschmieder, M.I. Biggerstaff, Onset of surface-tension-driven Bénard convection, *J. Fluid Mech.* 167 (1986) 49. doi:10.1017/S0022112086002720.

- [74] S.H. Davis, Thermocapillary Instabilities, *Annu. Rev. Fluid Mech.* 19 (1987) 403–435. doi:10.1146/annurev.fl.19.010187.002155.
- [75] P. (Pierre) Colinet, J.C. (Jean C. Legros, M.G. (Manuel G. Velarde, John Wiley & Sons., Nonlinear dynamics of surface-tension-driven instabilities, Wiley-VCH, 2001.
- [76] T. Gambaryan-Roisman, Modulation of Marangoni convection in liquid films., *Adv. Colloid Interface Sci.* 222 (2015) 319–31. doi:10.1016/j.cis.2015.02.003.
- [77] M.F. Schatz, S.J. Vanhook, W.D. McCormick, J.B. Swift, H.L. Swinney, Onset of surface-tension-driven Bénard convection, *Phys. Rev. Lett.* 75 (1995) 1938–1941. doi:10.1103/PhysRevLett.75.1938.
- [78] S. Rahal, P. Cerisier, H. Azuma, Bénard-Marangoni convection in a small circular container: Influence of the Biot and Prandtl numbers on pattern dynamics and free surface deformation, *Exp. Fluids.* 43 (2007) 547–554. doi:10.1007/s00348-007-0323-1.
- [79] K.C. Mills, B.J. Keene, Factors affecting variable weld penetration, *Int. Mater. Rev.* 35 (1990) 185–216. doi:10.1179/095066090790323966.
- [80] D.T.J. Hurle, Surface aspects of crystal growth from the melt, *Adv. Colloid Interface Sci.* 15 (1981) 101–130. doi:10.1016/0001-8686(81)80005-X.
- [81] A. Oprisan, J.J. Hegseth, G.M. Smith, C. Lecoutre, Y. Garrabos, D.A. Beysens, Dynamics of a wetting layer and Marangoni convection in microgravity, *Phys. Rev. E - Stat. Nonlinear, Soft Matter Phys.* 84 (2011). doi:10.1103/PhysRevE.84.021202.
- [82] S.J. VanHook, M.F. Schatz, W.D. McCormick, J.B. Swift, H.L. Swinney, Long-wavelength instability in surface-tension-driven Bénard convection, *Phys. Rev. Lett.* 75 (1995) 4397–4400. doi:10.1103/PhysRevLett.75.4397.
- [83] P. Deshpande, X. Sun, S.Y. Chou, Observation of dynamic behavior of lithographically induced self-assembly of supramolecular periodic pillar arrays in a homopolymer film, *Appl. Phys. Lett.* 79 (2001). doi:10.1063/1.1398616.
- [84] H. Nazari-poor, M.R. Flynn, C.R. Koch, M. Sadrzadeh, Thermally induced interfacial instabilities and pattern formation in confined liquid nanofilms, *Phys. Rev. E.* 98 (2018)

043106. doi:10.1103/PhysRevE.98.043106.
- [85] H. Annepu, J. Sarkar, S. Basu -, B. Li, Y. Li, G.-K. Xu, al -, Z. Yu-Nong, H. Gan-Yun -, Interfacial slippage effect on the surface instability of a thin elastic film, *J. Phys. D Appl. Phys. To.* 42 (2009) 55302. doi:10.1088/0022-3727/42/5/055302.
- [86] F. Song, D. Ju, F. Gu, Y. Liu, Y. Ji, Y. Ren, X. He, B. Sha, B.Q. Li, Q. Yang, Parametric Study on Electric Field-Induced Micro-/Nanopatterns in Thin Polymer Films, *Langmuir.* 34 (2018) 4188–4198. doi:10.1021/acs.langmuir.8b00007.
- [87] D. Kim, W. Lu, Three-dimensional model of electrostatically induced pattern formation in thin polymer films, *Phys. Rev. B - Condens. Matter Mater. Phys.* 73 (2006) 035206. doi:10.1103/PhysRevB.73.035206.
- [88] H. Tian, J. Shao, Y. Ding, X. Li, H. Liu, Simulation of polymer rheology in an electrically induced micro- or nano-structuring process based on electrohydrodynamics and conservative level set method, *RSC Adv.* 4 (2014) 21672. doi:10.1039/c4ra00553h.
- [89] J.S. Rowlinson, Translation of J. D. van der Waals' The thermodynamik theory of capillarity under the hypothesis of a continuous variation of density, *J. Stat. Phys.* 20 (1979) 197–200. doi:10.1007/BF01011513.
- [90] J.W. Cahn, J.E. Hilliard, Free Energy of a Nonuniform System. I. Interfacial Free Energy, *J. Chem. Phys.* 28 (1958) 258–267. doi:10.1063/1.1744102.
- [91] P. GAO, J.J. FENG, Spreading and breakup of a compound drop on a partially wetting substrate, *J. Fluid Mech.* 682 (2011) 415–433. doi:10.1017/jfm.2011.235.
- [92] V. V. KHATAVKAR, P.D. ANDERSON, P.C. DUINEVELD, H.E.H. MEIJER, Diffuse-interface modelling of droplet impact, *J. Fluid Mech.* 581 (2007) 97. doi:10.1017/S002211200700554X.
- [93] V. V. KHATAVKAR, P.D. ANDERSON, H.E.H. MEIJER, Capillary spreading of a droplet in the partially wetting regime using a diffuse-interface model, *J. Fluid Mech.* 572 (2007) 367. doi:10.1017/S0022112006003533.
- [94] Y. Lin, P. Skjetne, A. Carlson, A phase field model for multiphase electro-hydrodynamic

- flow, *Int. J. Multiph. Flow.* 45 (2012) 1–11.
doi:10.1016/J.IJMULTIPHASEFLOW.2012.04.002.
- [95] Q. Yang, B.Q. Li, Y. Ding, 3D phase field modeling of electrohydrodynamic multiphase flows, *Int. J. Multiph. Flow.* 57 (2013) 1–9.
doi:10.1016/J.IJMULTIPHASEFLOW.2013.06.006.
- [96] A. Mohammadtabar, H. Nazariipoor, A. Riad, A. Hemmati, M. Sadrzadeh, A numerical study for thermocapillary induced patterning of thin liquid films, *Phys. Fluids.* 32 (2020) 024106. doi:10.1063/1.5134460.
- [97] Y. Alhendal, A. Turan, P. Hollingsworth, Thermocapillary simulation of single bubble dynamics in zero gravity, *Acta Astronaut.* 88 (2013) 108–115.
doi:10.1016/J.ACTAASTRO.2013.03.017.
- [98] Y. Alhendal, A. Turan, A. Kalendar, Thermocapillary migration of an isolated droplet and interaction of two droplets in zero gravity, 2016. doi:10.1016/j.actaastro.2016.05.001.
- [99] A. Tomiyama, A. Sou, H. Minagawa, T. Sakaguchi, Numerical Analysis of a Single Bubble by VOF Method., *JSME Int. J. Ser. B.* 36 (1993) 51–56. doi:10.1299/jsmeb.36.51.
- [100] M. Kawaji, J.M. DeJesus, G. Tudose, Investigation of flow structures in vertical slug flow, *Nucl. Eng. Des.* 175 (1997) 37–48. doi:10.1016/S0029-5493(97)00160-X.
- [101] C.G. Willson, R.R. Dammel, A. Reiser, Photoresist materials: a historical perspective, in: R.G. Tarascon-Auriol (Ed.), *International Society for Optics and Photonics*, 1997: p. 28. doi:10.1117/12.275826.
- [102] H. Bénard, H.B. Étude, Étude expérimentale des courants de convection dans une nappe liquide.-Régime permanent : tourbillons cellulaires, *J. Phys. Theor. Appl.* 9 (1900) 513–524. doi:10.1051/jphystap:019000090051300.
- [103] A. Oron, P. Rosenau, On a nonlinear thermocapillary effect in thin liquid layers, *J. Fluid Mech.* 273 (1994) 361. doi:10.1017/S0022112094001977.
- [104] E. Schäffer, T. Thurn-Albrecht, T.P. Russell, U. Steiner, Electrically induced structure formation and pattern transfer, *Nature.* 403 (2000) 874–877. doi:10.1038/35002540.

- [105] J. Cahn, S. Allen, J.W. Cahn, S.M. Allen, A MICROSCOPIC THEORY FOR DOMAIN WALL MOTION AND ITS EXPERIMENTAL VERIFICATION IN Fe-AI ALLOY DOMAIN GROWTH KINETICS A MICROSCOPIC THEORY FOR DOMAIN WALL MOTION AND ITS EXPERIMENTAL VERIFICATION IN Fe-AI ALLOY DOMAIN GROWTH KINETICS, *J. Phys. Colloq.* 38 (1977). doi:10.1051/jphyscol:1977709i.
- [106] D. JACQMIN, Contact-line dynamics of a diffuse fluid interface, *J. Fluid Mech.* 402 (2000) S0022112099006874. doi:10.1017/S0022112099006874.
- [107] G. Karapetsas, N.T. Chamakos, A.G. Papathanasiou, Thermocapillary Droplet Actuation: Effect of Solid Structure and Wettability, *Langmuir.* 33 (2017). doi:10.1021/acs.langmuir.7b02762.
- [108] Q. Yang, B.Q. Li, Z. Zhao, J. Shao, F. Xu, Numerical analysis of the Rayleigh–Taylor instability in an electric field, *J. Fluid Mech.* 792 (2016) 397–434. doi:10.1017/jfm.2016.54.
- [109] H. Tian, J. Shao, Y. Ding, X. Li, H. Hu, Electrohydrodynamic Micro-/Nanostructuring Processes Based on Prepatterned Polymer and Prepatterned Template, (2014). doi:10.1021/ma402456u.
- [110] E. Schäffer, T. Thurn-Albrecht, T.P. Russell, U. Steiner, Electrohydrodynamic instabilities in polymer films, *Europhys. Lett.* 53 (2001) 518–524. doi:10.1209/epl/i2001-00183-2.
- [111] Z. Lin, T. Kerle, S.M. Baker, D.A. Hoagland, E. Schärfer, U. Steiner, T.P. Russell, Electric field induced instabilities at liquid/liquid interfaces, *J. Chem. Phys.* 114 (2001) 2377–2381. doi:10.1063/1.1338125.
- [112] K.R. Fiedler, S.M. Troian, Early time instability in nanofilms exposed to a large transverse thermal gradient: Improved image and thermal analysis, *J. Appl. Phys.* 120 (2016) 205303. doi:10.1063/1.4968575.
- [113] T. Young, An Essay on the Cohesion of Fluids., *Proc. R. Soc. London.* 1 (1800) 171–172. doi:10.1098/rspl.1800.0095.
- [114] G.M. Wallraff, W.D. Hinsberg, Lithographic Imaging Techniques for the Formation of Nanoscopic Features, *Chem. Rev.* 99 (1999) 1801–1821. doi:10.1021/cr980003i.

- [115] B.D. Gates, Q. Xu, M. Stewart, D. Ryan, C.G. Willson, G.M. Whitesides, New approaches to nanofabrication: Molding, printing, and other techniques, *Chem. Rev.* 105 (2005) 1171–1196. doi:10.1021/cr030076o.
- [116] W. Huang, X. Yu, Y. Liu, W. Qiao, L. Chen, A review of the scalable nano-manufacturing technology for flexible devices, *Front. Mech. Eng.* 12 (2017) 99–109. doi:10.1007/s11465-017-0416-3.
- [117] J. Rodríguez-Hernández, Wrinkled interfaces: Taking advantage of surface instabilities to pattern polymer surfaces, *Prog. Polym. Sci.* 42 (2015) 1–41. doi:10.1016/j.progpolymsci.2014.07.008.
- [118] A. Muñoz-Bonilla, M. Fernández-García, J. Rodríguez-Hernández, Towards hierarchically ordered functional porous polymeric surfaces prepared by the breath figures approach, *Prog. Polym. Sci.* 39 (2014) 510–554. doi:10.1016/j.progpolymsci.2013.08.006.
- [119] P. Gambhire, R.M. Thaokar, Role of conductivity in the electrohydrodynamic patterning of air-liquid interfaces, *Phys. Rev. E.* 86 (2012) 36301. doi:10.1103/PhysRevE.86.036301.
- [120] J. Sarkar, A. Sharma, V.B. Shenoy, Electric-field induced instabilities and morphological phase transitions in soft elastic films, *Phys. Rev. E.* 77 (2008) 031604. doi:10.1103/PhysRevE.77.031604.
- [121] J.M. Davis, S.M. Troian, Influence of attractive van der Waals interactions on the optimal excitations in thermocapillary-driven spreading, *Phys. Rev. E - Stat. Physics, Plasmas, Fluids, Relat. Interdiscip. Top.* 67 (2003) 9. doi:10.1103/PhysRevE.67.016308.
- [122] F.B. Wyart, J. Dailant, Drying of solids wetted by thin liquid films, *Can. J. Phys.* 68 (1990) 1084–1088. doi:10.1139/p90-151.
- [123] Y. Chao, Z. Ding, Thermocapillary thin-film flows on a compliant substrate, *Phys. Rev. E.* 99 (2019). doi:10.1103/PhysRevE.99.043101.
- [124] V. Frumkin, A. Oron, Thermocapillary flow of a thin liquid film in a confined two-layer system under a hydrophobic plate, *Phys. Rev. FLUIDS.* 2 (2017) 104002. doi:10.1103/PhysRevFluids.2.104002.

- [125] R. Verma, A. Sharma, I. Banerjee, K. Kargupta, Spinodal instability and pattern formation in thin liquid films confined between two plates, *J. Colloid Interface Sci.* 296 (2006) 220–232. doi:10.1016/j.jcis.2005.08.025.
- [126] D.T. Conroy, L. Espín, O.K. Matar, S. Kumar, Thermocapillary and electrohydrodynamic effects on the stability of dynamic contact lines, *Phys. Rev. Fluids.* 4 (2019) 34001. doi:10.1103/PhysRevFluids.4.034001.
- [127] H. Nazariipoor, C.R. Koch, M. Sadrzadeh, S. Bhattacharjee, Compact micro/nano electrohydrodynamic patterning: Using a thin conductive film and a patterned template, *Soft Matter.* 12 (2016) 1074–1084. doi:10.1039/c5sm02258d.
- [128] J.B. Bostwick, J.A. Dijksman, M. Shearer, Wetting dynamics of a collapsing fluid hole, *Phys. Rev. FLUIDS.* 2 (2017) 14006. doi:10.1103/PhysRevFluids.2.014006.
- [129] *Electrodynamics of Continuous Media* : L.D. Landau & E.M. Lifshitz : Free Download, Borrow, and Streaming : Internet Archive, (n.d.).
<https://archive.org/details/ElectrodynamicsOfContinuousMedia/mode/2up> (accessed February 4, 2020).
- [130] B.J. Kim, K.D. Kim, Rayleigh-Taylor instability of viscous fluids with phase change, *Phys. Rev. E.* 93 (2016). doi:10.1103/PhysRevE.93.043123.
- [131] R. Sarma, P.K. Mondal, Marangoni instability in a heated viscoelastic liquid film: Long-wave versus short-wave perturbations, *Phys. Rev. E.* 100 (2019) 13103. doi:10.1103/PhysRevE.100.013103.
- [132] E. Lim, Y.M. Hung, Long-wave evolution model of thermocapillary convection in an evaporating thin film of pseudoplastic fluids, *Int. J. Numer. Methods Heat Fluid Flow.* 29 (2019) 4764–4787. doi:10.1108/HFF-01-2019-0003.
- [133] A.A. Avramenko, I. V. Shevchuk, S. Harmand, A.I. Tyrinov, Thermocapillary instability in an evaporating two-dimensional thin layer film, *Int. J. Heat Mass Transf.* 91 (2015) 77–88. doi:10.1016/j.ijheatmasstransfer.2015.07.063.
- [134] E.A. Chinnov, E.N. Shatskiy, V. V. Semionov, Effect of thermocapillary instability on liquid film breakdown, *Int. J. Heat Mass Transf.* 145 (2019) 118692.

doi:10.1016/j.ijheatmasstransfer.2019.118692.

- [135] S.J. Vanhook, M.F. Schatz, J.B. Swift, W.D. McCormick, H.L. Swinney, Long-wavelength surface-tension-driven Bénard convection: experiment and theory, *J. Fluid Mech.* 345 (1997) 45–78. doi:10.1017/S0022112097006101.
- [136] A.C. Or, R.E. Kelly, L. Cortelezzi, J.L. Speyer, Control of long-wavelength Marangoni-Bénard convection, *J. Fluid Mech.* 387 (1999) 321–341. doi:10.1017/S0022112099004607.
- [137] R. V. Craster, O.K. Matar, Dynamics and stability of thin liquid films, *Rev. Mod. Phys.* 81 (2009) 1131–1198. doi:10.1103/RevModPhys.81.1131.
- [138] Y. Alhendal, A. Turan, Thermocapillary bubble dynamics in a 2D axis swirl domain, *Heat Mass Transf.* 51 (2015) 529–542. doi:10.1007/s00231-014-1427-9.
- [139] A. Mohammadtabar, H. Nazari-poor, A. Riad, A. Hemmati, M. Sadrzadeh, Two-layer modeling of thermally induced Bénard convection in thin liquid nanofilms: Volume of Fluid approach vs. Thin-Film model, *AIP Adv.* 11 (2021) 045317.
- [140] J.. Brackbill, D.. Kothe, C. Zemach, A continuum method for modeling surface tension, *J. Comput. Phys.* 100 (1992) 335–354. doi:10.1016/0021-9991(92)90240-Y.
- [141] D. Youngs, Time-Dependent Multi-material Flow with Large Fluid Distortion, in: *Num. Method Fluid Dyn.*, 1982: pp. 273–285.
- [142] C.. Hirt, B.. Nichols, Volume of fluid (VOF) method for the dynamics of free boundaries, *J. Comput. Phys.* 39 (1981) 201–225. doi:10.1016/0021-9991(81)90145-5.
- [143] Y. Alhendal, A. Turan, A. Kalendar, Wall effects on the thermocapillary migration of single gas bubbles in stagnant liquids, 2016. doi:10.1007/s00231-016-1903-5.
- [144] M. Francois, A Study of the Volume of Fluid Method for Moving Boundary Problems, *Theses - Daytona Beach.* (1998). <https://commons.erau.edu/db-theses/286> (accessed December 16, 2019).
- [145] M. Shams, Modelling two-phase flow at the micro-scale using a volume-of-fluid method, 2018.

- [146] E. Schäffer, S. Harkema, R. Blossey, Electrohydrodynamic instabilities in polymer films
Related content Temperature-gradient-induced instability in polymer films, n.d.
<http://iopscience.iop.org/article/10.1209/epl/i2001-00183-2/pdf> (accessed September 12, 2018).
- [147] B. Khorshidi, B. Soltannia, T. Thundat, M. Sadrzadeh, Synthesis of thin film composite polyamide membranes: Effect of monohydric and polyhydric alcohol additives in aqueous solution, *J. Memb. Sci.* 523 (2017) 336–345. doi:10.1016/j.memsci.2016.09.062.
- [148] B. Soltannia, M.A. Islam, J.Y. Cho, F. Mohammadtabar, R. Wang, V.A. Piunova, Z. Almansoori, M. Rastgar, A.J. Myles, Y.H. La, M. Sadrzadeh, Thermally stable core-shell star-shaped block copolymers for antifouling enhancement of water purification membranes, *J. Memb. Sci.* 598 (2020) 117686. doi:10.1016/j.memsci.2019.117686.
- [149] B. Khorshidi, S. Shabani, M. Sadrzadeh, Prospects of nanocomposite membranes for water treatment by osmotic-driven membrane processes, in: *Nanocomposite Membr. Water Gas Sep.*, Elsevier, 2019: pp. 257–297. doi:10.1016/B978-0-12-816710-6.00011-0.
- [150] A.M. Koupaei, H. Nazariipoor, M. Sadrzadeh, Electrohydrodynamic Patterning of Polyethersulfone Membranes, *Langmuir.* 35 (2019) 12139–12149. doi:10.1021/acs.langmuir.9b01948.
- [151] D. Bhattacharjee, H. Nazariipoor, B. Soltannia, M.F. Ismail, M. Sadrzadeh, An experimental and numerical study of droplet spreading and imbibition on microporous membranes, *Colloids Surfaces A Physicochem. Eng. Asp.* 615 (2021) 126191. doi:10.1016/j.colsurfa.2021.126191.
- [152] B. Soltannia, D. Sameoto, Strong, reversible underwater adhesion via gecko-inspired hydrophobic fibers, *ACS Appl. Mater. Interfaces.* 6 (2014) 21995–22003. doi:10.1021/am5075375.
- [153] S. Shabani, B. Khorshidi, M. Sadrzadeh, Development of nanocomposite membranes by biomimicking nanomaterials, in: *Nanocomposite Membr. Water Gas Sep.*, Elsevier, 2019: pp. 219–236. doi:10.1016/B978-0-12-816710-6.00009-2.
- [154] T. Ambjörnsson, M.A. Lomholt, P.L. Hansen, Applying a potential across a

- biomembrane: Electrostatic contribution to the bending rigidity and membrane instability, *Phys. Rev. E - Stat. Nonlinear, Soft Matter Phys.* 75 (2007) 051916.
doi:10.1103/PhysRevE.75.051916.
- [155] J.T. Schwalbe, P.M. Vlahovska, M.J. Miksis, Lipid membrane instability driven by capacitive charging, *Phys. Fluids*. 23 (2011) 041701. doi:10.1063/1.3567276.
- [156] *Analysis of Transport Phenomena - Hardcover - William M. Deen - Oxford University Press*, (n.d.). <https://global.oup.com/ushe/product/analysis-of-transport-phenomena-9780199740284?cc=ca&lang=en&> (accessed January 1, 2021).
- [157] S. Miladinova, G. Lebon, E. Toshev, Thin-film flow of a power-law liquid falling down an inclined plate, *J. Nonnewton. Fluid Mech.* 122 (2004) 69–78.
doi:10.1016/j.jnnfm.2004.01.021.
- [158] B.S. Dandapat, A. Mukhopadhyay, Waves on the surface of a falling power-law fluid film, *Int. J. Non. Linear. Mech.* 38 (2003) 21–38. doi:10.1016/S0020-7462(01)00038-5.
- [159] R.S.R. Gorla, Rupture of thin power-law liquid film on a cylinder, *J. Appl. Mech. Trans. ASME*. 68 (2001) 294–297. doi:10.1115/1.1355033.
- [160] S.M. Troian, X.L. Wu, S.A. Safran, Fingering instability in thin wetting films, *Phys. Rev. Lett.* 62 (1989) 1496–1499. doi:10.1103/PhysRevLett.62.1496.
- [161] V. Garg, P.M. Kamat, C.R. Anthony, S.S. Thete, O.A. Basaran, Self-similar rupture of thin films of power-law fluids on a substrate, *J. Fluid Mech.* 826 (2017) 455–483.
doi:10.1017/jfm.2017.446.
- [162] K.X. Hu, M. He, Q.S. Chen, Instability of thermocapillary liquid layers for Oldroyd-B fluid, *Phys. Fluids*. 28 (2016). doi:10.1063/1.4943971.
- [163] K.X. Hu, M. He, Q.S. Chen, R. Liu, Linear stability of thermocapillary liquid layers of a shear-thinning fluid, *Phys. Fluids*. 29 (2017) 073101. doi:10.1063/1.4994596.
- [164] M. Iervolino, J.P. Pascal, A. Vacca, Thermocapillary instabilities of a shear-thinning fluid falling over a porous layer, *J. Nonnewton. Fluid Mech.* 270 (2019) 36–50.
doi:10.1016/j.jnnfm.2019.06.011.

- [165] M. Naïmi, M. Hasnaoui, J.K. Platten, Marangoni convection of non-Newtonian power law fluids in a shallow rectangular cavity, *Eng. Comput. (Swansea, Wales)*. 17 (2000) 638–668. doi:10.1108/02644400010340570.
- [166] Z. Alloui, P. Vasseur, Onset of Marangoni convection and multiple solutions in a power-law fluid layer under a zero gravity environment, *Int. J. Heat Mass Transf.* 58 (2013) 43–52. doi:10.1016/j.ijheatmasstransfer.2012.11.052.
- [167] C.H. Chen, Marangoni effects on forced convection of power-law liquids in a thin film over a stretching surface, *Phys. Lett. Sect. A Gen. At. Solid State Phys.* 370 (2007) 51–57. doi:10.1016/j.physleta.2007.05.024.
- [168] I.M.R. Sadiq, R. Usha, Long-wave instabilities in a non-Newtonian film on a nonuniformly heated inclined plane, *J. Fluids Eng. Trans. ASME*. 131 (2009) 0312021–03120217. doi:10.1115/1.3059702.
- [169] G. Karapetsas, V. Bontozoglou, Non-linear dynamics of a viscoelastic film subjected to a spatially periodic electric field, (2015). doi:10.1016/j.jnnfm.2014.12.012.
- [170] G.L. Wilkes, An overview of the basic rheological behavior of polymer fluids with an emphasis on polymer melts, *J. Chem. Educ.* 58 (1981) 880–892. doi:10.1021/ed058p880.
- [171] W.H. Vandevender, K.H. Haskell, The SLATEC mathematical subroutine library, *ACM SIGNUM Newsl.* 17 (1982) 16–21. doi:10.1145/1057594.1057595.
- [172] Petzold, L. R, Description of DASSL: a differential/algebraic system solver, (1982).
- [173] K.E. Brenan, L.R. Petzold, The Numerical Solution of Higher Index Differential/Algebraic Equations by Implicit Methods, *SIAM J. Numer. Anal.* 26 (1989) 976–996. doi:10.1137/0726054.

Appendices

Appendix A – Vertical distance and wettability in phase field approach

A1. Effect of the vertical distance between two substrates on the pattern formation

Figure A1 shows the effect of the distance between hot and cold substrate in the pattern formation. The largest height of the pattern can be obtained when the distance between two substrates is maximum. In addition, there is no residual polymer between two patterns in case c (Quasi-steady state) compared to that of in two other cases. Moreover, the process time of reaching polymer to the protrusions is longer than that of in case (a) and case (b).

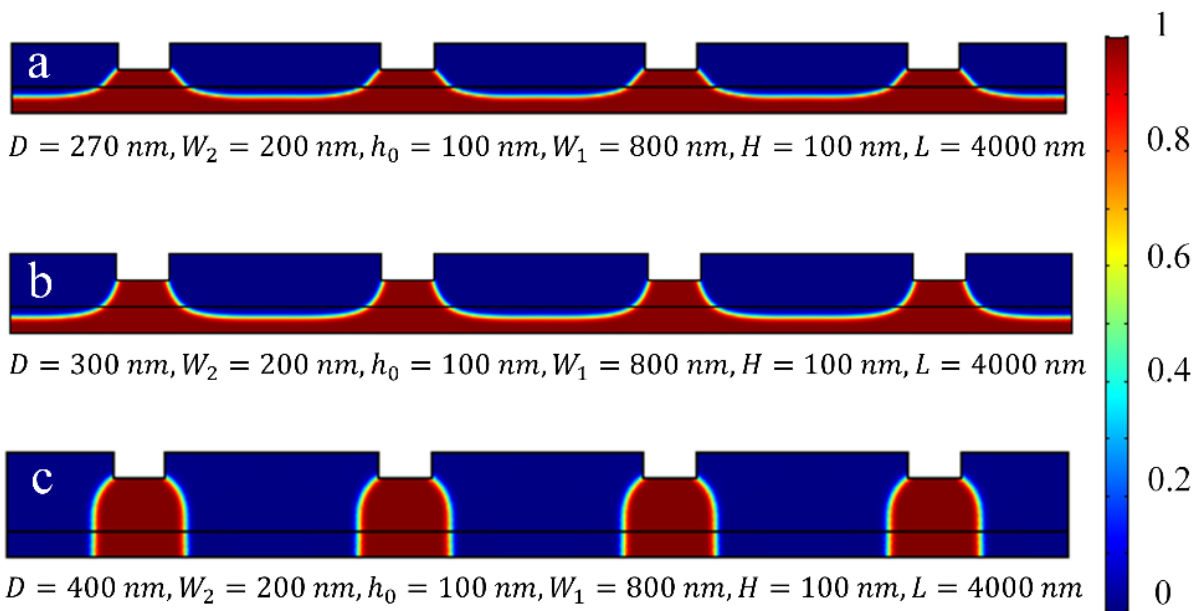


Figure A1. The changing trend of pattern formation induced by thermal gradient with the different substrates distance, (a) 270 nm, (b) 300 nm and (c) 400 nm.

A2. Effect of the wettability of protrusions on the pattern formation

The contact angle between the polymer film and solid substrates indicates the relative strength of the surface energy between the polymer and the substrate, which influences the thin film instability, shape, and size of patterns, significantly. Surface tension balance at the liquid/solid

interface is shown in Figure A2. Young's equation relates the contact angle (θ) and the surface tension of the film (σ_f), the interfacial tension between film and substrate (σ_{sf}) and the surface free energy of the solid substrate (σ_s) as follows [113]:

$$\sigma_s = \sigma_{sf} + \sigma_f \cos \theta. \quad (\text{A1})$$

The interactions between the liquid film and the underlying solid substrate leads to the film deformation and formation of various meso-scale structures [59].

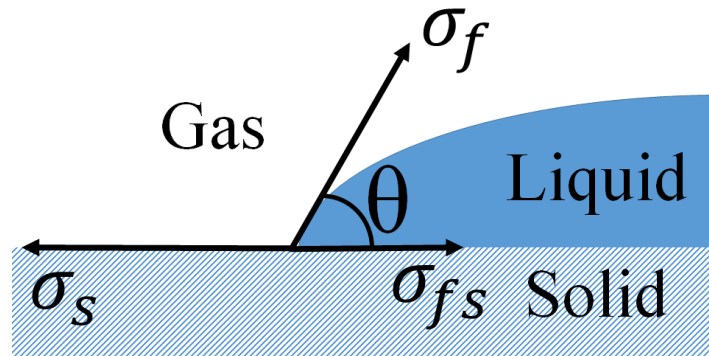


Figure A2. Surface tension balance based on Young's considerations.

Appendix B – Thin film equation derivation

B1. Vertical characteristic wavelength

To derive thin film equation for a homogeneous system, the distance between two substrates was used [19,84,137]. However, since there is a non-homogeneous system in this study due to the presence of a top patterned plate, we need to choose an appropriate distance (d_1 or d_2). To see the effect of substrates distance on the dynamics, instability, and morphological evolution of the nanofilm, we solve the non-linear thin film equation at different pattern height.

Figure B1 shows the effect of the pattern height on the final shape of the pattern formation. For all cases, d_2 was set to be 200 nm, and by changing d_1 , three different pattern heights were tested. As shown in Figure (a)-(c), the created patterns are similar in shape and have the same characteristic wavelength. However, the processing time is different. Since the thermal gradient in case (c) is higher than that in other cases, the processing time is shorter, and thus, it takes less time for the polymer to touch the top substrate. Consequently, the shorter distance between substrates is used to derive linear stability (LS) analysis in this study.

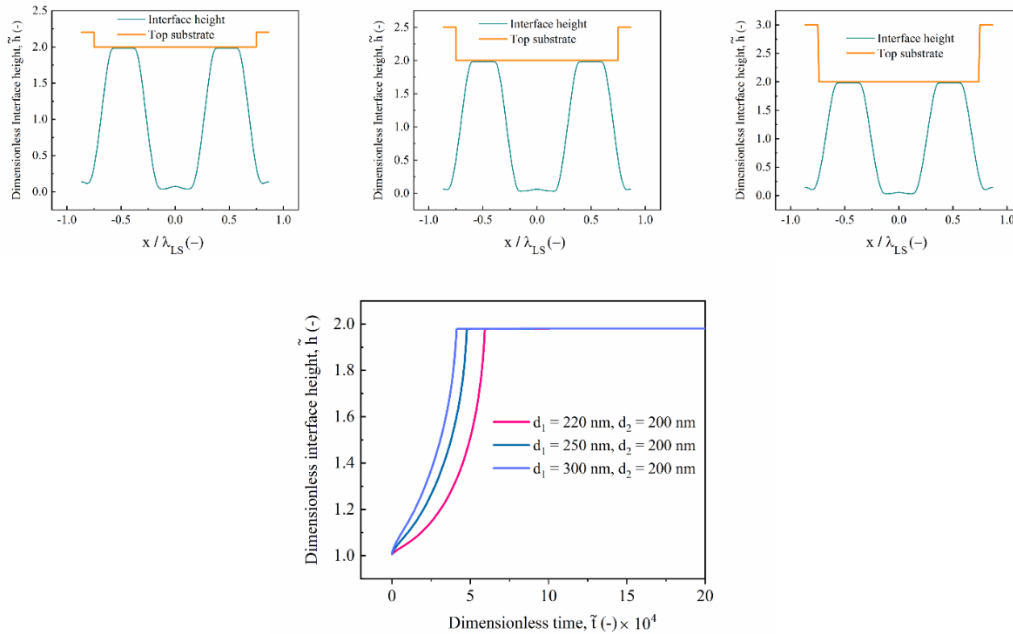


Figure B1. Thermally-induced hierarchical structures for a patterned template. 2D result of nonlinear thin film, $h_0 = 100$ nm, $d_2 = 200$ nm, $w = 6$ μ m, $l_p = 500$ nm and $\Delta T = 50$ K at different shorter substrates distance, (a) $d_1 = 220$ nm, (b) $d_1 = 250$ nm, and (c) $d_1 = 300$ nm. (d) The tracking of the Interface height of pillar at different shorter substrates distance.

B2. Thin-film equation for a Newtonian fluid

To describe the spatiotemporal evolution of the film under TC stress, we employ mass conservation and momentum and energy balances for an incompressible Newtonian film, which are respectively written as

$$\nabla \cdot \mathbf{u}_i = 0, \quad (\text{B1})$$

$$\rho_i \left[\frac{\partial \mathbf{u}_i}{\partial t} + (\mathbf{u}_i \cdot \nabla) \mathbf{u}_i \right] = -\nabla P_i + \nabla \cdot \{ \mu_i [\nabla \mathbf{u}_i + (\nabla \mathbf{u}_i)^T] \}, \quad (\text{B2})$$

$$\rho_i C_{p_i} \left(\frac{\partial T_i}{\partial t} + \mathbf{u}_i \cdot \nabla T_i \right) = k_i \nabla^2 T. \quad (\text{B3})$$

Subscript i differentiates between the following fluid phases: molten polymer film and air as a bounding layer. In the energy balance equation, energy dissipation due to viscous forces is assumed to be negligible. The thermal conductivity is k_i , heat capacity is C_{p_i} , and fluid velocity is \mathbf{u}_i . The hydrodynamic and thermal boundary conditions are

$$\mathbf{u}_1 = 0; \quad T_1 = T_H \quad \text{at } z = 0, \quad (\text{B4})$$

$$\mathbf{u}_2 = 0; \quad T_2 = T_C \quad \text{at the top substrate}, \quad (\text{B5})$$

At the interface [$z = h(x, t)$] the boundary conditions are

$$\mathbf{u}_{rel} = 0 \quad \text{and} \quad T_1 = T_2, \quad (\text{B6})$$

$$\text{Thermal conduction: } \mathbf{n} \cdot (k_1 \nabla T_1 - k_2 \nabla T_2) = 0. \quad (\text{B7})$$

Finally, the normal and tangential stress balances are:

$$\mathbf{n} \cdot [\sigma_1 \cdot \mathbf{n} - \sigma_2 \cdot \mathbf{n}] = \kappa \sigma, \quad (\text{B8})$$

$$\mathbf{t}_j \cdot [\sigma_1 \cdot \mathbf{n} - \sigma_2 \cdot \mathbf{n}] = \nabla_s \sigma \cdot \mathbf{t}_j, \quad (\text{B9})$$

The stress tensor $\sigma = -PI + \mu_i [\nabla \mathbf{u}_i + (\nabla \mathbf{u}_i)^T]$ is defined as the summation of hydrostatic and viscous stresses. The term $\kappa \sigma$ is the mean interfacial curvature of the film interface while \mathbf{n} and \mathbf{t}_j are the normal and tangential vectors. The term $\nabla_s \sigma = (d\sigma/dT) \nabla_s T|_{z=h}$ is the interfacial tension gradient along the interface, which represents the TC pressure in the tangential stress balance at the interface. The surface tension is assumed to decrease linearly with the interfacial temperature, i.e., $\sigma = \sigma_0 - \sigma_T(T - T_0)$ where $\sigma_T (>0)$, σ_0 and T_0 are the surface tension gradient, the reference

interfacial tension, and the reference temperature, respectively. Finally, to relate the interface height to the interfacial velocity components, a kinematic boundary condition is imposed:

$$w = \frac{\partial h}{\partial t} + u \frac{\partial h}{\partial x} \quad \text{at} \quad z = h(x, t), \quad (\text{B10})$$

The following dimensionless equation, which describes the spatiotemporal evolution of thin liquid film subjected to the transverse thermal gradient, is obtained:

$$\frac{\partial \tilde{h}}{\partial \tilde{t}} + \nabla \cdot \left\{ \frac{\tilde{h}^3}{3} Ca^{-1} \nabla (\nabla^2 \tilde{h}) + \frac{\tilde{h}^2}{2} \frac{Ma k_r \tilde{d}_2}{[(1 - k_r) \tilde{h} + k_r \tilde{d}_2]^2} \nabla \tilde{h} \right\} = 0, \quad (\text{B11})$$

B3. Linear Stability (LS) analysis

Linear stability (LS) analysis is the conventional technique in predicting the characteristic wavelength for the growth of instabilities, λ_c . It has been extensively used in the literature for thin-film studies [13,103,137]. The derivation of the thin-film equation for TC induced instabilities are omitted for brevity since they are available in the literature [44,114,117,146]. Using the scaling factors and dimensionless numbers defined above, the thin-film equation in its scaled form is given by

$$\frac{\partial \tilde{h}}{\partial \tilde{t}} + \nabla \cdot \left\{ \frac{\tilde{h}^3}{3} Ca^{-1} \nabla (\nabla^2 \tilde{h}) + \frac{\tilde{h}^2}{2} \frac{Ma k_r \tilde{d}_2}{[(1 - k_r) \tilde{h} + k_r \tilde{d}_2]^2} \nabla \tilde{h} \right\} = 0, \quad (\text{B12})$$

To derive Eq. B12, the shorter distance between two substrates (\tilde{d}_2) is used (see section S1). The corresponding wavelength is calculated by replacing the uniform interface height (h) in the so-called thin-film equation with a periodic perturbation of $\tilde{h} = 1 + \xi \exp(\bar{\kappa}(\tilde{x})i + S(\bar{\kappa})\tilde{t})$, where $i = \sqrt{-1}$, $\bar{\kappa}$ is the wavenumber, $S(\bar{\kappa})$ is the growth coefficient, and $\xi (\ll 1)$ is the infinitesimal amplitude coefficient. After substituting \tilde{h} in Eq. B12 with sinusoidal perturbation, and neglecting terms with ξ^2 and ξ^3 :

$$\begin{aligned} \frac{\partial \tilde{h}}{\partial \tilde{t}} + \frac{Ca^{-1}}{3} \left(3\tilde{h}^2 \frac{\partial \tilde{h}}{\partial \tilde{x}} \frac{\partial^3 \tilde{h}}{\partial \tilde{x}^3} + \tilde{h}^3 \frac{\partial^4 \tilde{h}}{\partial \tilde{x}^4} \right) + \tilde{h} \left(\frac{\partial \tilde{h}}{\partial \tilde{x}} \right)^2 \frac{Ma k_r \tilde{d}_2}{[(1 - k_r) \tilde{h} + k_r \tilde{d}_2]^2} \\ + \frac{\tilde{h}^2}{2} \frac{Ma k_r \tilde{d}_2}{[(1 - k_r) \tilde{h} + k_r \tilde{d}_2]^3} \left\{ \frac{\partial^2 \tilde{h}}{\partial \tilde{x}^2} [(1 - k_r) \tilde{h} + k_r \tilde{d}_2] \right. \\ \left. - 2(1 - k_r) \left(\frac{\partial \tilde{h}}{\partial \tilde{x}} \right)^2 \right\} = 0. \end{aligned} \quad (\text{B13})$$

The non-linear terms involving spatial derivatives in Eq. B18, such as $(\frac{\partial \tilde{h}}{\partial \tilde{x}} \frac{\partial^3 \tilde{h}}{\partial \tilde{x}^3})$ and $(\frac{\partial \tilde{h}}{\partial \tilde{x}})^2$, are eliminated. The time and first- to fourth-order spatial derivatives, and the terms \tilde{h}^2 and \tilde{h}^3 are replaced with the following expressions:

$$\frac{\partial \tilde{h}}{\partial \tilde{t}} = S(\bar{\kappa})\xi E, \quad \frac{\partial \tilde{h}}{\partial \tilde{x}} = i\bar{\kappa}\xi E, \quad \frac{\partial^2 \tilde{h}}{\partial \tilde{x}^2} = -\bar{\kappa}^2 \xi E, \quad \frac{\partial^3 \tilde{h}}{\partial \tilde{x}^3} = -i\bar{\kappa}^3 \xi E, \quad \frac{\partial^4 \tilde{h}}{\partial \tilde{x}^4} = \bar{\kappa}^4 \xi E, \quad (\text{B14})$$

$$\tilde{h}^2 = 1 + 2\xi E + (\xi E)^2, \quad \tilde{h}^3 = 1 + 3\xi E + 3(\xi E)^2 + (\xi E)^3,$$

where $E = \exp[\bar{\kappa}(\tilde{x})i + S(\bar{\kappa})\tilde{t}]$ is defined as a notational shorthand. After expanding all terms and eliminating further non-linear terms (ξ^2 and $\xi^3 \ll 1$), the following dispersion relation is found:

$$S(\bar{\kappa}) + \frac{\bar{\kappa}^4}{Ca} - \frac{3Ma k_r \tilde{d}_2}{2[(1 - k_r) + k_r \tilde{d}_2]^2} \bar{\kappa}^2 = 0. \quad (\text{B15})$$

The dispersion relation in Eq. B15 relates the time and length growth coefficients to the physical parameters in the system. The wavenumber $\bar{\kappa}$ corresponds to the wavelength ($\lambda = 2\pi l/\bar{\kappa}$) and the growth rate $[S(\bar{\kappa})]$. Zeros of the dispersion relation $S(\bar{\kappa}_0) = 0$ indicates the disturbances that remain unchanged over time. The thin film remains stable if $S(\bar{\kappa}) < 0$, such that the disturbances are stabilized over time. When there is no hydrostatic stabilizing force, the TC-induced instabilities in confined nanofilms always lead to pattern formation. Therefore, there is always a wave number band, $0 < \bar{\kappa} < \bar{\kappa}_0 = \sqrt{3 Ca Ma k_r \tilde{d}_2 / 2[(1 - k_r) + k_r \tilde{d}_2]^2}$, where $S(\bar{\kappa}) > 0$. The fastest-growing wavelength (λ_{LS}) corresponds to the positive root of $\frac{\partial S}{\partial \bar{\kappa}} = 0$,

$$\lambda_{LS} = 2\pi[h_0(1 - k_r) + k_r d_2] \sqrt{\frac{4\sigma h_0}{3d_2 \sigma_T k_r \Delta T}}. \quad (\text{B16})$$